Investigation of light-addressable potentiometric sensors for electrochemical imaging based on different semiconductor substrates

By Fan Wu

September 2017

A thesis submitted for the degree of Doctor of Philosophy (Ph.D.) to the

School of Engineering and Materials Science

Queen Mary University of London

Declaration

I, Fan Wu, confirm that the research included within this thesis is my own work or that where it has been carried out in collaboration with, or supported by others, that this is duly acknowledged below and my contribution indicated. Previously published material is also acknowledged below.

I attest that I have exercised reasonable care to ensure that the work is original, and does not to the best of my knowledge break any UK law, infringe any third party's copyright or other Intellectual Property Right, or contain any confidential material.

I accept that the College has the right to use plagiarism detection software to check the electronic version of the thesis.

I confirm that this thesis has not been previously submitted for the award of a degree by this or any other university.

Signature: Fan Wu

Date: 13/09/2017

Abstract

Light-addressable potentiometric sensors (LAPS) and scanning photo-induced impedance microscopy (SPIM) have been extensively applied as chemical sensors and biosensors. This thesis focuses on the investigation of LAPS and SPIM for electrochemical imaging based on two different semiconductor substrates, silicon on sapphire (SOS) and indium tin oxide (ITO) coated glass.

Firstly, SOS substrates were modified with 1,8-nonadiyne self-assembled organic monolayers (SAMs), which served as the insulator. The resultant alkyne terminals provided a platform for the further functionalization of the sensor substrate with various chemicals and biomolecules by Cu(I)-catalyzed azide alkyne cycloaddition (CuAAC) 'click' reactions. The CuAAC reaction combined with microcontact printing (μCP) was successfully used to create chemical patterns on alkyne-terminated SOS substrates. The patterned monolayers were found to be contaminated with the copper catalyst used in the click reaction as visualized by LAPS and SPIM. Different strategies for avoiding copper contamination were tested. Only cleaning of the silicon surfaces with an ethylenediaminetetraacetic acid tetrasodium salt (EDTA) solution containing trifluoroacetic acid after the 'click' modification proved to be an effective method as confirmed by LAPS and SPIM results, which allowed, for the first time, the impedance of an organic monolayer to be imaged.

Furthermore, the 1,8-nonadiyne modified SOS substrate was functionalized and patterned with an RGD containing peptide, which was used to improve the biocompatibility of the substrate and cell adhesion. By seeding cells on the peptide patterned sensor substrate, cell patterning was achieved. Single cell imaging using LAPS and SPIM was attempted on the RGD containing peptide modified SOS substrate.

Finally, an ITO coated glass substrate was used as a LAPS substrate for the first time. The photocurrent response, the pH response, LAPS and SPIM imaging and its lateral

resolution using ITO coated glass without any modification were investigated. Importantly, single cell images were obtained with this ITO-based LAPS system.

Publications

- F. Wu, D. Zhang, M. Watkinson, S. Krause. Single cells imaging using light-addressable potentiometric sensors with ITO coated glass as the substrate. (In preparation)
- F. Wu, D. Zhang, J. Wang, M. Watkinson, S. Krause. Copper contamination of self-assembled organic monolayer modified silicon surfaces following a 'click' reaction characterized with LAPS and SPIM. *Langmuir*, 2017, 33, 3170-3177.
- F. Wu, I. Campos, D. Zhang, S. Krause. Biological imaging using light-addressable potentiometric sensors and scanning photo-induced impedance microscopy. *Proceeding of the Royal Society A: Mathematical, Physical and Engineering Science*, 2017, 473.
- D. Zhang, F. Wu, S. Krause. LAPS and SPIM imaging using ITO-coated glass as the substrate material. *Analytical Chemistry*, 2017, 89, 8129-8133.
- D. Zhang, F. Wu, J. Wang, M. Watkinson, S. Krause. Image detection of yeast Saccharomyces cerevisiae by light-addressable potentiometric sensors (LAPS). *Electrochemistry Communications*, 2016, 72, 41-45.
- J. Wang, I. Campos, F. Wu, J. Zhu, G. Sukhorukov, M. Palma, M. Watkinson, S. Krause. The effect of gold nanoparticles on the impedance of microcapsules visualized by scanning photo-induced impedance microscopy. *Electrochimica Acta*, 2016, 208, 39-46.
- J. Wang, F. Wu, M. Watkinson, J. Zhu and S. Krause. "Click" patterning of self-assembled monolayers on hydrogen-terminated silicon surfaces and their characterization using light-addressable potentiometric sensors. *Langmuir*, 2015, 31, 9646-9654.

Acknowledgements

First of all, I would like to express my sincere gratitude to my first supervisor Dr Steffi Krause, who brought me into the world of LAPS. Without her continuous support and encouragement and sufficient guidance and insightful ideas, I would not be able to come so far and finish my thesis. She is truly helpful not only to my research but also to my life. She will always be my mentor and a precious friend.

Secondly, I would like to thank my second supervisor Prof. Mike Watkinson, who has been supportive and given me a lot of pertinent, practical and valuable advice and guidance in my last four years of doctoral study. His erudite knowledge in chemistry is always helpful and vital to my project.

Particularly, I am thankful to one of my colleagues Dr Dewen Zhang whom I'm honoured to be working with for the last two years. I have benefited a lot from his novel, constructive and sometimes crazy ideas, which make my work more effective and more colourful. I've really enjoyed having discussions with him where I have learned a lot. I will never forget the days and nights we spent doing experiments together.

Another colleague I would like to thank is Dr Jian Wang, who taught me many useful and important experimental skills, such as the surface modification of silicon surfaces and the microcontact printing, in the beginning of my PhD study, which benefited me in my entire PhD study.

My sincere thanks also go to Dr Karin Hing and Prof. Gleb Sukhorukov for providing the cells and some advice for cell related issues, to Dr Philip Duncanson and Dr Inmacualda Sánchez for their guidance in chemical synthesis and some useful suggestions, to my labmates, Mr Martin John Gibbs and Miss Norlaily Ahmad, Dr Anna Biela, Miss Muchun Zhong, Mr Bo Zhou and Mr Ying Tu for the stimulating discussions and their companion, to Ms Jun Ma, Mr Chris Mole, Mr Shafir Iqba, Dr Dongsheng Wu and Mr Dennis Ife for

their technical support, to Mr Geoff Gannaway in the School of Physics and Astronomy for cleanroom training.

I am grateful to China Scholarship Council and Queen Mary University of London for the financial support. I would also like to thank NEXUS (UK) for XPS measurements.

Thanks to all my friends especially Wenjun Sun and my housemates Fan Wang and Yejiao Shi for all the fun we have had and for the sleepless nights we were together before deadlines in the last four years.

Last but not the least, I would like to thank my family for supporting me and encouraging me throughout my PhD study and my life. In particular, I thank Jingyuan Zhu, for sharing all my happiness and bitterness in the past four years.

Table of Contents

Abstract i

Publications iii

Acknowledgements iv

Table of Contents vi

List of abbreviation x

List of tables xiii

List of figures xiv

1. Introduction 1

1.1 Background and motivation 1

1.2 LAPS and SPIM 2

1.2.1 Principle of LAPS/SPIM 2

1.2.2 Spatial resolution of LAPS/SPIM 4

1.2.3 Temporal resolution 10

1.2.4 Applications of LAPS/SPIM 13

1.3 Modification of silicon surfaces with self-assembled organic monolayers (SAMs) 22

1.3.1 Deposition of SAMs on oxide-free silicon surfaces 23

1.3.2 Further derivatization of SAMs on silicon via ‘click’ chemistry 28

1.4 Chemical patterning on silicon surfaces 32

1.4.1 Photolithography 33

1.4.2 Microcontact printing 34

1.5 Electrochemical methods for live cell imaging 36

2. Experiments....40

2.1 Materials....40

2.2 Surface preparation methods....41

2.2.1 Preparation of an ohmic contact on the SOS substrate....41

2.2.2 Assembly of 1,8-nonadiyne monolayer....42

2.3 Characterization methods....43

2.3.1 Water contact angle measurement....43

2.3.2 Ellipsometry....44

2.3.3 X-ray photoelectron spectroscopy (XPS)....45

2.3.4 Electrochemical impedance spectroscopy (EIS)....46

2.3.5 Nuclear Magnetic Resonance Spectroscopy....47

2.3.6 Electrospray ionization mass spectrometry (ESI-MS)....47

2.4 LAPS and SPIM setup....48

3. Copper contamination of self-assembled organic monolayer modified silicon surfaces following a 'click' reaction characterized with LAPS and SPIM....50

3.1 Introduction....50

3.2 Experimental methods....51

3.2.1 Materials....51

3.2.2 Preparation of silicon master and PDMS stamp....52

3.2.3 Cleaning of the PDMS stamp....52

3.2.4 Patterning of SOS surfaces with microcontact printing combined with 'click' chemistry....53

3.2.5 Surface characterization....55

3.2.6 LAPS and SPIM measurement....55

3.3 Results and discussion 55

3.3.1 Characterization of 1,8-nonadiyne monolayer and ‘click’ functionalization by μCP 55

3.3.2 The effect of the PDMS stamps for μCP on LAPS and SPIM images 58

3.3.3 Copper residue visualized with LAPS and SPIM. 60

3.3.4 Strategies for avoiding a copper(I) residue after ‘click’ modification. 64

3.3.5 SPIM and LAPS measurements of a click modified sample after removal of the copper residue. 66

3.4 Summary 67

4. Patterning osteoblasts on silicon on sapphire substrate in serum-free medium 68

4.1 Introduction 68

4.2 Experimental methods 69

4.2.1 Materials 69

4.2.2 Modification of cyclic-RGDfK peptide with 4-azidophenyl isothiocyanate (API) 69

4.2.3 SOS or Si surface functionalization with cyclic-RGDfK peptide 70

4.2.4 Surface patterning with cyclic-RGDfK peptide via μCP 70

4.2.5 Cell culturing and adhesion 71

4.2.6 Cell staining of actin 72

4.2.7 LAPS and SPIM measurement 72

4.3 Results and discussion 73

4.3.1 Functionalization of peptide with azide group 73

4.3.2 Characterization of RGD peptide modified SOS or Si substrate 74

4.3.3 The pH response of the peptide modified SOS surface with LAPS 77

4.3.4 Cell adhesion 77

4.3.5 Cell patterning 78

4.3.6 Single cell imaging with LAPS/SPIM 79

4.4 Summary 83

5. Preliminary results of single cells imaging using light-addressable potentiometric sensors with ITO coated glass as the substrate 85

5.1 Introduction 85

5.2 Experimental methods 86

5.2.1 Materials 86

5.2.2 Preparation of ITO coated glass 87

5.2.3 Cell culturing on ITO 87

5.2.4 Linear Sweep Voltammetry 87

5.2.5 LAPS measurement 88

5.3 Results and discussion 88

5.3.1 The photocurrent response of ITO coated glass 88

5.3.2 The pH response of ITO coated glass 89

5.3.3 LAPS and SPIM imaging of ITO coated glass 92

5.3.4 Cell imaging with LAPS and SPIM 96

5.4 Summary 99

6. Conclusions 101

7. Future work 104

8. References 106

List of abbreviation

AchE	Acetylcholinesterase
AFP	Alpha fetoprotein
API	4-Azidophenyl isothiocyanate
ATP	Adenosine triphosphate
CE	Counter electrode
CHO	Chinese hamster ovary
µCP	Microcontact printing
CuAAC	Cu(I)-catalyzed azide alkyne cycloaddition
CV	Cyclic voltammetry
2-D	Two-dimensional
DAQ	Data acquisition
DCM	Dichloromethane
DLP	Digital light processing
DMD	Digital micromirror device
DMEM	Dulbecco's Modified Eagle's Medium
DMSO	Dimethyl sulfoxide
DOPA	Dihydroxyphenylalanine
DPBS	Dulbecco's Phosphate Buffered Saline
E.coli	*Escherichia coli*
EDTA	Ethylenediaminetetraacetic acid
EIS	Electrolyte-insulator-semiconductor
ELISA	Enzyme Linked Immunosorbent Assays
ESCA	Electron spectroscopy for chemical analysis
ESI-MS	Electrospray Ionization mass spectrometry
ETH1117	*N,N′*-diheptyl-*N,N′*-dimethyl-1,4-butanediamide
FBS	Fetal Bovine Serum

FFT	Fast Fourier transformation
FITC-BSA	Fluorescein isothiocyanate labeled bovine serum albumin
fps	Frames per second
FTIR	Fourier-transform infrared spectroscopy
FWHM	Full width at half maximum
HDOPP-Ca	Bis[di-(n-octylphenyl)phosphato]calcium(II)
hPRL-3	Phosphatase of regenerating liver 3
HRP	Horseradish peroxidase
H-Si	Hydrogen-terminated silicon
HUVECs	Human umbilical vein endothelial cells
i-Pr,	Isopropyl
IR	Infrared
ITO	Indium tin oxide
LAPCIS	Light-addressable potentiometric and cellular impedance sensor
LAPS	Light-addressable potentiometric sensors
LED	Light emitting diode
LSV	Linear sweep voltammetry
NMR	Nuclear magnetic resonance
OLED	Organic light emitting diode
PAH	Poly allylamine hydrochloride
PBS	Phosphate buffered saline
PDMS	Polydimethylsiloxane
P-EIM	Plasmonic-based electrochemical impedance microscopy
PLOL	Poly-L-ornithine and laminin
PMMA	Poly(methyl methacrylate)
PVC	Polyvinyl chloride
QRCE	Quasi-reference counter electrode
RE	Reference electrode

RGD	Arginylglycylaspartic acid
SAMs	Self-assembled organic monolayers
SECM	Scanning electrochemical microscopy
SICM	Scanning ion conductance microscopy
SLPT	Scanned light pulse technique
SOI	Silicon on insulator
SOS	Silicon on sapphire
SPIM	Scanning photo-induced impedance microscopy
SPR	Surface plasmon resonance
TBTA	Tris[(1-benzyl-1H-1,2,3-triazol-4-yl)methyl]amine
t-Bu	*ter*t-butyl
TFA	Trifluoroacetic acid
TMEDA	*N*, *N*, *N*′, *N*′-Tetramethylethylenediamine
TMG	Trimethylgermanyl
UV	Ultraviolet
VCSELs	Vertical cavity surface emitting lasers
WE	Working electrode
XPS	X-ray photoelectron spectroscopy
XRR	X-ray reflectivity

List of tables

Table 2.1 Chemicals and reagents 40

Table 3.1 Contact angles and ellipsometry thicknesses of different surfaces 56

Table 4.1 Contact angle and ellipsometric thickness of 1,8 nonadiyne modified substrate and peptide modified substrate. 76

List of figures

Figure 1.1 (a) Basic setup for LAPS and SPIM measurements; (b) equivalent circuit for photocurrent measurements: i_P is the photocurrent generated in the space charge layer, C_{SC} is the DC voltage dependent capacitance of the space charge layer, and i_{Photo} the current measured in the external circuit; (c) LAPS measure changes in the surface potential (shift from curve A to B) by monitoring the shift of the I-V curve at a constant current or the change in the current at a constant voltage. SPIM monitors changes in the maximum photocurrent (shift from curve B to C), which are directly related to the local impedance of the illuminated part of the sensor chip. 3

Figure 1.2(a) Photocurrent image of an SU-8 pattern on an SOS substrate with a 0.5 µm thick silicon layer and an anodic oxide and (b) photocurrent line scans across the edge of the photoresist at different wavelengths[15]. 10

Figure 1.3 Experimental setup for high-resolution LAPS and SPIM measurements [3]. (V_{AC} – AC voltage, RE – reference electrode, CE – counter electrode, WE – working electrode, SAM – self assembled monolayer)..... 11

Figure 1.4 High-speed laser scanning setup for LAPS using a two-axis analogue micromirror [34]. (PDMS - polydimethylsiloxane, DAQ – data acquisition) 12

Figure 1.5 Optical fibres were mounted above the LAPS substrate in a microfluidic channel for dynamic monitoring of pH changes [45]. 13

Figure 1.6 The sandwich ELISA model used in LAPS. (F – fluorescein, b – biotin)..... 15

Figure 1.7 A pH image of colonies of yeast. Each dark region corresponds to a colony [6]. 20

Figure 1.8 Microcapsules attached on a COOH-terminated SOS substrate. (a) SPIM image measured at 0.9 V, (b) corresponding optical image [3]..... 21

Figure 1.9 Visualization of buffering action at 100 fps. (a) Injection of 10 mM NaOH solution into phosphate buffer and (b) Injection of 10 mM HCl solution into phosphate buffer [45]. 21

Figure 1.10 Schematic representation of the structure of SAMs deposited on solid substrates [136]. 22

Figure 1.11 Schematic representations of (a) native oxide removal on silicon surfaces and (b) hydrosilylation of H-Si. (R represents functionalized or non-functionalized hydrocarbon chain, Δ and hν represent thermal-activated and photo-activated processes, respectively) [165] 23

Figure 1.12 Mechanism of hydrosilylation of alkene on H-Si [166, 167]. 24

Figure 1.13 Schematic illustration of the two mechanisms, (top) radical-based mechanism and (bottom) exciton-mediated mechanism, for photochemical hydrosilylation of H-terminated Si surfaces [198].....25

Figure 1.14 Representative modification schemes for Si-Cl surfaces. (RMgX, R = -C_nH_{2n+1} (n = 1–18), –t-Bu, –i-Pr, $–C_6H_5$, $–CH=CHCH_3$); R-OH, R = $–C_nH_{2n+1}$) (n = 12, 18); and R-NH_2 (R = $–C_4H_9$, $–C_8H_{17}$, $–C_6H_5$) [140, 165]. 28

Figure 1.15 Cu(I)-catalyzed azide alkyne cycloaddition (CuAAC) ‘click’ reaction mechanism [217]. 29

Figure 1.16 Preparation of alkyne-terminated silicon surfaces through a two-step strategy and a further ‘click’ functionalization [212]. 30

Figure 1.17 A CuAAC ‘click’ reaction on 1,8-nonadiyne modified silicon surfaces [140, 220]. 30

Figure 1.18 Preparation of TMG-terminated film and its deprotection and a further one-

pot ‘click’ functionalization [219].....31

Figure 1.19 A ‘click’ reaction on azide-terminated silicon surfaces [221].....32

Figure 1.20 Standard procedure for photolithography to create physical and chemical patterns on a substrate [222]. 33

Figure 1.21 General process of μCP [244]. (a) A PDMS precursor is poured into a microstructured master and (b) cured and (c) peeled off; (d) PDMS stamp is immersed into an ‘ink’ solution; (e) the inked stamp is brought into focal contact with the substrate; (f) the stamp is removed.....35

Figure 1.22 (a) Click chemistry via the μCP of 1-octadecyne on azido-terminated SAMs; (b) AFM image of the line patterned 1-octadecyne monolayer; (c) fluorescent image of printed fluorescent alkynes on the azido-terminated surface [231]. 36

Figure 1.23 (a) Schematic representations of SICM for mapping single cells; (b) Optical microscope image of a human adipocyte cell on a collagen support with the SICM scan region indicated by white dashed lines and corresponding normalized DC ion current images at (c) negative (−0.4 V) and (d) positive (0.4 V) tip biases. The results demonstrated a negative surface charge distribution of the human adipocyte cell.[259]38

Figure 1.24 (a) Setup of the P-EIM; (b) bright-field, SPR and EIM images of Hela cells [263]. 39

Figure 2.1 Schematic representation of surface modification of SOS or Si substrate with 1,8-nonadiyne.....42

Figure 2.2 Schematic representation of (a) hydrophilic surface and (b) hydrophobic surface. 43

Figure 2.3 The principle of ellipsomotry [270].....44

Figure 2.4 Principle of XPS. 45

Figure 2.5 Schematic representation of the sample holder for photocurrent measurements. 48

Figure 2.6 Experimental setup for LAPS/SPIM measurements.....49

Figure 3.1 Schematic representation of cleaning the PDMS stamp with a soxhlet extractor. 53

Figure 3.2 Schematic illustration of the μCP of 'click' chemistry: azido-NH_2 was printed on 1,8-nonadiyne modified surface 1 and 'click' reactions occurred exclusively in the contact area (surface 2: an array of chemical pattern, surface 2*: a homogeneous surface functionalized with azido-NH_2 by a flat featureless PDMS stamp). For ellipsometry measurements, the above surface modification was carried out on silicon substrates....54

Figure 3.3 (a) XPS spectrum of samples modified with 1,8-nonadiyne (i), and 3-azido-1-propanamine without any further cleaning to remove the copper residue (ii), with further cleaning with 0.5 M HCl for 2 min (iii),and with further cleaning with 0.05% EDTA/TFA for 24 hours (iv). Narrow scans of (b) C 1s of surface 1, (c) N 1s and (d) C 1s of surface 2a*. 57

Figure 3.4 Narrow scan of Cu 2p3/2 of surface 2a*. 58

Figure 3.5 (a) SPIM images at a bias voltage of 0.8 V on control sample with uncleaned blank PDMS stamp, (b) the corresponding I-V curves on modified spots and blank 1,8-nonadiyne modified area, (c) normalized I-V curves. (d) SPIM image and (e) LAPS image of control sample with cleaned blank PDMS stamp at bias voltages of 0.8 V and 0.5 V, respectively, and (f) corresponding I-V curve.....60

Figure 3.6 The SPIM image of a 1,8-nonadiyne modified SOS sample patterned with 3 azido-1-propanamine with a 'click' reaction (surface 2a) after cleaning with (a) HCl

solution and corresponding (b) I-V curves ($I_{max\text{-}on}$ = 101.3 ± 2.7 nA, $I_{max\text{-}off}$ = 91.7 ± 0.6 nA) and (c) normalized curves. 61

Figure 3.7 SPIM images at a bias voltage of 0.8 V on (a) control surface a, (d) control surface b and (g) control surface c after rinsing with 0.5 M HCl for 2 min, and the corresponding I-V curves (b) ($I_{max\text{-}on}$ = 98.1 ± 1.1 nA, $I_{max\text{-}off}$ = 79.4 ± 1.6 nA), (e) ($I_{max\text{-}on}$ = 98.7 ± 2.6 nA, $I_{max\text{-}off}$ = 87.7 ± 1.0 nA), (h) ($I_{max\text{-}on}$ = 124.4 ± 2.3 nA, $I_{max\text{-}off}$ = 108.6 ± 1.3 nA) on modified spots (red) and non-modified 1,8-nonadiyne areas (black) and normalized I-V curves (c), (f), (i). 62

Figure 3.8 Cyclic voltammograms of control surface a after rinsing with HCl (red solid line) and a blank 1,8-nonadiyne modified surface (black dashed line) in 10 mM PBS solution (pH 7.4) with a scan rate of 50 mV/s. 63

Figure 3.9 (a) LAPS image of control surface a rinsing with EDTA/HCl for 24 hours at a bias voltage of 0.5 V, (b) the corresponding I-V curves on modified spots and blank 1,8-nonadiyne modified area ($I_{max\text{-}on}$ = 104.5 ± 1.4 nA, $I_{max\text{-}off}$ = 105.0 ± 3.6 nA), and (c) enlarged I-V curves with a voltage shift of -10 mV. (d) SPIM image and (e) LAPS image of control surface a rinsing with EDTA/TFA for 24 hours at bias voltages of 0.8 V and 0.5 V, respectively, and (f) corresponding I-V curve. 65

Figure 3.10 (a) The SPIM image of a 1,8-nonadiyne modified SOS sample patterned with 3-azido-1-propanamine with a 'click' reaction (surface 2a) after cleaning with EDTA/TFA solutions, and corresponding (b) I-V curves ($I_{max\text{-}on}$ = 100.2 ± 0.1 nA, $I_{max\text{-}off}$ = 112.9 ± 2.1 nA) and (c) normalized curves. 67

Figure 4.1 (a) Modification of cyclic-RGDfK peptide with API; (b) surface functionality with cyclic-RGDfK peptide via CuAAC 'click' reaction. 71

Figure 4.2 (a) ^{13}C NMR spectra of the starting materials and the product of azido-peptide; (b) ESI-MS spectrum of the unpurified azido-peptide. 74

Figure 4.3 XPS spectra of (a) 1,8-nonadiyne modified surface (black line) and cyclic-RGDfK peptide modified surface prepared with a 'click' reaction in solution (red line) and via μCP (blue line) ; narrow scans of (b) Si 2p and (c) C1s and (d) N 1s of cyclic-RGDfK peptide modified surface. 76

Figure 4.4 (a) LAPS I-V curves of peptide modified SOS substrate at different pH values; (b) the pH sensitivity of the peptide modified surface (R^2=0.9886). 77

Figure 4.5 Optical images of osteoblasts cultured on (a) cyclic-RGDfK peptide modified, (b) NH_2-terminated and (c) alkyne-terminated surfaces. 78

Figure 4.6 Fluorescent images of actin stained by Alexa Fluor® 633 Phalloidin in osteoblasts cultured on (a) cyclic-RGDfK peptide modified, (b) NH_2-terminated and (c) alkyne-terminated surfaces..... 78

Figure 4.7 Optical images of (a) osteoblasts patterns on patterned cyclic-RGDfK peptide modified SOS substrate and (b) patterns on PDMS stamp used in μCP cyclic-RGDfK peptide with 100 μm dots separated by 40 μm gaps. 79

Figure 4.8 Photocurrent dependency on the light intensity of the diode laser and femtosecond laser. 80

Figure 4.9 (a) SPIM image of the photoresist pattern measured with the femtosecond laser at a bias voltage of 0.8 V and (b) corresponding optical image from the camera..... 81

Figure 4.10 (a) SPIM image and (b) LAPS image of the osteoblasts cultured on cyclic-RGDfK peptide modified SOS substrate at a bias voltage of 0.8V and 0.6V with femtosecond laser, respectively, and corresponding (c) optical image of the osteoblast from camera and (d) I-V curve..... 82

Figure 5.1 (a) LSV curves of ITO coated glass in the dark and with chopped illumination;

(b)UV/Vis absorption spectra of ITO coated glass surface; Bode plots of (c) magnitude and (d) phase of ITO coated surface in 10 mM pH 7.4 PBS buffer at the open circuit potential in the dark. The equivalent circuit inset comprises a serial combination of the solution resistance (R) and a constant phase element (Q), which represents the double layer capacitance for a circular surface area with 3 mm diameter (13.2 μF/cm^2). 89

Figure 5.2 (a) LAPS I-V curves of ITO coated glass at different pH values; (b) the pH sensitivity of the ITO coated glass (R^2=0.98). 90

Figure 5.3 (a) optical image of an osteoblast monolayer cultured on ITO coated glass surface; (b) I-V curves on control sample (only cell culture medium incubated ITO coated glass substrate) before and after adding glucose solution for 60 min; (c) I-V curves on osteoblasts covered ITO coated glass substrate before and after adding glucose solution for 60 min and (d) corresponding voltage shift versus the time of before and after adding the glucose at a constant current value of 10 nA. 92

Figure 5.4 (a) LAPS I-V curve of blank ITO in pH 7.4 PBS buffer at 10 Hz with an unfocused laser source; (b) The frequency dependence of photocurrent and background AC current under dark condition.....93

Figure 5.5 (a) The LAPS image of blank ITO at 2 V and 10 Hz with a focused laser beam; (b) z axis line scan of the photocurrent around the focus; (c) the LAPS I-V curve in focus at 10 Hz. 94

Figure 5.6 (a) The LAPS image of a PMMA dot at 2 V and 10 Hz with a focused laser beam; (b) x-axis photocurrent scan across the edge of the PMMA dot; (c) the first derivative of (b) with FWHM of 2.3 μm.....95

Figure 5.7 (a) LAPS image of ITO coated glass surface with a PAH dot at 1.5V with a frequency of 10Hz and (b) corresponding I-V curves on the PAH dot (red) and on the blank ITO (black); (c) Bode plots of ITO coated glass surface before (black) and after

(red) coating with a complete PAH layer at 1.5V. 96

Figure 5.8 (a) LAPS image of osteoblasts on ITO coated glass surface at 1.5 V with a frequency of 10 Hz and corresponding (b) I-V curves on cell (point A red and B blue) and off cell C (black),(c) phase angle image,(d) phase angle-voltage curves, (e) optical image and (f) Bode plots of ITO coated glass surface at 1.5V before (black) and after (red) culturing a layer of osteoblasts. 97

Figure 5.9 (a) LAPS image of neurons on ITO coated glass surface at 1.5V and a frequency of 10Hz and corresponding (b) I-V curves on cell (point D red and E blue) and off cell F (black) and (c) optical image. 99

1. Introduction

1.1 Background and motivation

Cells, as the basic structural, functional and biological unit of all known living organisms, have been extensively investigated since they were discovered by Robert Hooke in 1665 with the first optical microscope. Over the past centuries, optical microscopy has developed significantly, especially the invention of super-resolved fluorescence microscopy, which has brought optical microscopy into the nanodimension and enabled the visualisation of the pathways of individual molecules such as proteins inside living cells with the help of fluorescent molecules [1, 2]. However, fluorescence labelling may have side effects on cellular health and a time-resolved measurement on cellular dynamic processes may cause photobleaching. Other live-cell imaging methods include electrochemical imaging approaches, which have become more and more attractive in recent years, as they are label-free techniques, being able to detect the electrical properties of living cells (cell surface charge and cell impedance), which are not accessible to optical imaging methods.

Light-addressable potentiometric sensors (LAPS) and scanning photo-induced impedance microscopy (SPIM) are electrochemical imaging techniques based on photocurrent measurements at electrolyte-insulator-semiconductor (EIS) field-effect capacitors. By generating photocurrents locally with a focused light-source, they provide information such as surface potential, ion concentrations and electrical impedance with lateral resolution without the need for a probe or a patterned substrate. In contrast to micro-fabricated arrays of electrodes or field-effect transistors, any spot on a featureless EIS substrate can be addressed with light. Hence, these techniques possess great potential for biological imaging applications, particularly where there is an interest in investigating processes taking place at the interface between cells and surface – an area generally not accessible to other electrochemical techniques.

LAPS and SPIM have been used to measure cell responses, such as cellular metabolism, extracellular potentials, ionic currents, and cell impedance before, but single cell imaging has not been realized because of a lack of resolution and sensitivity. The main aim of this project was to develop substrates suitable for imaging single cells with LAPS. Initially, the focus was on silicon on sapphire (SOS) substrates modified with organic monolayers due to the good resolution and high sensitivity which have been achieved recently [3, 4]. Later, indium tin oxide (ITO) coated glass substrates were proposed and investigated as alternative semiconductor chips for LAPS and SPIM imaging.

1.2 LAPS and SPIM

1.2.1 Principle of LAPS/SPIM

Hafeman *et al.* [5] developed LAPS by combining the scanned light pulse technique (SLPT) with an electrolyte-insulator-semiconductor (EIS) structure in 1988. A basic setup for photocurrent measurements at EIS field-effect capacitors and a simple equivalent circuit describing the system are shown in Figure 1.1a and b. By applying a DC voltage between a reference electrode immersed in the electrolyte and the semiconductor, a depletion or inversion layer with capacitance C_{SC} is formed at the semiconductor-insulator interface. Electron-hole pairs generated by a light source focused into the semiconductor diffuse to the space charge layer where they separate in the field (see local current source i_P in Figure 1.1b) and cause a current i_{Photo} to flow in the outer circuit, which charges the capacitive structure. Modulating the intensity of the light source results in an AC photocurrent of the modulation frequency that depends on the applied DC voltage as shown in Figure 1.1c.

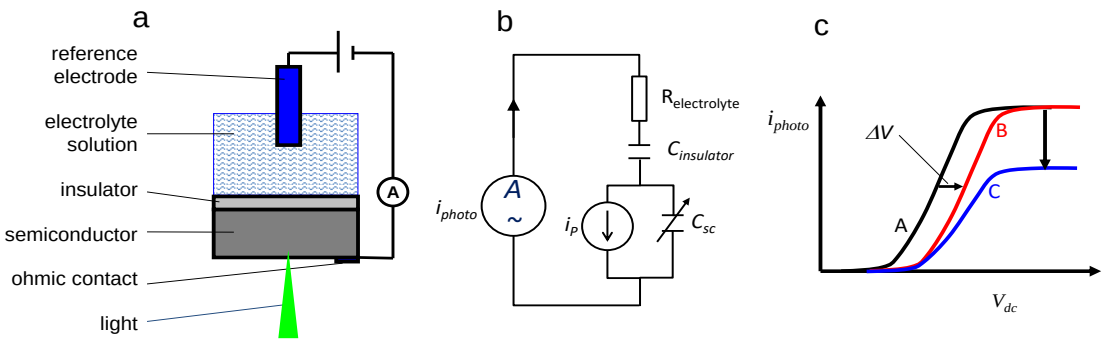

Figure 1.1 (a) Basic setup for LAPS and SPIM measurements; (b) equivalent circuit for photocurrent measurements: i_P is the photocurrent generated in the space charge layer, C_{SC} is the DC voltage dependent capacitance of the space charge layer, and i_{Photo} the current measured in the external circuit; (c) LAPS measure changes in the surface potential (shift from curve A to B) by monitoring the shift of the I-V curve at a constant current or the change in the current at a constant voltage. SPIM monitors changes in the maximum photocurrent (shift from curve B to C), which are directly related to the local impedance of the illuminated part of the sensor chip.

The position of the photocurrent-voltage (*I-V*) curve on the voltage axis depends on the potential difference between insulator surface and solution, an effect that has been exploited for the measurement of various ion concentrations including pH [6, 7], charged molecules such as DNA [8], cell surface charges [9] and extracellular potentials [10]. This measurement mode is known as LAPS. LAPS images can be recorded either by monitoring photocurrents at a constant DC voltage in the depletion region of the *I-V* curve or by monitoring voltage changes while the photocurrent is kept constant.

Another measurement mode known as SPIM exploits the dependence of the maximum photocurrent observed in inversion on the local impedance of the insulator or anything in contact with the insulator [11]. Hence, recording photocurrent while applying a DC voltage corresponding to the saturation region of the *I-V* curve can be used to generate impedance images of the surface.

In complex systems where both the impedance and surface potential might change at the

same time, recording LAPS images becomes more complicated as changes in the maximum photocurrent caused by local impedance changes will also change the photocurrent corresponding to a particular charge state of the surface. In these cases, recording the phase shift between modulated light and photocurrent can be used as an alternative measurement mode [12, 13] as the phase has been shown to be relatively independent of local impedance changes [3] and is less sensitive to the fluctuation of light intensity and distribution of defects in the silicon substrate [12-14].

Spatial resolution and measurement speed are the two most important properties of LAPS and SPIM imaging for biological applications and will be explored in the following sections.

1.2.2 Spatial resolution of LAPS/SPIM

The two main factors that limit the resolution of LAPS and SPIM are the lateral diffusion of minority charge carriers out of the illuminated area in the semiconductor substrate and the quality of the light focus for charge carrier excitation. The resolution has been investigated theoretically and experimentally for front and back side illumination of the EIS structure. Front side illumination is not practical for biological applications as irradiating living cells or microorganisms may adversely affect their normal activity, and light scattering in the electrolyte solution may degrade the spatial resolution. The discussion below will therefore concentrate on the case of back side illumination, which has been adopted for most recent LAPS and SPIM investigations.

Lateral resolution has been defined differently depending on the experimental techniques used to determine it. Frequently, a photoresist pattern is deposited onto the insulator. Resolution can be defined as the distance required for achieving a photocurrent drop to 1/e of the total drop when scanning from an area with high photocurrent to an area with low photocurrent [4, 15] or the smallest size of the pattern that LAPS can resolve [16]. In other publications, resolution was determined by scanning a focused laser beam across

the edge of a metal gate and measuring the decay of the photocurrent outside the gate area [11, 17].

1.2.2.1 Optimisation of the semiconductor substrate

Theoretical calculations have shown that the resolution for a thick semiconductor substrate is determined by the bulk diffusion length of charge carriers [18]. This is problematic in single crystalline silicon where the bulk diffusion length can be hundreds of micrometres. An improvement in the resolution can be obtained by limiting charge carrier generation to the space charge layer, which is difficult to achieve with back side illumination. Increasing the doping concentration in silicon also results in a higher spatial resolution [19-21]. The impurities work as scattering centres for free carriers, leading to a short recombination lifetime and thus a smaller diffusion length of the minority charge carriers, e.g. for n-type silicon with a resistivity of 0.014 Ω·cm, a diffusion length of 14 µm was determined from a measurement of the photocurrent decay outside the gate area [18]. However, with a higher concentration of dopants in the semiconductor, more minority charge carriers produced by illumination will recombine resulting in a reduction of the photocurrent and, hence, a loss of sensitivity.

Direct semiconductor materials, which have smaller bulk diffusion lengths compared to the traditionally used single crystalline silicon, such as GaAs [22], GaN [23] and amorphous silicon [17, 24, 25], have been investigated as possible LAPS substrates. Moritz *et al*. [22] measured a diffusion length of 3.1 µm using GaAs as the LAPS substrate and a resolution of less than 1 µm with amorphous silicon [17], which has been reported to have a diffusion length of 120 nm [26]. However, the problem of the poor quality of the insulators that can be deposited on these materials, which result in a large number of interface states and high leakage currents, has not been solved to date. Zhou *et al*. [27, 28] demonstrated the use of an amorphous silicon n-i-p/SiO_2 photodiode structure for SPIM measurements and achieved a resolution of about 10 µm. As the photocurrent

is not generated at the insulator/semiconductor interface, a good quality insulator is not required in this case. However, the resolution was strongly dependent on the modulation frequency due to the conductivity of the topmost semiconducting layer in the diode structure. The n-i-p/SiO_2 substrates can only be used for local impedance measurements, but not for LAPS as the photocurrent does not change significantly with the applied DC voltage.

Thinning single crystalline silicon is currently the most effective method for improving the spatial resolution of LAPS [4, 6, 11, 15, 16, 21, 29-31]. With a thicker substrate, the charge carriers generated by light illumination travel a longer distance to the space charge region, causing a larger lateral spread and thus a decreased resolution. By thinning the silicon from 500 µm to 100 µm and further to 20 µm, spatial resolutions of 300 µm, 100 µm and 10 µm were achieved by Nakao *et al.* [29]. However, very thin silicon is fragile and not easy to handle. This problem can be solved by the use of silicon on insulator (SOI) or silicon on sapphire (SOS) with a thin device layer. Ito employed a 0.5 µm thick silicon film on the transparent substrates sapphire and quartz to achieve a resolution of 5 µm [16], although in this system, the semiconductor substrate consisted of doped islands functioning like a microelectrode array rather than a homogenous LAPS substrate. Krause *et al*. [11] reported the use of an SOI substrate with a 7 µm thick device layer where a window was etched into the handle to obtain a free-standing silicon membrane accessible to back side illumination with light of short wavelengths. The effective diffusion length of minority charge carriers was measured to be 13 µm. The disadvantage of these devices was that the thin silicon membrane was easily distorted making the devices difficult to handle.

Thin, single crystalline silicon layers on a transparent substrate such as sapphire offer the advantage of mechanical stability while at the same time making the silicon layer accessible to back side illumination with a wide range of different wavelengths. Measuring the decay of the photocurrent outside the gate area, a diffusion length of

0.57 µm was measured with a 1 µm thick silicon layer on sapphire [11]. The best resolution reported to date for a LAPS/SPIM experiment with back side illumination is 0.8 µm obtained with an SOS substrate with a 0.5 µm thick silicon layer [4, 15]. Initial use of this substrate was fraught with problems as it is difficult to grow a standard thermal oxide on SOS most likely due to a mismatch of the thermal expansion coefficients of silicon and sapphire resulting in a large number of interface states and high leakage currents. Hence, alternative insulators have been used with SOS including a good quality anodic oxide [15] and, more recently, self-assembled organic monolayers [4]. The high resolution was not only due to the choice of semiconductor substrate, but also due to the optimized optical setup, which will be discussed in the next section.

1.2.2.2 Optical setup

The focus and the wavelength of light are important aspects for achieving good lateral resolution with LAPS. Decreasing the spot size of the light source is a direct way to enhance the resolution of LAPS. Nakao *et al.* [30] employed a focused laser beam of 1 µm as the illumination source for LAPS for the first time, making the transition from a macroscope to a microscope. The effect of the wavelength of light on the resolution has been investigated theoretically and experimentally [4, 15, 19, 20, 29].

LAPS resolution in bulk silicon. Despite the short diffusion lengths measured with thin silicon layers in SOI and SOS, a lot of effort has been directed at the improvement of the resolution using bulk silicon substrates. To a large extent, this is due to a cost consideration as bulk silicon lends itself much more to the mass production of cheap sensor devices. For bulk silicon substrates, increasing the wavelength leads to improved resolution as light with longer wavelength can travel deeper into the silicon and thus generate charge carriers nearer to the space charge region [19]. Krause *et al.* [11] attempted to confine charge carrier generation to the space charge layer using a two-photon effect in silicon. For single photon absorption, charge carriers are produced

throughout the bulk of the silicon. Using a laser with energy smaller than the bandgap of silicon, two-photon absorption is required for generating electron-hole pairs, thus limiting charge carrier generation to the focus of the laser. Placing the focus close to the space charge region, a significant improvement in the resolution was expected. However, using a 1560 nm femtosecond laser, this approach resulted in an improvement of the resolution of only 31% compared to the results obtained using a 632 nm He-Ne laser, indicating that a large number of charge carriers were still created outside the space charge layer. Using an objective with a larger numerical aperture to focus the laser was proposed for further improving the resolution.

Recently, improvement of the resolution of LAPS by using a ring of constant illumination around the modulated light probe has been suggested for thick silicon substrates (200 µm) [32]. The constant illumination is meant to suppress the lateral diffusion of charge carriers by enhanced recombination in the area of constant illumination. Simulations suggest that improvement in resolution is possible, but would be limited to 50 µm for a 200 µm thick silicon substrate due to the flooding of the central illuminated area with charge carriers through lateral diffusion causing a decrease of the amplitude of the photocurrent because of enhanced recombination. Experiments using fibre-optic illumination verified an improvement of the resolution from 92 µm without to 68 µm with a ring of constant illumination [33].

LAPS resolution in thin silicon substrates. An improvement of the resolution with decreasing wavelength was reported for silicon substrates of 50-200 µm thickness by Guo *et al.* [19], who attributed this effect to a thinning of the space charge region, as longer wavelengths can penetrate deeper into the silicon and produce larger carrier concentrations in the space charge region around the illuminated point. In the same paper, Guo *et al.* also showed that decreasing the light intensity led to an improvement in the resolution because of a reduction in the carrier concentration in the space charge region.

The wavelength dependence of the resolution was also investigated for SOS substrates

with silicon layers of 0.5 and 1 µm thickness [4, 15]. Focusing the laser beam through the solid sapphire substrate required a microscope objective with correction to minimise spherical aberration and achieve the best possible focus. In a wavelength range from 405 nm to 1064 nm an improvement of the resolution with decreasing wavelength was observed. For these ultrathin silicon layers, the penetration depth of the laser becomes less important and the wavelength dependence is more likely due to the Rayleigh criterion for a focused laser beam:

$$r = \frac{0.61\lambda}{NA}$$

where r is the resolution, λ the wavelength and NA the numerical aperture of the microscope objective used.

At 405 nm, a resolution of 1.5 µm was obtained measuring photocurrent changes while scanning a focused laser beam across an SOS substrate with an SU-8 photoresist pattern (Figure 1.2) [15]. Further improvement of the resolution to 0.8 µm was observed using a two-photon effect for charge carrier excitation with a femtosecond laser at 1250 nm (Figure 1.2 b). The non-linear absorption improved the effective focus of the laser beam and drastically reduced any effects from light outside the central focus of the laser beam.

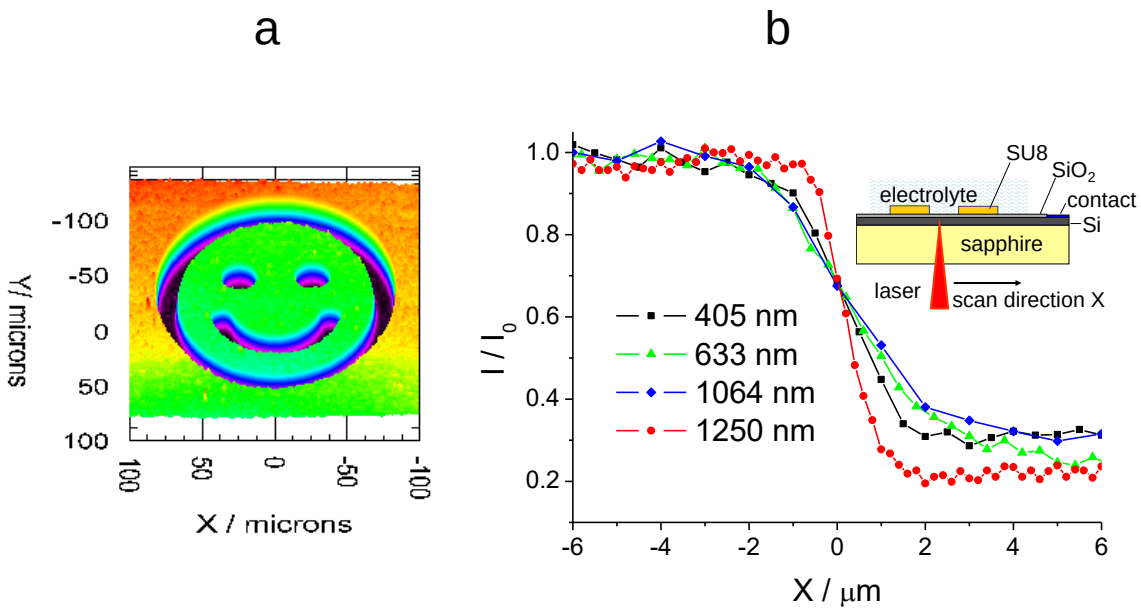

Figure 1.2(a) Photocurrent image of an SU-8 pattern on an SOS substrate with a 0.5 µm thick silicon layer and an anodic oxide and (b) photocurrent line scans across the edge of the photoresist at different wavelengths[15].

1.2.3 Temporal resolution

A typical experimental setup for high-resolution LAPS and SPIM imaging is shown in Figure 1.3 [3]. The stationary laser beam is focused into the semiconductor through a microscope objective. The LAPS substrate is mounted on an XYZ positioning system that allows imaging by moving the sensor with respect to the laser beam. Alternatively, the laser beam can be scanned across the sensor with a pair of galvano mirrors when imaging small areas [6]. The major problem with this approach is the low measurement speed due to the fact that the two-dimensional images are obtained by scanning pixel-by-pixel, and each photocurrent value needs to be measured in each spot. Furthermore, the frequency used in LAPS is in the order of kHz which makes this technique time-consuming. A typical scan time at a resolution of 128x128 pixels is about 3 min when 10 ms of sampling time is spent for each pixel. This slow imaging speed makes it difficult to use this setup for the investigation of fast processes such as chemical phenomena or visualizing the activity of biological systems.

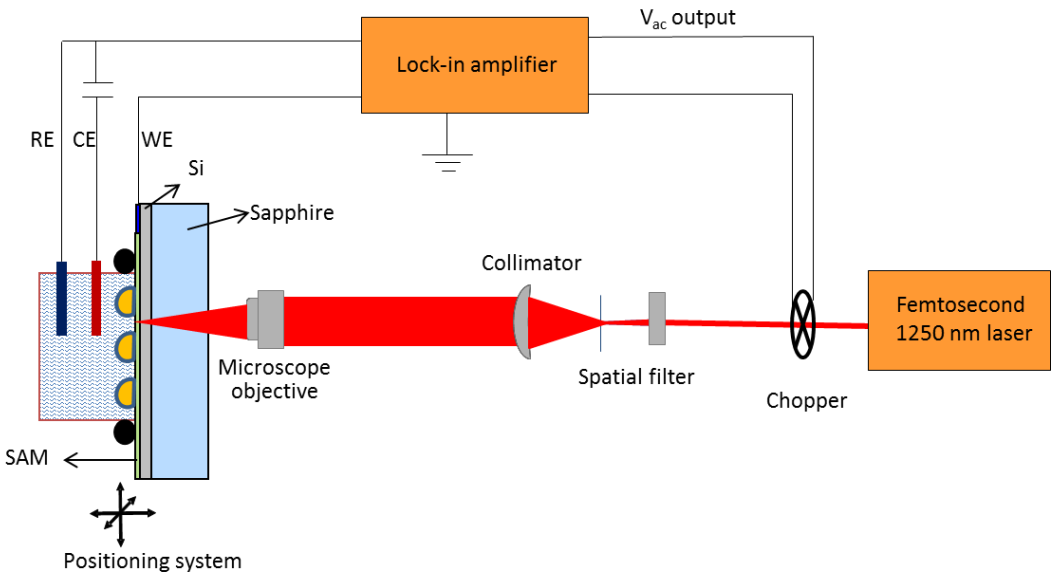

Figure 1.3 Experimental setup for high-resolution LAPS and SPIM measurements [3]. (V_{AC} – AC voltage, RE – reference electrode, CE – counter electrode, WE – working electrode, SAM – self assembled monolayer)

Das *et al.* [34, 35] developed a fast measurement system based on a gimbal-less two-axis electrostatic comb driven micromirror for scanning a focused laser beam across the LAPS substrate from the back side (Figure 1.4). This system was able to measure the spatiotemporal change of pH in a solution with a speed of 16 frames per second (fps). In addition, a chemical image with 200,000 pixels of a photoresist pattern on the sensor surface was generated within 40 s. To avoid mechanical movement altogether, commercially available projectors and displays were suggested to illuminate different spots on the LAPS substrate [24, 36-38]. A digital micromirror device (DMD) [36], a pico-projector based on digital light processing (DLP) [24], an OLED display [38, 39] and a liquid crystal based projector [37] were employed to address different spots on the sample. All these devices have the advantage that they are capable of addressing a large number of measurement spots. While the modulation frequency for the DMD and the liquid crystal projector have to date been limited to maximum values of 720 Hz and 30 Hz, respectively, resulting in relatively long sampling times, a customized driver circuit allowed for modulation frequencies of 1 kHz to 16 kHz for an OLED display [40].

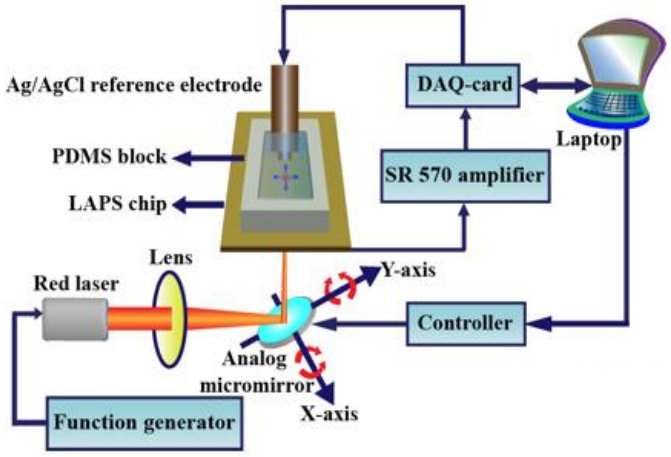

Figure 1.4 High-speed laser scanning setup for LAPS using a two-axis analogue micromirror [34]. (PDMS - polydimethylsiloxane, DAQ – data acquisition)

A different approach for increasing the imaging speed is the use of arrays of light sources to illuminate different spots on the LAPS substrate simultaneously. Zhang *et al.* [41] first introduced this method by illuminating the LAPS chip with three light pointers, each modulated at a different frequency. A fast Fourier transformation (FFT) algorithm was used to restore individual signals from a superposition of the signals at different frequencies. This frequency division multiplex has been used for the development of a number of fast imaging systems. Wagner *et al.* [42] employed a 4x4 LED array with each LED modulated at a different frequency for fast simultaneous measurement of 16 sensor spots. A combination of multiple light sources modulated at different frequencies and mechanical scanning was proposed by Miyamoto *et al.* [43], who scanned a linear LED array with 3.6 mm spacing across a LAPS substrate to achieve fast imaging. A scan time of 6.4 s at a resolution of 16 pixels×128 lines was reported. The measurement spot density for this approach was increased by miniaturising the light sources using an array of vertical cavity surface emitting lasers (VCSELs) with a pitch of 250 µm [44]. Recently, a high-speed chemical imaging system based on 64 light beams guided by an array of optical fibres was developed to measure dynamic pH changes inside a microfluidic channel formed on a LAPS substrate (Figure 1.5) [45]. Using optical fibres allows for the layout of the light sources to be adapted to a specific measurement problem. Frame rates

of 100 fps were achieved using this system.

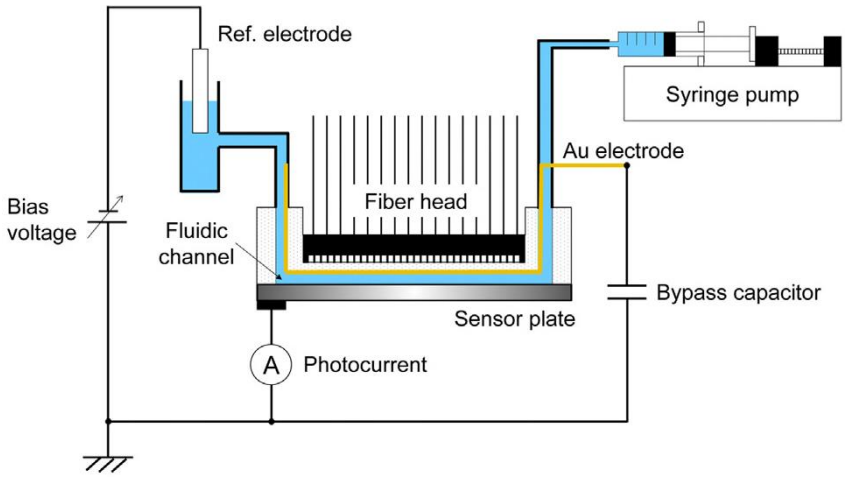

Figure 1.5 Optical fibres mounted above the LAPS substrate in a microfluidic channel for dynamic monitoring of pH changes [45].

1.2.4 Applications of LAPS/SPIM

1.2.4.1 The detection of surface potentials

As the *I-V* curve of LAPS responds to the surface potential, the pH could be monitored by a potential shift with a pH-sensitive silicon oxynitride insulating layer in accordance with the Nernst equation, which has since become a standard test. Potassium ions were measured with a Nernstian potential response with a valinomycin containing a K^+-selective membrane. Redox pairs such as ferricyanide-ferrocyanide were also measured by depositing metal pads over the insulator. The enzymatic reaction of urea with urease was monitored by measuring pH changes caused by the production of ammonia. The following section will focus on the applications of LAPS in the detection of pH, ions, redox pairs, and enzymatic reactions.

Ion detection. LAPS has been widely used to detect various ions such as K^+, Ca^{2+}, Mg^{2+} [46], Pb^{2+} [47], Li^+ [48], Na^+ [49], Cs^+ [50], Hg^{2+} [51], Fe^{3+}, Cr^{6+} [52, 53], Cd^{2+} [42, 54], F^- [55], Cl^- [56], NO_3^-, and SO_4^{2-} [57] by depositing ion-selective films on the gate

insulator. The potential shifts resulting from ion binding were measured. For example, polyvinyl chloride (PVC)-based membranes with ion-recognition elements (valinomycin, 18-crown-6 ether, bis[di-(n-octylphenyl)phosphato]calcium(II) (HDOPP-Ca), *N,N′*-diheptyl-*N,N′*-dimethyl-1,4-butanediamide (ETH1117)) were prepared on an $Al_2O_3/SiO_2/Si$ structure to detect K^+, Ca^{2+} and Mg^{2+} based on a LAPS system [46].

Redox potentials. LAPS was developed to detect redox potential changes in solution, which required a partial gold-deposited layer compared to the conventional EIS structure [5, 58]. Different ratios of the redox pair ferricyanide-ferrocyanide could be monitored by the potential shift of *I-V* curves, which can be further used in the detection of enzymatic reactions involving redox active species. The distribution of the redox potential with a gold layer on the insulator cannot be determined, as the redox potential would be the same everywhere on the gold. Oba *et al.* [59] demonstrated that redox potentials in the presence of ferricyanide-ferrocyanide could also be measured without the presence of a gold layer, even though the mechanism of potential formation was not clear in this case.

Enzymatic reactions. Enzymatic reactions have been monitored by LAPS based on pH [60] and redox potential sensing [58]. LAPS has been used to detect enzymes, the substrates, the products and the inhibitors of enzymes and the rate of enzymatic reactions. The investigations included urease [61], acetylcholinesterase (AchE) [62-64], ethanol dehydrogenase (ADH) [65], glucose oxidase, penicillinase [66-68], horseradish peroxidase (HRP) [58], α-chymotrypsin, butyrylcholinesterase [69], β-D-fructofuranosidase, α-D-glucosidase, and glucokinase [70]. Seki *et al.* [66] used a pH-sensitive surface for the detection of urea, penicillin and glucose by immobilizing urease, penicillinase and glucose oxidase, respectively, on the insulator. Enzymatic reactions in organic media were also recorded using LAPS [69].

LAPS have been used as detectors in Enzyme Linked Immunosorbent Assays (ELISA). A commonly used model employed urease as the label to produce a LAPS signal (Figure 1.6) [71]. Immunosensors with LAPS detectors were applied to the measurement of

various antigens including an antibody to the Hepatitis-B virus envelope protein [72], asialofetuin [73], DNA [74], plasmids [75], Newcastle disease virus [76], Venezuelan equine encephalitis virus [77], spores and cells [78], *E.coli* [79-81], salmonella [82], *B. subtilis* [71], and terbuthylazine [83]. Redox based HRP was also used as a label enzyme in the model to detect 2,4-dichlorophenoxyacetic acid (2,4-D) [65, 84].

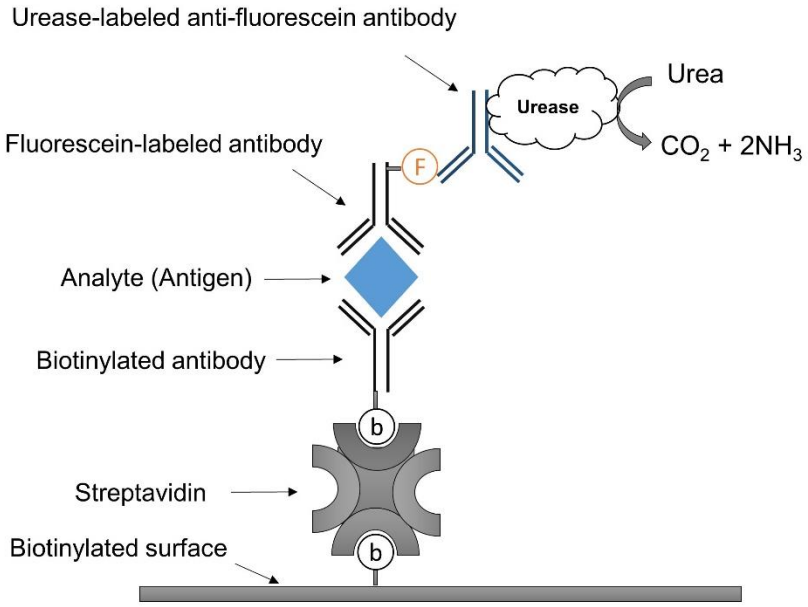

Figure 1.6 The sandwich ELISA model used in LAPS. (F – fluorescein, b – biotin)

Cellular Metabolism. Cellular metabolism produces acid as an excretion in the form of protons, lactic acid or CO_2 through glycolysis and respiration. The extracellular acidification response to cellular metabolism could be monitored with pH-sensitive LAPS [7, 42, 65, 85-89], and the influence of drugs, toxins or growth factors on cellular metabolism could be evaluated [90-94], which was called a microphysiometer. Seki *et al.* [95] developed a LAPS microbial assay for tryptophan sensing based on extracellular pH changes. The sensor detected the acidification rate of *E.coli* WP2, which was dependent on the growth of *E.coli* WP2 and tryptophan concentrations. A multichannel microphysiometer based on multi-LAPS was developed to measure several extracellular ions concentrations (H^+, K^+, Ca^{2+}) simultaneously in living cells under the influence of drugs [96].

Extracellular potentials and ionic currents. Tanaka *et al.* [97] applied LAPS to the measurement of the membrane potential of *Aplysia*'s neural cells. The sensor output photocurrent related to the surface potential decreased along with the cell membrane potential. However, the surface potential shift was only 1.3% of the change of the membrane potential.

Parak *et al.* [18] raised the question whether LAPS can detect extracellular potentials of cardiac myocytes, which have already been demonstrated with field-effect transistors and substrate-integrated microelectrodes. Time dependent LAPS photocurrent signals that correlated with contractions of cardiac myocytes were observed. Unfortunately, the LAPS substrate was illuminated from the front in this case, making it impossible to separate effects from changes in the extracellular potential and the shape of the cells during the mechanical contractions.

In 2003, Ismail *et al.* [98] developed a poly-L-ornithine and laminin (PLOL) coated SiO_2/Si structure to improve the sensitivity and biocompatibility for neural cells, which made LAPS sensitive enough to measure the small change of surface potential due to the extracellular transients of the neural action potential. Later, LAPS was shown to be capable of detecting small surface potential that could be correlated to extracellular potentials or averaged ion currents of neuronal cells upon periodic stimulation [10]. Very small surface potential changes of about 10 μV were reported, which were thought to be due to insufficient attachment of the cells to the sensors surfaces.

Xu *et al.* [99] studied extracellular action potentials of single living rat cortical neurons under acetylcholine as stimulus. The extracellular potential LAPS system was used as an olfactory cell-based biosensor for odorant stimulus monitoring (acetic acid, glutamic acid, butanedione) [100-102]. Mouse embryonic stem cells were cultured on the surface of the LAPS and induced to differentiate into cardiac myocytes and neurons. Extracellular potentials of the cells were recorded, and the characteristic effect of cardiac stimulants (isoproterenol) and relaxants (carbamylcholine) on the cardiomyocytes was

investigated [103], although front side illumination of the LAPS again made it impossible to distinguish between extracellular potentials and shape changes in the beating cardiac myocytes. The cardiac cell-based biosensor was also used for detection of heavy metal toxicity (Hg^{2+}, Pb^{2+}, Cd^{2+}, Fe^{3+}, Cu^{2+}, Zn^{2+}) through extracellular potentials by LAPS [104]. The same setup was used to detect extracellular potentials of taste receptor cells and their response to taste stimuli of NaCl, HCl, $MgSO_4$, sucrose, glutamate, and acidic sensation [105, 106].

Label-free detection of proteins, DNA and cells by potential shift. Recent research results suggested that the immobilization of charged molecules and cells onto the LAPS surface could directly induce a change of the surface potential. This has been applied to the detection of proteins, DNA and cells by potential shift directly without labels. Alpha fetoprotein (AFP) was detected by a surface potential change caused by binding to immobilized antibodies on a membrane. The response to 400 µg/L of AFP was about 11 mV [107]. Jia *et al.* [108] developed phage-modified LAPS to detect the cancer marker hPRL-3 in a concentration range of 0.04 – 400 nM with a maximum response of 10 µV, and cancer cells (mammary adenocarcinoma) in the range of $5 \times 10^3 – 5 \times 10^5$ /mL with a maximum response of 60 µV, respectively. L-DOPA-activated LAPS were applied to detect unlabelled rabbit anti-mouse IgG [109]. LAPS has also been used for the detection of four tumour markers (AFP, carcinoembryonic antigen, cancer antigen 19-9, and Ferritin) [110] and human IgG [111]. Non-labelled DNA biosensors based on LAPS were developed to detect the hybridization of probe DNA and target DNA [8, 112-116]. Potential shifts were caused by the intrinsic negative charge of DNA. Using anti-ATP aptamer as recognition element immobilized on the surface of LAPS, local ATP secretion from a single taste receptor cell can be detected by measuring the potential shift [117]. Hg^{2+} was detected with an aptamer modified LAPS. The surface potential was influenced by the aptamer's morphology and charge [118]. A carboxylated graphene oxide (GO-COOH) modified LAPS substrate was developed for the label-free detection of circulation tumour cells by measuring potential shifts [119].

The surface potential shift of LAPS has been related to the Nernst potential due to ion binding to surface states of the insulator, to ion exchange equilibria with ion selective membranes, to redox potentials, to extracellular potentials or ionic currents of excitatory cells, and further to the surface charge status of immobilized molecules and cells in a broad sense.

1.2.4.2 The detection of local impedance

SPIM has been applied to the measurement of local impedance [11, 27, 120]. The potential of the technique for interrogating sensor arrays was demonstrated by depositing an array of polymer dots of cellulose acetate and an α-chymotrypsin sensitive poly (ester amide) on a SPIM substrate and monitoring their enzymatic degradation by recording changes in the maximum photocurrent and impedance [28].

Yu *et al.* [121] used impedance measurement with SPIM to monitor the cell adhesion of rat kidney cells, which showed a 10% change of impedance. The real-time monitoring of cellular impedance and cellular acidification for cell growth and metabolism were combined into one sensor named light-addressable potentiometric and cellular impedance sensor (LAPCIS) [122].

SPIM was also used for the characterization of microcapsules [3] and yeast cells [9] on organic monolayer modified silicon on sapphire (SOS) surfaces. The use of organic monolayers as the insulator decreased the impedance of the insulator substantially and resulted in an improved sensitivity for local impedance changes.

1.2.4.3 Multichannel detection

The sensing area of LAPS depends on the illuminated area, which is natural for multichannel detection [5, 123]. This was achieved experimentally for pH detection [124] and impedance measurements (see section 1.2.4.2.) [28] of selected areas at the same time with a single semiconductor device. Stein *et al.* [85] monitored metabolic activity of two

different co-cultured cellular populations seeded on different segments of one LAPS device. Yu *et al.* [88] designed a multifunctional integrated LAPS system for simultaneously detecting cell acidification and extracellular potential of cardiac myocytes. Yoshinobu *et al.* [125] developed a portable 4-LED LAPS to detect four different ion species by integrating different ion-selective materials on the sensing surface. Jia *et al.* [110] described a label-free multi tumour marker parallel detection system based on LAPS (see section 1.2.4.1).

A handheld 16-channel 'chip card'-based LAPS device for the simultaneous real-time measurement of 16 sensor spots (see section 1.2.3.) was used for the detection of different Cd^{2+} concentrations and metabolic activity of Chinese hamster ovary (CHO) cells at different locations of the sensor surface [42, 126-128].

1.2.4.4 LAPS imaging

In 1994, Nakao *et al.* [6] first constructed a two-dimensional (2-D) pH-imaging sensor to observe H^+ distribution produced by colonies of yeast (Figure 1.7) and later *E. coli* [129] through scanning a laser beam focused to a spot of ~1 μm diameter. The scanning-laser-beam LAPS imaging system was applied to urea imaging using the pH change caused by the reaction with urease [130], redox potential imaging of $K_3Fe(CN)_6$/ $K_4Fe(CN)_6$ [59], and dynamic imaging of the Belousav-Zhabotinsky reaction [131]. Yoshinobu *et al.* [132] applied the pH-imaging sensor to the visualization of ionic diffusion in an electrochemical system. The diffusion coefficients of ions were investigated, which demonstrated the applicability of the pH-imaging sensor in the quantitative analysis of chemical dynamics.

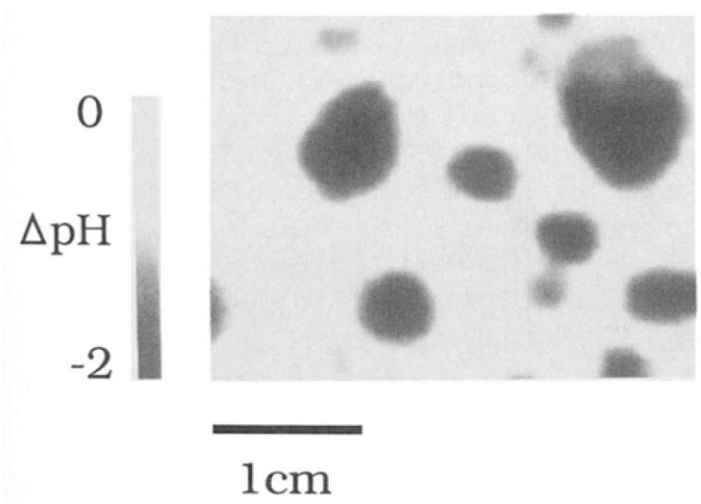

Figure 1.7 A pH image of colonies of yeast. Each dark region corresponds to a colony [6].

Tanaka *et al.* [97] measured the extracellular potential of *Aplysia*'s neural cells. A photocurrent image of the cultured cells was related to the surface potential shift and the charge of the cells. SPIM and LAPS using organic monolayer modified SOS substrates were used for the imaging of microcapsules (diameter ~ 10 μm) with high lateral resolution (Figure 1.8) [3]. The same substrates were shown to be sensitive enough to image patterned self-assembled organic monolayers obtained by microcontact printing (μCP) [4, 133, 134]. Modifying SOS substrates with an inert monolayer of 1,8-nonadiyne resulted in a pH-insensitive surface which was used for imaging both, the surface charge and the impedance of colonies of yeast cells [9].

High-speed LAPS imaging was used to record a movie of the pH distribution inside a microfluidic channel at 100 fps (Figure 1.9) by illuminating 64 points simultaneously using optical fibres (also see section 1.2.3) [45]. The visualization of the catalytic reaction of urease in a microfluidic channel by high-speed LAPS imaging was achieved using an OLED panel as the light source [135].

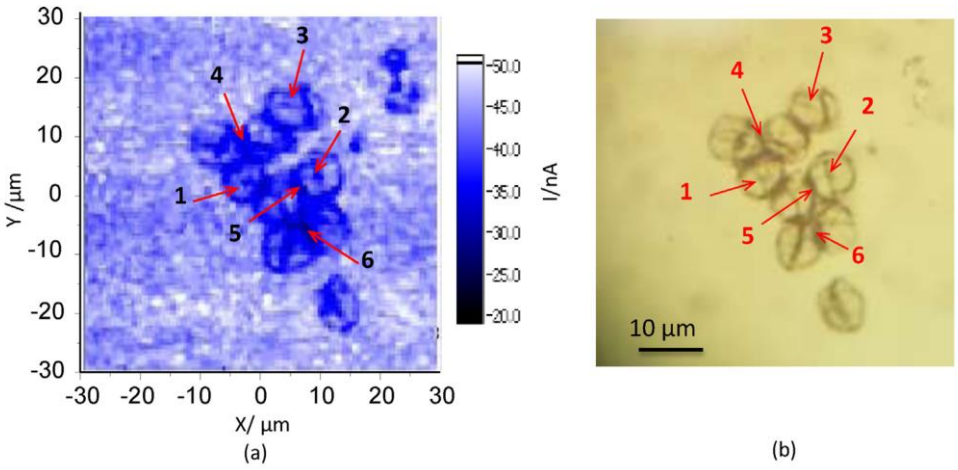

Figure 1.8 Microcapsules attached on a COOH-terminated SOS substrate. (a) SPIM image measured at 0.9 V, (b) corresponding optical image [3].

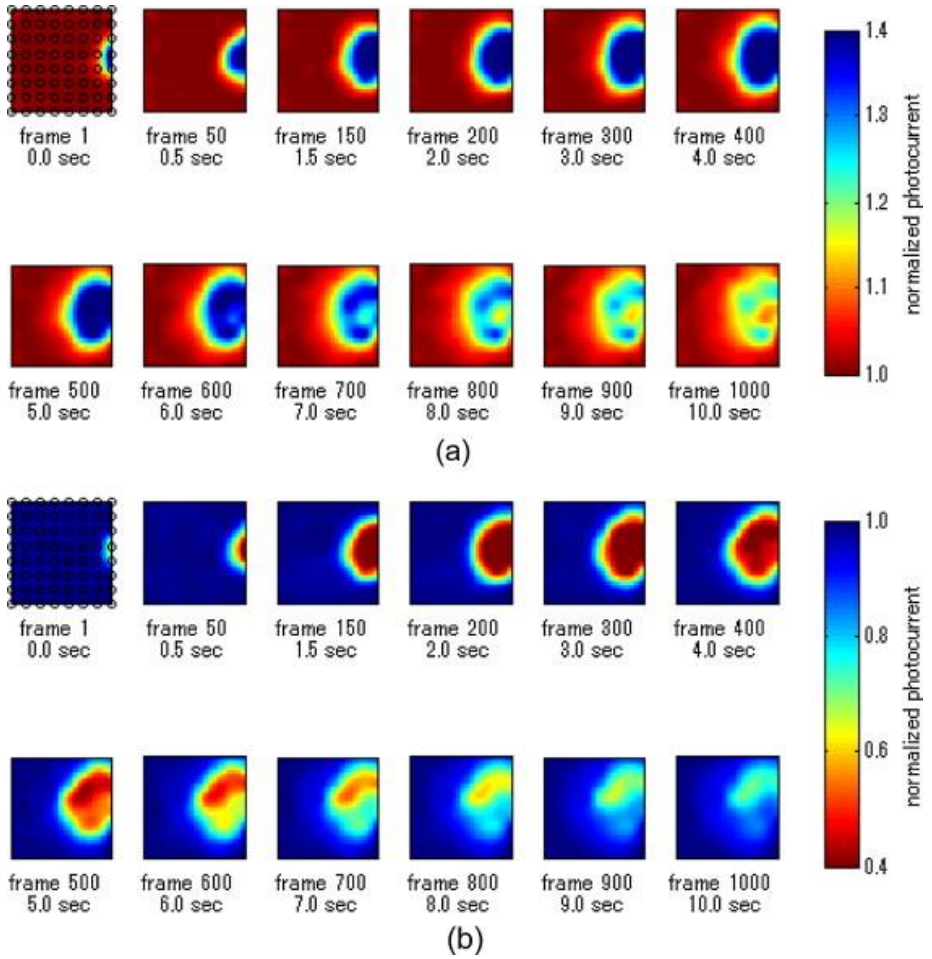

Figure 1.9 Visualization of buffering action at 100 fps. (a) Injection of 10 mM NaOH solution into phosphate buffer and (b) Injection of 10 mM HCl solution into phosphate buffer [45].

1.3 Modification of silicon surfaces with self-assembled organic monolayers (SAMs)

"Self-assembled organic monolayers are ordered organic molecules assemblies that are formed spontaneously by the adsorption of a surfactant with a specific affinity of the molecules to a substrate" [136]. The SAM molecules contain head groups, backbones and end groups (Figure 1.10), where the head groups are the reactive sites with a strong affinity for the substrate, backbones play an important role in the ordering and packing of the molecules on the surface and end groups can be tuned to control the surface properties. Silicon is the most widely used semiconductor material. Modification of silicon with SAMs has been employed for various applications, such as surface passivation [137-141], electronics [142-145], sensors [146-148] and biomedical devices [149-152]. One of the most studied SAMs on silicon is the alkylsiloxane monolayer formed on silicon dioxide surfaces [153-158]. However, it suffers from reproducibility and stability problems related to the siloxane polymerization and the facile hydrolysis of the Si-O-Si bond [159-162]. To solve these problems, deposition of SAMs directly on oxide-free silicon has been developed, which is mainly achieved by hydrosilylation and a halogenation/alkylation approach on hydrogen-terminated silicon surfaces (H-Si), which will be discussed hereafter.

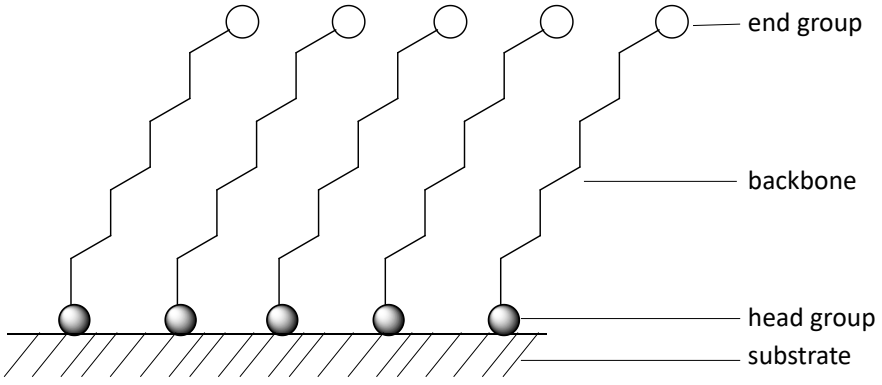

Figure 1.10 Schematic representation of the structure of SAMs deposited on solid substrates [136].

1.3.1 Deposition of SAMs on oxide-free silicon surfaces

1.3.1.1 Hydrosilylation on H-Si

Direct hydrosilylation of H-Si surfaces is one of the most appealing approaches to deposit SAMs on oxide-free silicon. The H-Si surfaces are typically prepared by chemical etching silicon in fluoride-containing solutions, such as dilute (< 10%) hydrofluoric acid or 40% ammonium fluoride solutions [159, 163, 164]. Hydrosilylation can be generally classified into thermal hydrosilylation, photo-activitated hydrosilylation and electrochemical hydrosilylation according to the reaction conditions (see Figure 1.11).

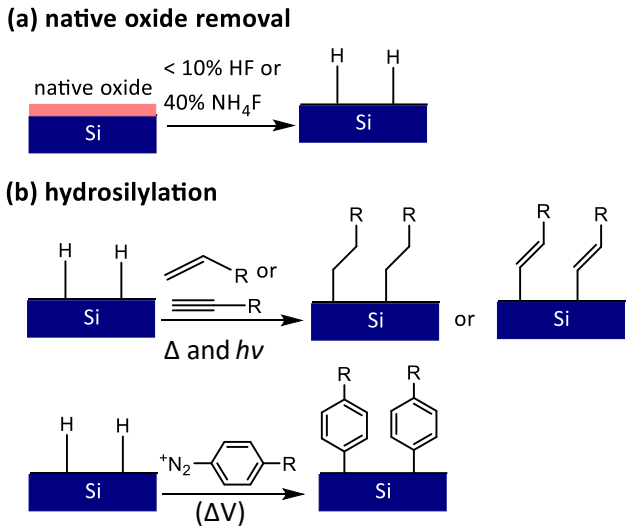

Figure 1.11 Schematic representations of (a) native oxide removal on silicon surfaces and (b) hydrosilylation of H-Si. (R represents functionalized or non-functionalized hydrocarbon chain, Δ, hv and ΔV represent thermal-activated, photo-activated and electrochemical processes, respectively) [165]

Thermal hydrosilylation on H-Si was first reported by Linford *et al.* [166] who prepared alkyl monolayers on non-oxidized H-Si surfaces by the pyrolysis of diacyl peroxide ($[CH_3(CH_2)_nC(O)O]_2$, n = 10 or 16). In their later report, 1-alkenes were grafted onto H-Si surfaces in the presence of a diacyl peroxide radical initiator at 100-200 °C for 1 h [167]. The results from Infrared (IR) spectroscopy and X-ray reflectivity (XRR) showed

that the monolayers were highly stable and densely packed on silicon surfaces. Based on the deuterium labelling experiments, they proposed a radical chain mechanism as depicted in Figure 1.12. First, the silicon radical is formed through the cleavage of a Si-H bond by the diacyl peroxide-derived radical. Then the alkenes react with the silicon radical to form the Si-C bond and a secondary alkyl radical, which will abstract the hydrogen from another Si-H bond and generate a new silicon radical to react with the alkenes. Similarly, high-quality SAMs have also been obtained from alkynes at elevated temperature [168-171], where the silicon radicals are generated by the homolytic cleavage of Si-H bond, which will then react with the alkynes as described above. It has been found that alkynes are more reactive and form more densely packed monolayers on H-Si surfaces than alkenes [172-174]. Functionalized alkenes, such as undecylenic acid, have also been successfully immobilized on H-Si surfaces via thermal hydrosilylation, which produced a carboxyl-terminated monolayer, allowing for further derivatization with diverse biomolecules [175-179]. It is worth mentioning that Gooding's group demonstrated the formation of a robust and well-defined alkyne-terminated monolayer on non-oxidized silicon surfaces through the reaction with a commercially available distal diyne (1,8-nonadiyne) at 170 °C for 3 h [140, 170, 180-184]. The resulting alkyne groups provided a powerful platform for a further Cu(I)-catalyzed azide alkyne cycloaddition (CuAAC) 'click' functionalization.

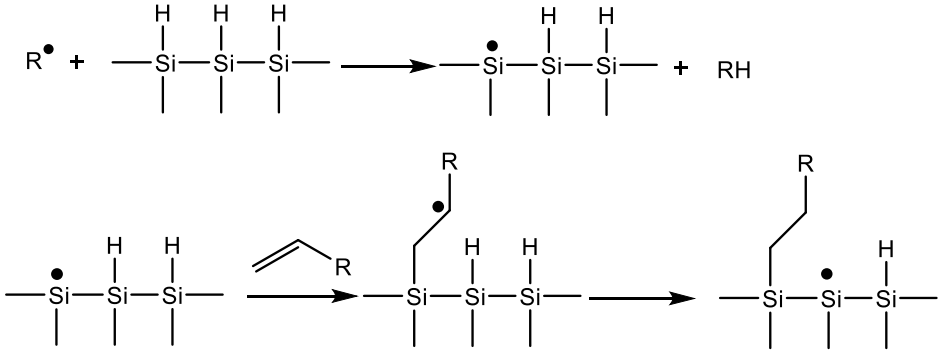

Figure 1.12 Mechanism of hydrosilylation of alkene on H-Si [166, 167].

Photo-activated hydrosilylation has also been widely used to modify Si-H surfaces [185-

188]. Terry *et al.* [185] firstly reported the reaction of 1-pentene with Si-H surfaces under the activation of UV (Hg lamp, λ = 185 and 253.7 nm) for 2 h. The mechanism was initially believed to be that the Si-H bond was broken by the UV irradiation, the energy of which was greater than Si-H bond energy (~3.5eV or λ < 350 nm), producing a silicon radical and initiating the radical chain reaction. Interestingly, visible light can also be employed to activate the attachment of unsaturated hydrocarbon chain on porous silicon as reported by Stewart *et al.* [189] and on crystalline silicon surfaces as discovered by de Smet *et al.* [190]. An alternative exciton-mediated mechanism was proposed since the photon energy of visible light was not enough to promote the homolytic dissociation of surface Si-H bonds [189, 191-193]. In this mechanism, the excitons generated in the semiconductor substrate with visible light initiated the reaction. The above two mechanisms are depicted in Figure 1.13. Although the mechanism of the photochemical hydrosilylation is indefinite, its advantages are obvious, such as the good surface coverage of the monolayers [187], high chemical stability [194] and as it allows for the fabrication of patterned SAMs with optical lithography [195, 196]. It is noteworthy that this method has also been successfully applied to modify other semiconductor materials, such as GaN [197].

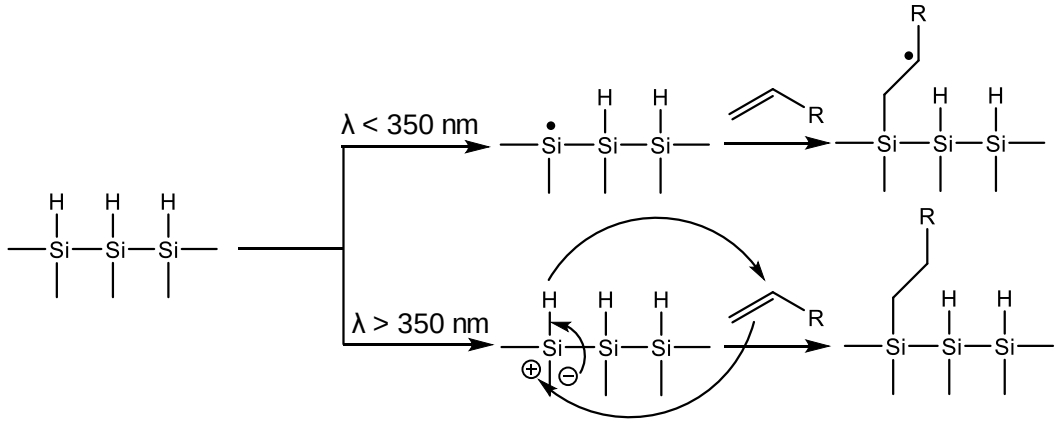

Figure 1.13 Schematic illustration of the two mechanisms, (top) radical-based mechanism and (bottom) exciton-mediated mechanism, for photochemical hydrosilylation of H-terminated Si surfaces [198].

Additionally, SAMs have been deposited on Si-H surfaces using an electrochemical method [199, 200]. Villeneuve *et al.* [199] reported the electrochemical formation of phenyl layers on Si-H surfaces by reduction of commercially available aryl diazonium salts. The mechanism was proposed as follows:

$$\mathrm{N} \equiv N^{+} — \mathrm{Ar} — \mathrm{X} + e^{-} \rightarrow \bullet\mathrm{Ar} — \mathrm{X} + N_2 \quad (1)$$

$$\equiv \mathrm{Si} — \mathrm{H} + \bullet\mathrm{Ar} — \mathrm{X} \rightarrow \equiv \mathrm{Si}\bullet + \mathrm{H} — \mathrm{Ar} — \mathrm{X} \quad (2)$$

$$\equiv \mathrm{Si}\bullet + \bullet\mathrm{Ar} — \mathrm{X} \rightarrow \equiv \mathrm{Si} — \mathrm{Ar} — \mathrm{X} \quad (3)$$

$$\equiv \mathrm{Si} — \mathrm{H} + \mathrm{H_2O} + e^{-} \rightarrow \equiv \mathrm{Si}\bullet + H_2 + \mathrm{OH}^{-} \quad (4)$$

$$\equiv \mathrm{Si}\bullet + \mathrm{H_2O} + e^{-} \rightarrow \equiv \mathrm{Si} — \mathrm{H} + \mathrm{OH}^{-} \quad (5)$$

where X is either a nitro group or a bromine atom, and ≡Si–H refers to the HF etched Si surface. Reaction (1) illustrates the formation of an acyl radical (•Ar-X) in an acid aqueous solution. The generated acyl radical then abstracts hydrogen from Si-H surface in reaction (2), resulting in a silyl radical which reacts with a second acyl radical to form the ≡Si–Ar-X bound (reaction (3)). It should be noted that reaction (4) explained the observed molecular hydrogen evolution with a Heyrovsky mechanism [201]. The resultant silyl radical might also participate in reaction (3) or react with a water molecule to generate more Si-H bonds. This method forms a very stable organic layer on silicon surfaces with no detectable oxidation which resists the etching of 40% HF solution. The big difference between this approach and the thermal hydrosilylation and photochemical hydrosilylation is that the reaction was performed in an aqueous solution and generates a non-oxidized surface. As the Si-C bond is inert to 2.5% HF solution, any silicon oxide formed during the process can be dissolved in HF solution, resulting in a non-oxidized surface. The cathodic potential applied prevented the degradation and oxidation of the surface.

1.3.1.2 Halogenation/alkylation on H-Si

Another important approach to deposit SAMs on non-oxidized silicon surfaces is a two-step reaction involving the halogenation and alkylation of H-Si surfaces, which was initially reported by Bansal *et al.* [202]. In their report, H-Si surfaces were chlorinated by PCl_5 in chlorobenzene using benzoyl peroxide as the radical initiator at a temperature of 80-100 °C to produce the chloro-terminated silicon surfaces (Si-Cl), which were then alkylated by alkyl lithium reagents (RLi, R = C_4H_9, C_6H_{13}, $C_{10}H_{21}$, $C_{18}H_{37}$) or alkyl Grignard reagents (RMgX, R = CH_3, C_2H_5, C_4H_9, C_5H_{11}, C_6H_{13}, $C_{10}H_{21}$, $C_{12}H_{25}$, $C_{18}H_{37}$; X = Br, Cl). The X-ray photoelectron spectroscopy (XPS) and Fourier-transform infrared spectroscopy (FTIR) results showed the high quality of the organic monolayers formed on silicon surfaces. Additional chemical and electrical stability tests also demonstrated the robustness of the organic monolayers. The advantage of this two-step method is its ability to produce a fully passivated non-oxidized silicon surface by reacting all the Si-H sites with single methyl or acetylene groups, which is not accessible for most other surface modification methods [138, 140, 202]. Alkylation on Si-Br or Si-I surfaces has also been performed [165, 203, 204]. However, the most commonly used halogenated silicon surfaces are Si-Cl surfaces, which have been alternatively prepared by reacting Si-surfaces with Cl_2 either thermally or photochemically [203]. Figure 1.14 represents the two-step chlorination/alkylation route on H-Si surfaces. The Si-Cl surfaces have also been reported to react with ammonia or primary amines to generate Si-N bond [205-209], or primary alcohols to produce Si-O-C bond [209-211]. In addition, the halide-terminated silicon surfaces have been further functionalized with alkyne groups [138, 212] and azide groups [213] by reacting with sodium acetylides and sodium azide, respectively, both of which provide a platform for further derivatization with a ‘click’ reaction, which will be discussed in detail in the following section.

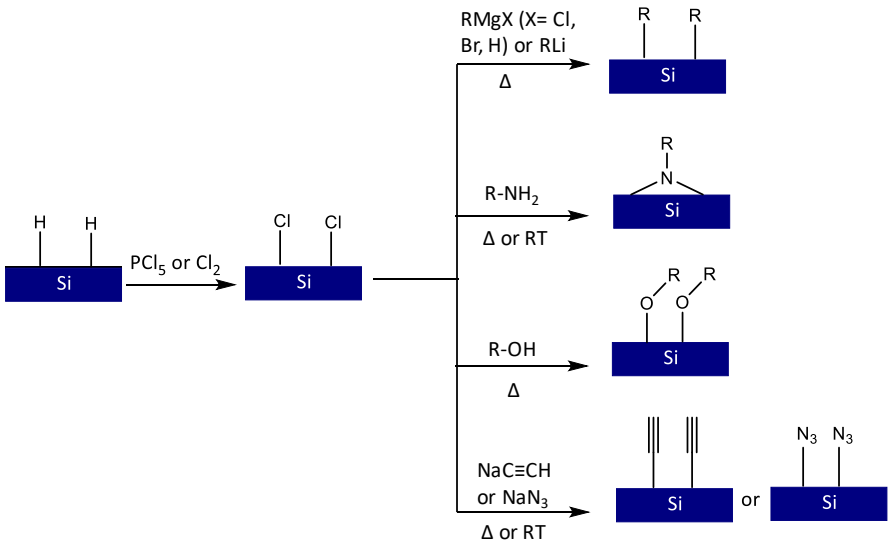

Figure 1.14 Representative modification schemes for Si-Cl surfaces. (RMgX, R = -C_nH_{2n+1} (n = 1–18), –t-Bu, –i-Pr, –C_6H_5, –CH=$CHCH_3$); R-OH, R = –C_nH_{2n+1}) (n = 12, 18); and R-NH_2 (R = –C_4H_9, –C_8H_{17}, –C_6H_5) [140, 165].

1.3.2 Further derivatization of SAMs on silicon via ‘click’ chemistry

To expand the application of the SAMs modified silicon substrates, it is of great importance to further functionalize the SAMs through different surface chemistry, among which ‘click’ chemistry is one of the most attractive routes and will be reviewed hereafter.

1.3.2.1 The mechanism of ‘click’ chemistry

‘Click’ chemistry, especially the CuAAC reaction, has been used extensively to modify silicon surfaces [146, 147, 175, 212, 214, 215], due to its many advantages, such as high selectivity and yield, mild reaction conditions and good compatibility with various solvents, since it was first described by Sharpless’ group in 2001 [216]. The latest generally accepted mechanism was proposed by Worrell *et al.* [217] as depicted in Figure 1.15. In this mechanism, there are two copper atoms involved in the catalytic cycle, where the first copper atom is σ-bonded and the other is π-bonded, forming complex 1. This complex coordinates the organic azide, forming complex 2. Then the β-carbon of complex 1 attacks the N-3 to form the first covalent C-N bound in intermediate 3 through

nucleophilic addition. The formation of the second covalent C-N bound results in the ring closure, producing the triazoly-copper derivative 4. The final triazole product is formed by protonolysis, accompanying the regeneration of catalytical copper. The click reaction can be employed both, on azide-terminated and alkyne terminated silicon surfaces.

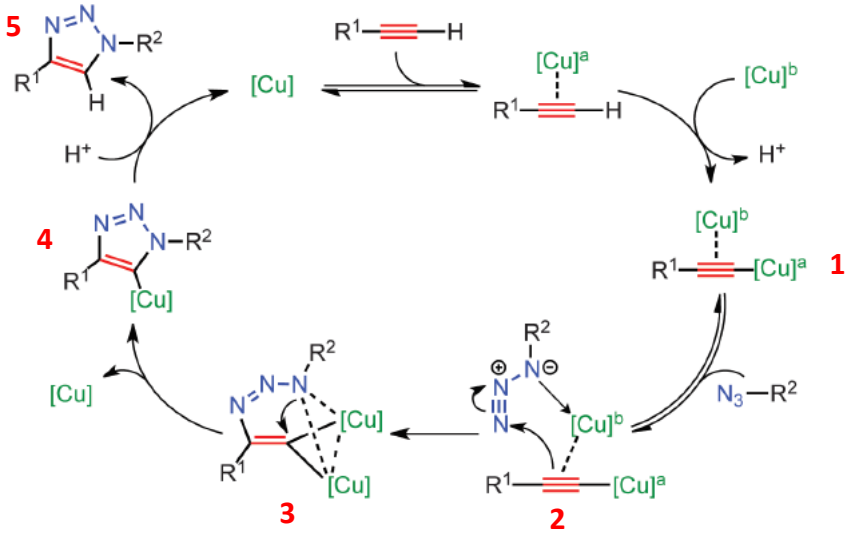

Figure 1.15 Cu(I)-catalyzed azide alkyne cycloaddition (CuAAC) 'click' reaction mechanism [217].

1.3.2.2 Click chemistry on alkyne-terminated non-oxide silicon surfaces

The alkyne-terminated oxide-free silicon surface can be obtained by ethynylation of chlorinated silicon surface [138, 212], thermal hydrosilylation of commercially available distal diynes [170, 218], or photoactivated hydrosilylation of enynes [219] on H-Si surfaces.

The first report on modifying oxide-free silicon surfaces with click chemistry was published by Rohde *et al.* [212] as shown in Figure 1.16. The acetylene group on silicon surfaces was prepared by chlorination of H-Si and subsequent reaction with sodium acetylide. A benzoquinone with an azido group was further successfully immobilized onto the alkyne-terminated silicon surfaces through the CuAAC reaction, which was validated by XPS, FTIR and cyclic voltammetry (CV) results. However, the surface coverage of

the ‘clicked’ monolayer was only 7%, which was due to the extremely high density and rigidity of the acetylene monolayer, making the click reaction only occur at the step edges and defect sites.

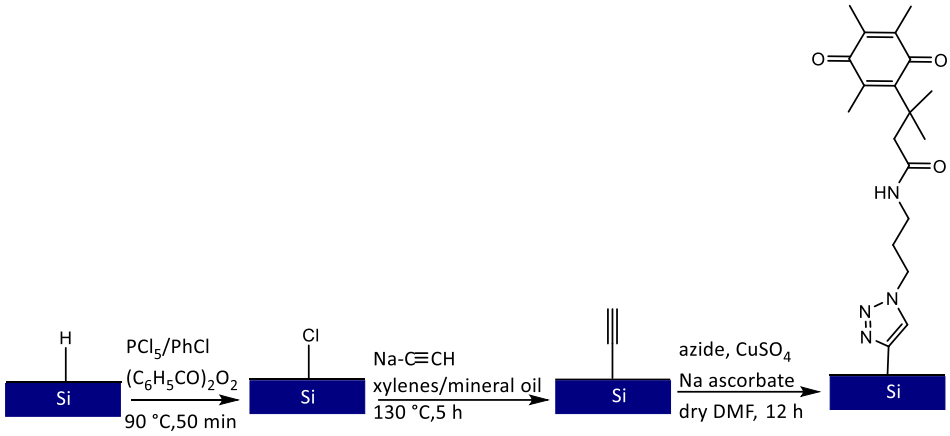

Figure 1.16 Preparation of alkyne-terminated silicon surfaces through a two-step strategy and a further ‘click’ functionalization [212].

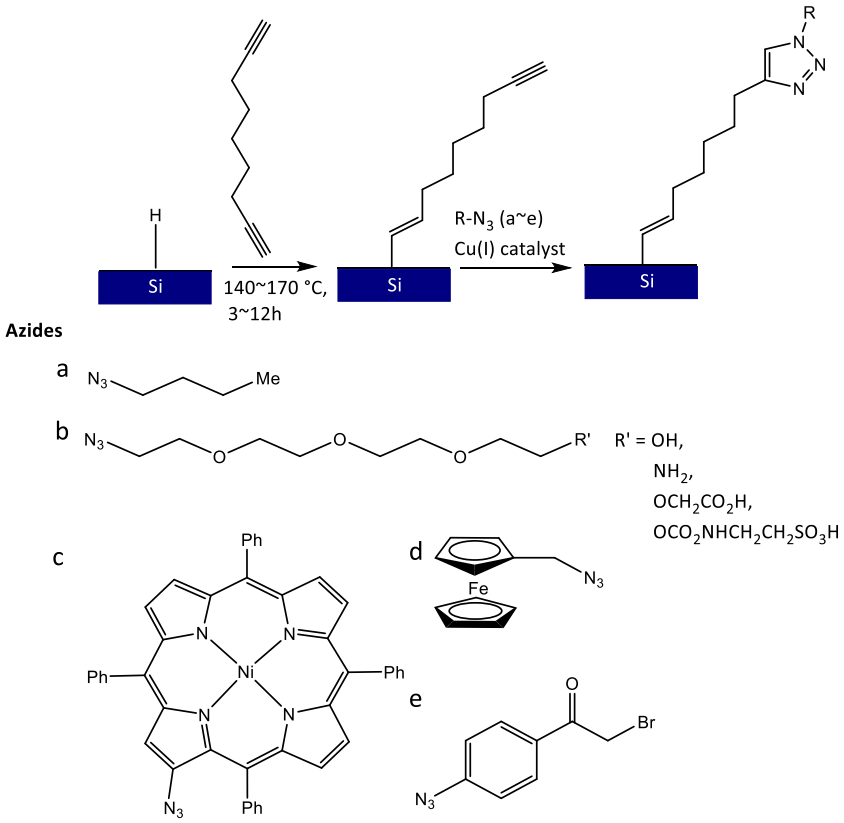

Figure 1.17 A CuAAC ‘click’ reaction on 1,8-nonadiyne modified silicon surfaces [140, 220].

Gooding's group simplified the preparation of alkyne-terminated oxide-free silicon surfaces by direct immobilization of commercially available 1,8-nonadiyne on H-Si, which was further functionalized with various azides in satisfactory yields (> 40%) as outlined in Figure 1.17 [140, 170, 181, 182, 214].

An alternative 'clickable' monolayer was proposed by Qin *et al.* [219] through photoactivated hydrosilylation of α, ω-alkenynes where the alkynyl terminal was protected with a trimethylgermanyl (TMG) group, which can be deprotected in protic solvents in the presence of Ag^+ or Cu^+ to form the acetylene group, allowing for the further functionalization via CuAAC reaction. Importantly, Cu(I) used in the click reaction also induced the deprotection of the TMG group, making the two steps combine in one pot. Figure 1.18 showed the various functional moieties that have been prepared through this strategy.

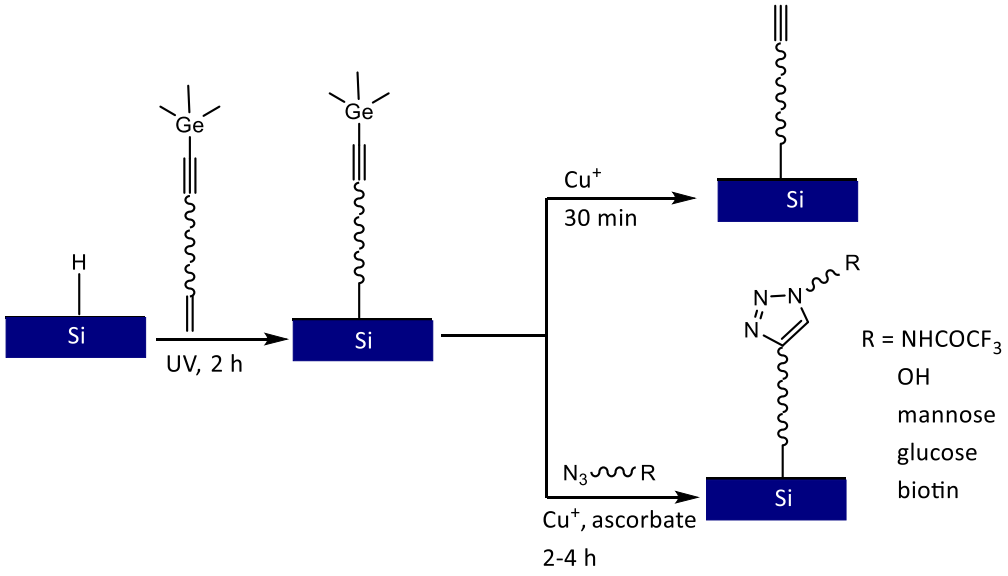

Figure 1.18 Preparation of TMG-terminated film and its deprotection and a further one-pot 'click' functionalization [219].

1.3.2.3 Click chemistry on azide-terminated silicon surfaces

The azide group on the oxide-free silicon surface was commonly prepared by a two-step halogenation/azidation process [213, 221]. For instance, Marrani *et al.* [221] immobilized

11-bro-1-undecene on H-Si by photochemical grafting and then reacted it with NaN_3 to substitute C-Br, forming azide-terminated silicon surfaces, which were further functionalized with ethynylferrocene through a CuAAC reaction as shown in Figure 1.19. The success of the surface modification was verified with XPS measurement and cyclic voltammetry, which showed an efficient charge transfer reaction to the ferrocene redox head group.

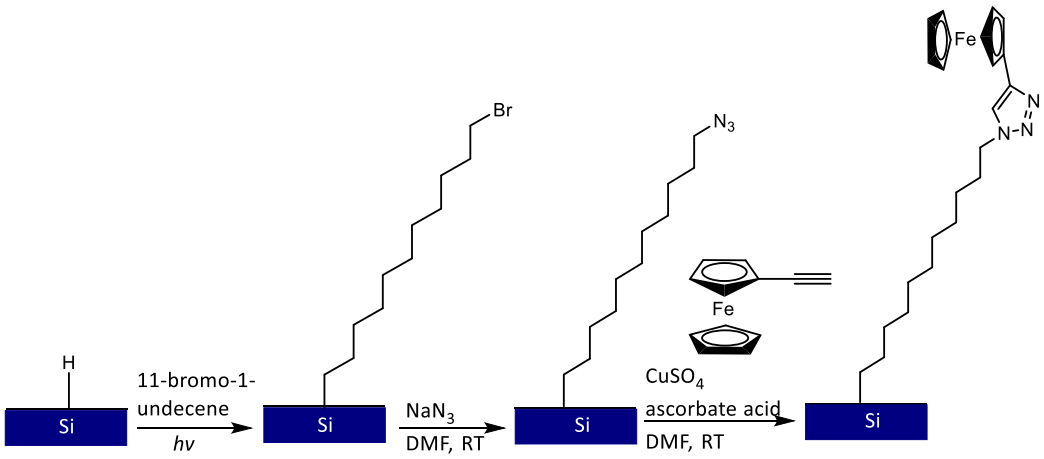

Figure 1.19 A 'click' reaction on azide-terminated silicon surfaces [221].

1.4 Chemical patterning on silicon surfaces

Patterning silicon surfaces is a fundamental method to maintain a high signal-to-noise ratio for many biosensors where the patterned areas act as sensing elements that interact directly with analytes such as biomolecules, viruses, bacteria or cells, while the background of the substrate stays inactive to analyte deposition. Various methods have been used to chemically pattern silicon surfaces. According to the pattern dimension, patterning methods can be classified into micropatterning and nanopatterning methods. Since the best resolution is 0.8 μm so far for LAPS and SPIM [4, 15], which are the focus of this thesis, we will mainly discuss the micropatterning methods, among which the most commonly applied techniques are photolithography and microcontact printing (μCP).

1.4.1 Photolithography

Photolithography has been widely used as a microfabrication technique in the semiconductor industry. A standard procedure for photolithography is shown in Figure 1.20. Generally, a photoresist pattern is obtained by partially exposing a surface covered with a photoresist through a photomask under photoirradiation and then the photoresist of the exposed area for a positive photoresist, or unexposed area for negative photoresist, can be removed through the process of development in a specific developer. Furthermore, the photoresist patterned substrate can be either selectively etched to form physical patterns or chemically functionalized to generate chemical patterns on the substrate.

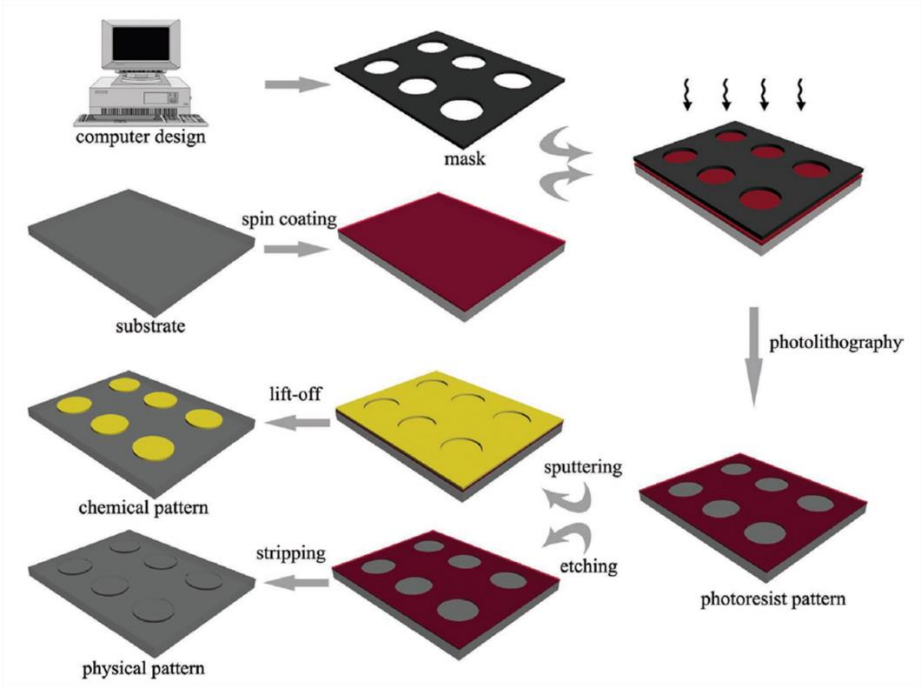

Figure 1.20 Standard procedure for photolithography to create physical and chemical patterns on a substrate [222].

Falconnet *et al.* [223] developed a chemically patterning method using photolithography combined with molecular assembly to obtain a functional micropatterned surface. Recently, Zhu *et al.* [224, 225] reported the chemically patterning of a 1,8-nonadiyne modified porous silicon surface with two different azido species (N_3-OEG-OCH_3 and N_3-OEG-OH) by a combination of photolithography of a photoresist with 'click' chemistry.

The patterned surface was further verified through the conjugation of fluorescein isothiocyanate labelled bovine serum albumin (FITC-BSA) and gelatine, respectively, which were then characterized by a fluorescent microscope and an optical reflectivity measurement. In addition, surface patterning of protein [226], peptides [227], DNA [228] and cells [229] were also achieved by photolithography.

However, the disadvantages of this technique are also obvious, such as the expensive equipment and sophisticated facilities, which limit its widespread use in research labs. Photolithography is not suitable for the patterning on substrates with films that are sensitive to UV-irradiation, photoresists and solvents used for the development of patterns [230]. Recently, Wang *et al.* [133] demonstrated that patterning silicon surfaces modified with SAMs with photolithography not only introduced chemically bonded contaminants, but also decreased the coverage of the monolayers on silicon which was further validated by XPS and LAPS results.

1.4.2 Microcontact printing

Microcontact printing (μCP) as a very powerful alternative micropatterning method has been extensively used to pattern various substances ranging from small molecules [133, 231, 232] and polymers [233, 234] to biomolecules, such as DNAs [235, 236] and proteins [237-239], and even further to cells [240-242]. It was firstly developed by Kumar *et al.* [243] in 1993, who reported the application of a elastomeric stamp made of polydimethylsiloxane (PDMS) with micro-meter features to pattern hexadecanethiol on gold coated silicon surfaces, which served as etching templates for further selective removal of unprotected metal to form microstructured gold electrodes. Figure 1.21 shows the general process of μCP.

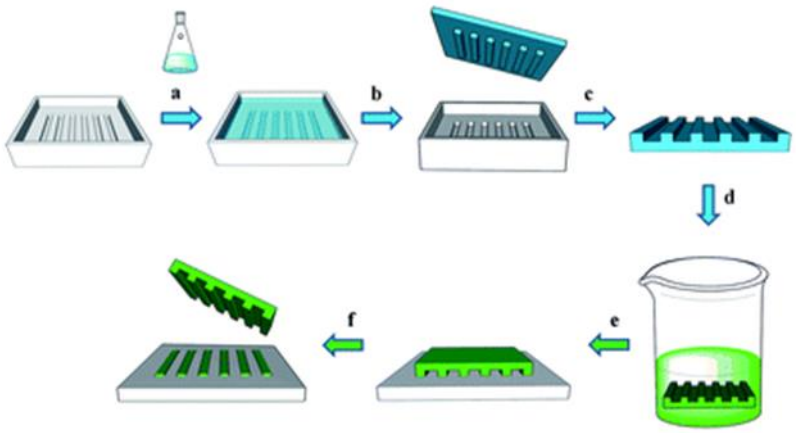

Figure 1.21 General process of μCP [244]. (a) A PDMS precursor is poured into a microstructured master and (b) cured and (c) peeled off; (d) PDMS stamp is immersed into an 'ink' solution; (e) the inked stamp is brought into focal contact with the substrate; (f) the stamp is removed.

Various reactions have been performed successfully via μCP, including the aforementioned 'click' reaction. Nandivada *et al.* [245] first reported the μCP of an azido-biotin onto an alkyne-modified polymer film through a CuAAC 'click' reaction. The obtained biotin patterns were further imaged by the binding of streptavidin. A copper-free 'click' reaction via μCP was demonstrated by Rozkiewicz *et al.* [231] by printing alkynes (1-octadecyne and fluorescent alkyne lissamine rhodamine) onto azido-terminated SAMs on silicon, which was validated by further characterization with AFM, XPS, ellipsometry and fluorescent microscopy (see Figure 1.22). In their later report, acetylene-modified DNAs were also patterned on an azido-terminated glass substrate using a similar method [236]. However, this copper-free method usually suffers from limited reaction conversion [246]. Amines have also been printed onto aldehyde-terminated SAMs via μCP by the same group [247]. Based on this reaction, cytophilic proteins were covalently patterned on aldehyde-modified gold and glass substrates where Hela cells were then incubated and cellular patterns were obtained [238]. In addition, amines have also been printed on anhydride and epoxide modified substrates and thiols have been printed on alkene-terminated substrates [233, 248-250].

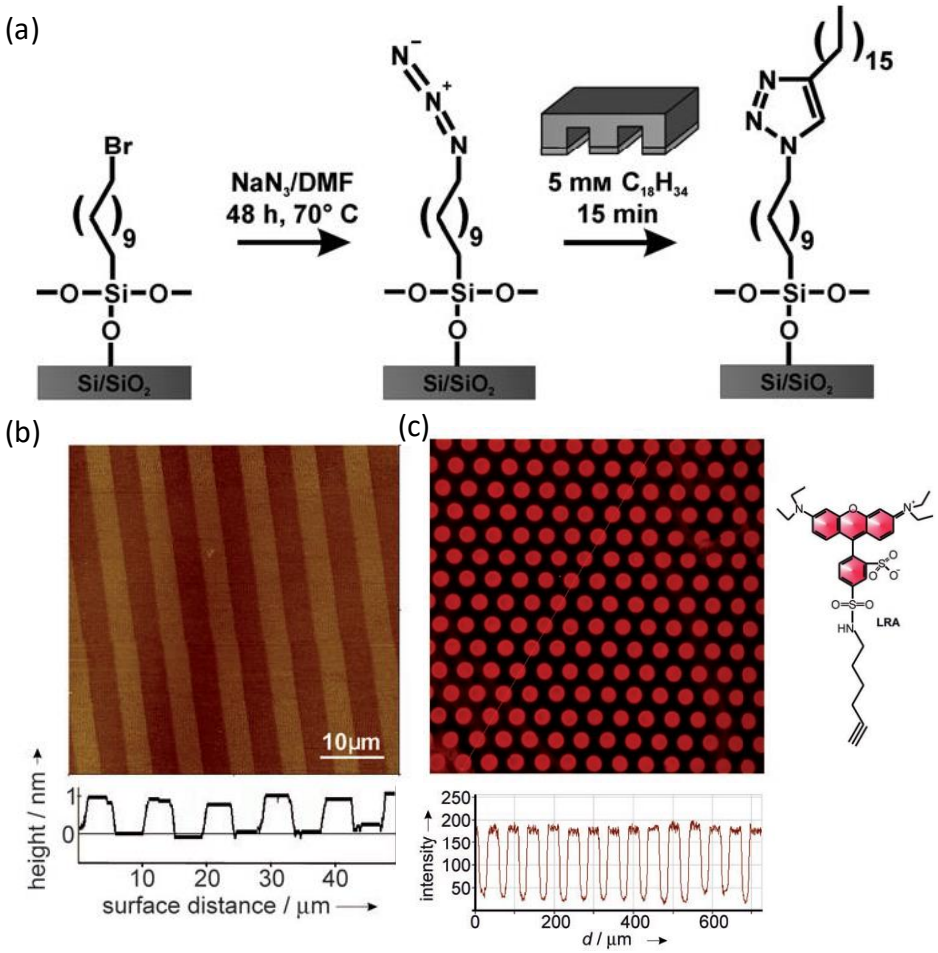

Figure 1.22 (a) Click chemistry via the µCP of 1-octadecyne on azido-terminated SAMs; (b) AFM image of the line patterned 1-octadecyne monolayer; (c) fluorescent image of printed fluorescent alkynes on the azido-terminated surface [231].

1.5 Electrochemical methods for live cell imaging

Live-cell imaging has been used to investigate the structural organization and dynamic processes of living cells or tissues, which can be achieved with optical microscopes and electrochemical imaging methods. The latter one has been more and more attractive in recent years, as they are label-free techniques with resolved spatial resolution, making it possible to investigate cells locally and the heterogeneous cellular activities.

One of the powerful electrochemical method used for cells imaging is scanning electrochemical microscopy (SECM), which is based on the detection of local electrochemical current by scanning a microelectrode or nanoelectrode across the

surface [251-254]. Wang *et al.* [253] reported the application of SECM to image the morphology of human umbilical vein endothelial cells (HUVECs) and detect the morphology change of a single cell after a stimulation to release nitric oxide. Takahashi *et al.* [252] demonstrated the topographic and electrochemical imaging of single cells simultaneously using SECM. However, the scanning probe in the electrolyte may disturb the local environment and the physiological process of the living cells.

Scanning ion conductance microscopy (SICM) is another effective electrochemical technique to image cells. Although it was originally used to map surface topography, it has been developed to image surface charge of single cells by probing the properties of the diffuse double layer at the cellular interface [255-259]. The basic principle of this technique is based on the detection of the ionic current that passes between a quasi-reference counter electrode (QRCE) in an electrolyte solution filled nanopipette and a QRCE in the bulk electrolyte solution when a modulated bias potential is applied between these two QRCEs [260]. Perry *et al.* [259] reported the use of SICM to image the surface charge distribution along with the topography of single Zea mays root hair cells and human adipocytes (see Figure 1.23).

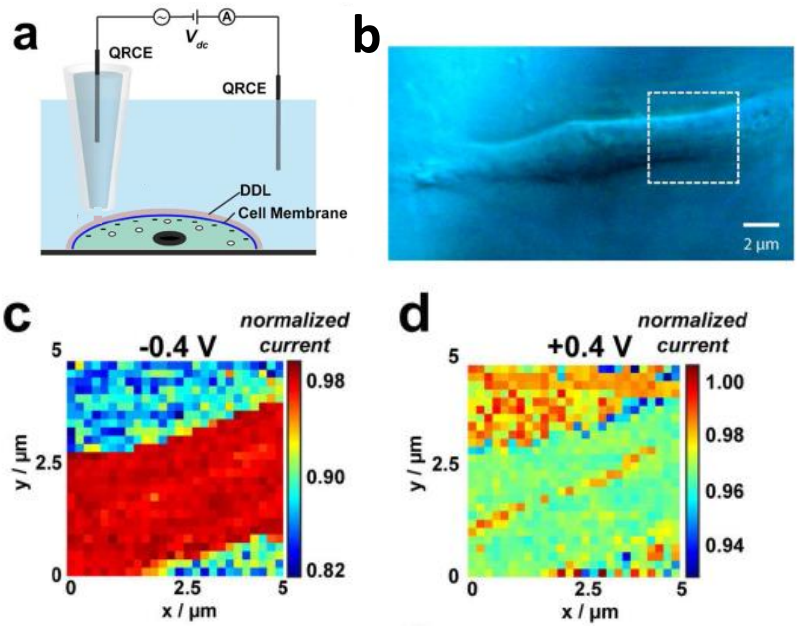

Figure 1.23 (a) Schematic representations of SICM for mapping single cells; (b) Optical microscope image of a human adipocyte cell on a collagen support with the SICM scan region indicated by white dashed lines and corresponding normalized DC ion current images at (c) negative (−0.4 V) and (d) positive (0.4 V) tip biases. The results demonstrated a negative surface charge distribution of the human adipocyte cell.[259]

Plasmonic-based electrochemical impedance microscopy (P-EIM) has been another crucial electrochemical imaging technique as a fast, non-invasive and scanning-free cell-based biosensor, since it was developed by Foley *et al* [261]. The principle of this electrochemical imaging technique is based on the sensitive response of surface plasma resonance to local surface charge densities, which can be detected optically. Figure 1.24 shows the experimental setup of the P-EIM and an EIM image of Hela cells, which matches with the corresponding bright-field and SPR images. Wang *et al.* [262] reported the application of P-EIM to image the impedance of single cells and further monitor the dynamics of individual cellular apoptosis and electroporation with submicrometre spatial resolution and millisecond time resolution. Recently, the P-EIM was employed to investigate the dynamic and transient calcium signalling under agonist stimulation in single Hela cells [263] and the fast initiation and propagation of action potential within

single neurons [264].

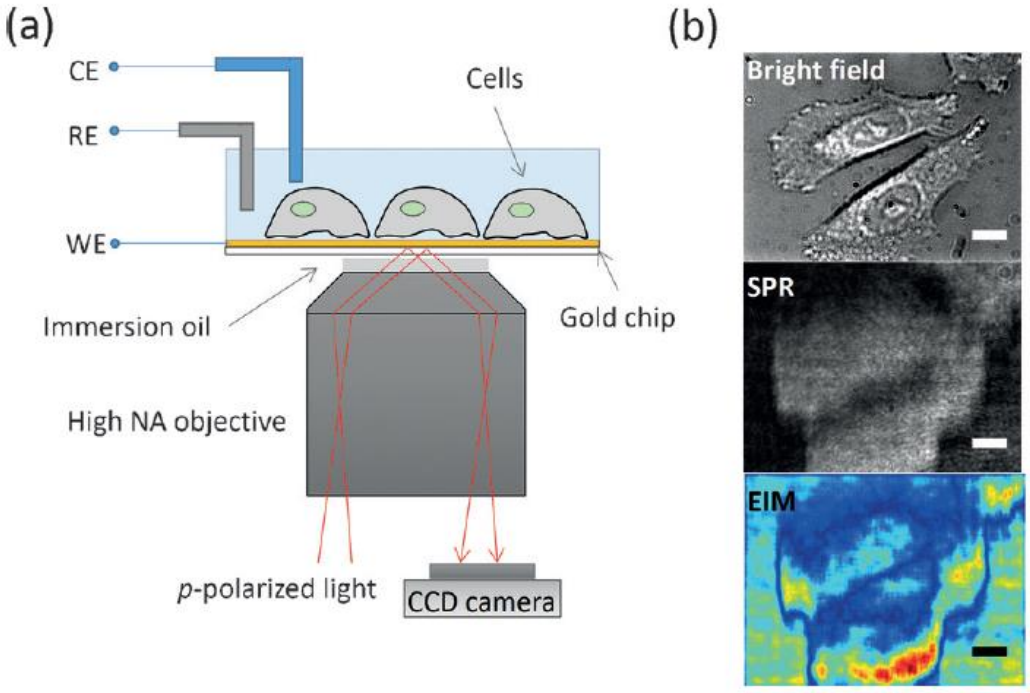

Figure 1.24 (a) Setup of the P-EIM; (b) bright-field, SPR and EIM images of Hela cells [263].

In addition, LAPS have also been applied as an electrochemical imaging method to study the cellular metabolism and cell surface charge and impedance as described in section 1.2, which will be further investigated in chapter 5.

2. Experiments

2.1 Materials

Silicon-on-sapphire (SOS) with a 1 μm thick silicon (100) layer (boron doped, 0.1 Ω·cm) on a 475 μm thick sapphire substrate was purchased from Monocrystal, Russia. Double polished silicon (100) (boron doped, 10-30 Ω·cm, 500 μm thickness) was purchased from Si-MAT, Germany. All chemicals and reagents were purchased from Sigma-Aldrich and used as received without further purification unless otherwise noted. Zero grade argon (BOC online, UK) was dried and purified through an oxygen/moisture trap (Agilent Technologies, USA). 1,8-Nonadiyne was redistilled from sodium borohydride under reduced pressure (95 °C, 25 to 32 Torr), and stored under an argon atmosphere prior to use. Dichloromethane (DCM) was redistilled before use. Ultrapure water (18.2 Ω cm) was collected from a three-stage Millipore Milli-Q 185 water purification system (Millipore, USA) and used to prepare solutions. Table 2.1 shows the chemicals and reagents that have been used in this work.

Table 2.1 Chemicals and reagents

Chemical name	Grade
Hydrogen peroxide	Semiconductor grade, ≥30%
Sulfuric acid	Semiconductor grade, 95-97%
Hydrofluoric acid	Semiconductor grade, 49-51%
Hydrochloric acid	ACS reagent, 37%
1,8-Nonadiyne	98%
Sodium borohydride	99.99%, trace metals basis
Sodium ascorbate	≥98%

Copper(II) sulfate pentahydrate	ACS reagent, ≥ 98.0%
N, *N*, *N*′, *N*′-Tetramethylethylenediamine (TMEDA)	≥99.5%, purified by redistillation
Copper(I) bromide (CuBr)	99.999%, trace metals basis
Tetrakis(acetonitrile) copper(I) hexafluorophosphate ($Cu(CH_3CN)_4](PF_6)$)	97%
Tris[(1-benzyl-1H-1,2,3-triazol-4-yl)methyl]amine (TBTA)	97%
3-Azido-1-propanamine	technical, ≥90% (GC)
4-azidophenyl isothiocyanate (API)	97%
Ethylenediaminetetraacetic acid tetrasodium salt hydrate (EDTA)	98%
Trifluoroacetic acid (TFA)	≥99%
Ethanol (EtOH)	absolute, Puriss., ≥99.8%
Dichloromethane (DCM)	HPLC
Sodium chloride (NaCl)	ACS regent, ≥ 99%
Potassium chloride (KCl)	ACS reagent, ≥99%

2.2 Surface preparation methods

2.2.1 Preparation of an ohmic contact on the SOS substrate

Firstly, the SOS wafer was cut into 0.7 cm × 0.7 cm sized sample using a diamond tipped cutter and the dust on their surface was blown away with nitrogen. Then the sample was rinsed in 10% HF for 30 s and washed with ultrapure water and blown dry with nitrogen.

In order to form the ohmic contact, some 30 nm Cr and 150 nm Au were thermally evaporated onto one corner of the samples using an Edwards Coating System E306A and subsequently heated to 300 °C for 5 min on a hot plate.

2.2.2 Assembly of 1,8-nonadiyne monolayer

The assembly of the 1,8-nonadiyne monolayer followed a procedure reported previously[133, 170]. Firstly, 1,8-nonadiyne was redistilled from sodium borohydride under reduced pressure (95 °C, 25 to 32 Torr), and stored under an argon atmosphere prior to use. Then SOS or silicon substrate was cleaned in a hot piranha solution (3:1 H_2SO_4 (96%)/H_2O_2 (30%), caution: highly corrosive) at 100 °C for 30 min and then rinsed copiously with ultrapure (Milli-Q) water. The cleaned SOS or silicon sample was transferred to a 2.5% HF solution and chemically etched for 90 s to obtain an H-terminated surface (caution: HF is highly corrosive). During the cleaning and etching time, the redistilled 1,8-nonadiyne was transferred into a Schlenk tube and was degassed by freeze-pump-thaw cycles until no gas bubbles evolved from the solution. Then, the freshly prepared H-SOS or H-Si sample was transferred into the degassed 1,8-nonadiyne and left for 3 h at 165 °C under an argon stream. After cooling to room temperature, the functionalized surface (surface 1, Figure 2.1) was then rinsed with copious amounts of redistilled DCM and blown dry with nitrogen.

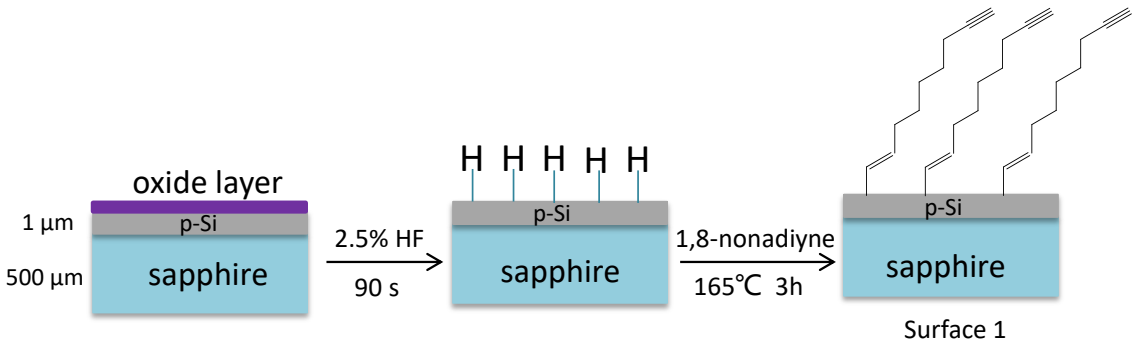

Figure 2.1 Schematic representation of surface modification of SOS or Si substrate with 1,8-nonadiyne.

2.3 Characterization methods

2.3.1 Water contact angle measurement

Contact angle measurement is a technique used to determine the wettability of a solid surface by a liquid, which can be used to indicate the occurrence of a chemical reaction on a monolayer when the terminal functional group changes [265-268]. The contact angle is the angle measured between the liquid-solid interface and the liquid-vapour interface, which can be obtained by firstly capturing the image of a droplet on a solid surface with a camera and then measuring the angle between a tangent line from the three-phase contact point along the droplet and the solid surface [268]. Generally, if the water contact angle of a solid surface is greater than 90°, the surface is considered to be hydrophobic and shows a low affinity to water. When the contact angle of a solid surface is smaller than 90°, the surface is considered to be hydrophilic and shows a higher affinity to water (Figure 2.2).

In this work, the water contact angle measurements were performed using a Drop Shape Analysis System (Krüss DSA100, Germany). 1 μL of ultrapure water was carefully deposited onto sample surface, and three spots were measured on each sample and averaged.

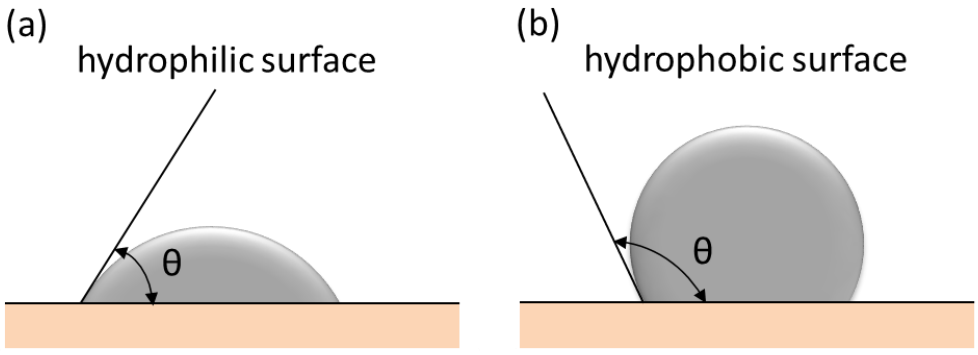

Figure 2.2 Schematic representation of (a) hydrophilic surface and (b) hydrophobic surface.

2.3.2 Ellipsometry

Ellipsometry is a non-destructive and sensitive method widely used to detect the thickness and optical properties of thin films [154, 269]. Generally, this technique measures the change in the polarization state of the light beam. As illustrated in Figure 2.3, linearly polarized incident light was changed to elliptically polarized light after it was reflected by the sample surface. This polarization change can be characterized by the ellipsometric parameters Ψ and Δ with the following equation:

$$\rho = \tan(\Psi) \cdot e^{i\Delta} = \frac{r_p}{r_s}$$

where r_p and r_s are the reflectivity of the light polarized parallel and perpendicular to the plane of incidence, respectively, which are the functions of the refractive index of the material; ρ is the ratio of these two reflectivities and is a complex number; $\tan(\Psi)$ is the amplitude of the reflectivity ratio and Δ is the phase shift. An ellipsometer can directly measure the values of Ψ and Δ as functions of wavelength. In order to acquire the optical properties and the thickness of the films, optical models need to be built to fit the data.

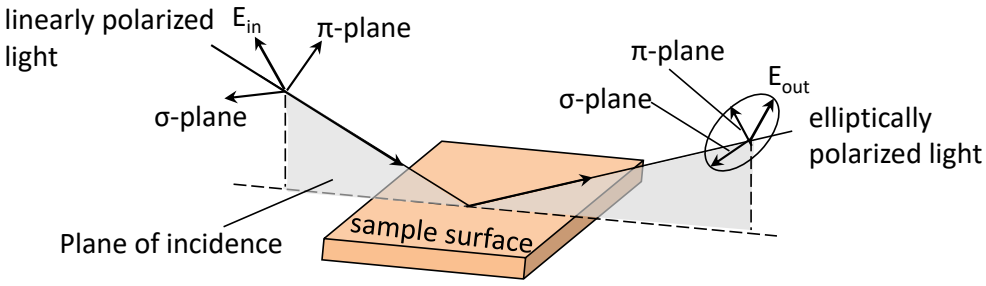

Figure 2.3 The principle of ellipsomotry [270].

In our work, an alpha-SE® Spectroscopic Ellipsometer (J.A. Woollam Co. Inc., USA) and CompleteEASE software (J.A. Woollam Co. Inc., USA) for data collection and analysis were used to measure the thickness of monolayers on silicon surfaces. A He-Ne laser (632.8 nm) and an angle of incidence of 70˚ were adopted. The optical constants (refractive index (n) and imaginary refractive index (k)) of the substrate were determined

from a freshly etched H-Si (n = 3.877, k = 0.051). The model used to determine the monolayer thickness was built as a single layer absorbed on the H-Si substrate using the Cauchy model in the software. The refractive index of the organic monolayer was set to 1.46 in this work [167]. At least three measurements were taken at different spots on each sample and averaged.

2.3.3 X-ray photoelectron spectroscopy (XPS)

X-ray photoelectron spectroscopy (XPS), also known as electron spectroscopy for chemical analysis (ESCA), has been widely used to characterize the chemical composition and chemical states of sample surfaces [271-274]. It measures the kinetic energy of photoelectrons (E_p) that escape from sample surfaces following the excitation by the mono-energetic X-rays as depicted in Figure 2.4 [275, 276]. Since the energy of the X-rays (hv) is known, the binding energy (E_b) can be obtained from the following equation:

$$E_b = hv - E_p - \varphi$$

Where φ is the work function (energy required to remove electrons from Fermi level to vacuum level) of the analyzer. According to the peak position of the binding energy, the elemental species and chemical states can be recognized. The intensity of the binding energy indicates the ratio of the different elements and chemical bonds.

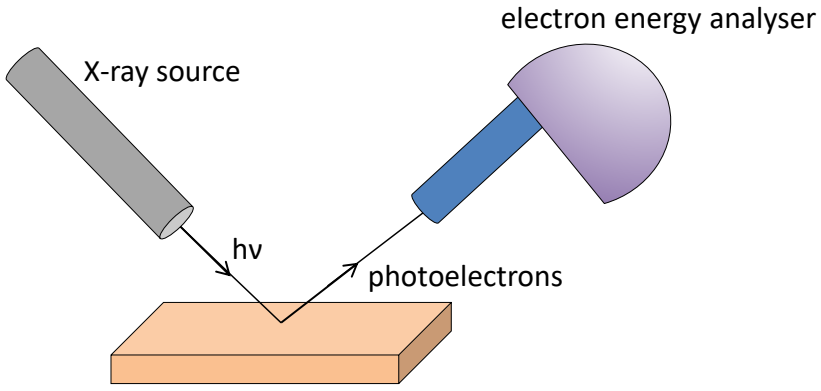

Figure 2.4 Principle of XPS.

In our work, XPS experiments were performed on modified SOS surfaces at the nanoLAB of Newcastle University, UK, using a Kratos Axis Nova spectrometer with CasaXPS software. Samples used for XPS measurements were all with homogenous surface modification prepared either by immersing the whole sample in the reaction solution or with flat, featureless PDMS stamps. Survey scans were carried out over a 1100-0 eV range with a 1.0 eV step size, a 100 ms dwell time, and an analyser pass energy of 100 eV. High-resolution scans were run with a 0.1 eV step size, a dwell time of 100 ms, and the analyser pass energy set to 20 eV. The scan regions were Si 2p (97-107 eV), C 1s (278-294 eV), N 1s (392-408 eV), O 1s (526-542 eV) and Cu $2p_{3/2}$ (926-938 eV).

2.3.4 Electrochemical impedance spectroscopy (EIS)

The electrochemical impedance spectroscopy (EIS), also known as AC impedance or just impedance spectroscopy, has been used to characterize electrodes and interface processes[277, 278]. Generally, it measures an output alternating current (AC) flowing through an electrochemical cell after the application of an AC voltage to the electrochemical cell. The AC signal is applied over a range of frequencies. The impedance in an EIS measurement is usually determined by the following equation:

$$\mathrm{Z}(\omega) = \frac{V_0 \sin(\omega t)}{I_0 \sin(\omega t + \varphi)} = Z_0 \frac{\sin(\omega t)}{\sin(\omega t + \varphi)} = Z' + jZ''$$

Where V_0 and I_0 is the amplitude of the applied AC voltage and output AC current, respectively, $\omega = 2\pi f$ is the radial frequency of the AC voltage (f is the frequency expressed in Hz), φ is the phase shift between the input AC voltage and the output AC current, and Z_0 is the amplitude of the impedance. The EIS results are usually displayed in the forms of Bode plots and Nyquist plots. The Bode plots illustrate the impedance and phase shift as the functions of frequency, which are associated with the resistive and capacitive properties of an electrochemical system. In general, impedance measured at very low phase shift near 0° is related to resistances, while impedance measured at very high phase shift around 90° is associated with capacitance. The Nyquist plot displays the

imaginary impedance component (Z'') against the real impedance component (Z'). Each point on the Nyquist plot is the impedance measured at one frequency. Its main drawback is that it is difficult to tell what frequency is used to record that data point.

In this work, all the EIS measurements were performed performed in a 10 mM phosphate buffer solution at pH 7.4 containing 137 mM NaCl and 2.7 mM KCl, using an Autolab PGSTAT30/FRA2 (Windsor Scientific Ltd., UK) with a three-electrode system including a platinum electrode as the counter electrode, an Ag/AgCl electrode as reference electrode.

2.3.5 Nuclear Magnetic Resonance Spectroscopy

Nuclear magnetic resonance spectroscopy (NMR) is a research technique based on the phenomenon of nuclear magnetic resonance to measure the structure, dynamics, reaction rate and chemical environment of molecules. The resonance frequency can be changed by the intramolecular magnetic field around an atom in a molecule, thus allowing the detection of the detailed information of the electronic structure of a molecule and the functional groups. In this work, ^{13}C NMR spectra were recorded using a Bruker Avance 400 MHz spectrometer employing DMSO-d_6 as the solvent. Chemical shifts were referenced to the residual carbon peak of DMSO-d_6 at 39.5 ppm.

2.3.6 Electrospray ionization mass spectrometry (ESI-MS)

Mass spectrometry (MS) is an analytical technique extensively used to measure the molecular weight of chemical species by ionizing them and then sorting the ions based on their mass-to-charge ratio. Electrospray ionization (ESI) is a soft ionization method which produces ions by applying a high voltage to a liquid in an electrospray to generate gas phase ions. The advantage of the ESI-MS is that it creates very little fragmentation and can always observe the molecular ions. In this work, Agilent LC-MS, comprising a 1100 Series LC and SL Ion Trap MSD was used for the ESI-MS measurement.

2.4 LAPS and SPIM setup

LAPS/SPIM measurements were carried out in an electrolyte solution. Samples were fixed on a custom built cell as depicted in Figure 2.5. An O-ring with an inner diameter of 1 mm or 3 mm determined the area of the measurement. An Ag/AgCl electrode was used as a reference electrode (RE), a platinum electrode as a counter electrode (CE) and a metal contact on the semiconductor substrate as the working electrode (WE). A laser illuminated the backside of the semiconductor.

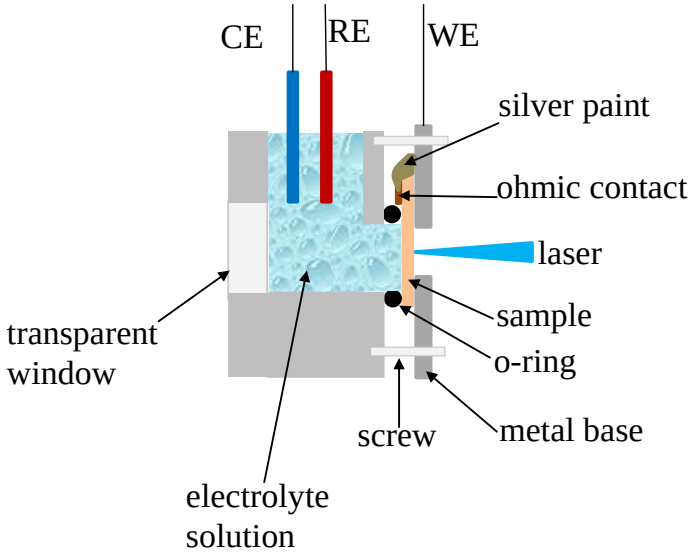

Figure 2.5 Schematic representation of the sample holder for photocurrent measurements.

The whole LAPS and SPIM measurement setup is shown in Figure 2.6. A laser diode module LD1539 (Laser 2000, λ=405 nm, max. 50 mW) and a femtosecond Cr-Forsterite laser (DEL MAR PHOTONICS, λ=1250 nm, 80 fs pulses, 200 mW, 80 MHz) were used. The modulation frequency was 1 kHz for all LAPS/SPIM measurements on SOS substrates. The beam profile of the laser diode module was improved by using a spatial filter and a collimator lens. The infrared laser was modulated by a chopper and was passed through a beam expander. All lasers were focused onto the semiconductor substrate using an LD Plan-NEOFLUAR 40× objective with a correction ring (Zeiss, numerical aperture 0.6), which allowed to correct for spherical aberration caused by focusing through a solid

substrate. The sample holder (shown in Figure 2.5) was mounted onto an M-VP-25XL XYZ positioning system with a 50 nm motion sensitivity on all axes (Newport, UK). A white light illuminated the sensor from the front side to obtain an optical image of the sensor surface from the CMOS camera. The photocurrent was measured using an EG&G 7260 lock-in amplifier. The control program used for the measurements was written in LabView by Dr Shihong Jiang [15].

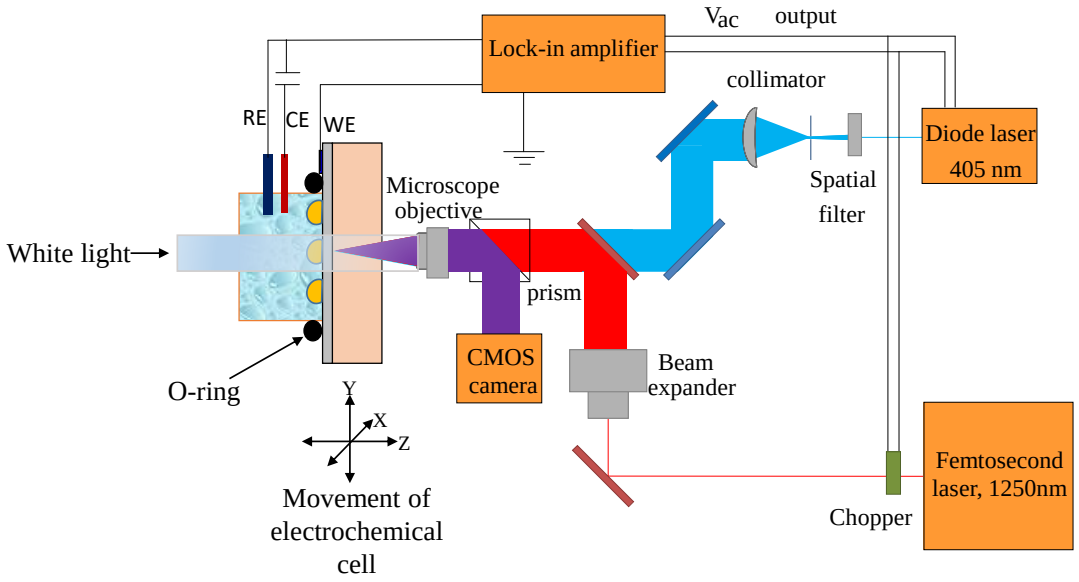

Figure 2.6 Experimental setup for LAPS/SPIM measurements.

3. Copper contamination of self-assembled organic monolayer modified silicon surfaces following a 'click' reaction characterized with LAPS and SPIM

3.1 Introduction

'Click' chemistry, especially the Cu(I)-catalyzed azide alkyne cycloaddition (CuAAC) reaction, has been used extensively to modify silicon surfaces [146, 147, 175, 212, 214, 215], due to its many advantages, such as high selectivity and yield, mild reaction conditions and good compatibility with various solvents, since it was first described by Sharpless' group in 2001 [216]. However, few investigations have been made on the copper residue that remains on silicon surfaces after 'click' reactions despite its potentially detrimental effect on biological systems and contamination issues in other applications [279, 280]. X-ray photoelectron spectroscopy (XPS) is one of the most widely used methods to characterize copper ions on silicon surfaces. Gooding's group showed that a Cu 2p3/2 emission at ~933 eV was present in the XPS spectra when there was a trace of residual copper following a 'click' reaction on alkyne-terminated silicon surfaces [170]. However, following rinsing of the modified samples with dilute aqueous hydrochloric acid (HCl) solution, copper could no longer be detected by XPS [182, 183, 224, 225, 281].

Patterning silicon surfaces is a fundamental method to maintain a high signal-to-noise ratio for many biosensors where the patterned areas act as sensing elements that interact directly with analytes such as biomolecules, viruses, bacteria or cells, while the background of the substrate stays inactive to analyte deposition. The two most widely used methods for chemically patterning silicon surfaces modified with self-assembled organic monolayers are photolithography [224, 225, 282] and microcontact printing (μCP) [232-236, 283]. We have recently reported that photolithography not only introduces chemically bonded contaminants, but also decreases the coverage of the monolayers on

silicon [133]. Meanwhile, our group has also demonstrated that the strategy of combining μCP with 'click' chemistry on alkyne terminated surfaces is non-destructive and efficient.

Light-addressable potentiometric sensors (LAPS) and scanning photo-induced impedance microscopy (SPIM) have been reported to be highly sensitive to the surface contamination on self-assembled organic monolayers [133]. In this chapter, LAPS and SPIM were used to study the copper(I) residue that remains on alkyne-terminated silicon surfaces following 'click' reactions, as well as the electrochemical properties of the functionalized organic monolayers. Firstly, the silicon on sapphire (SOS) sensor substrates were modified with 1,8-nonadiyne self-assembled organic monolayers, serving as the insulator for LAPS and SPIM with high sensitivity [133]. The subsequent CuAAC 'click' reaction combined with μCP created a pattern with both 'clicked' areas and unreacted alkyne-terminated areas to allow 2D imaging of the electrical properties (surface charge and impedance) of 'click' modified surfaces with LAPS and SPIM.

3.2 Experimental methods

3.2.1 Materials.

SOS with a 1 μm-thick silicon (100) layer (boron doped, 0.1 Ω·cm) on a 475 μm-thick sapphire substrate was purchased from Monocrystal, Russia. Double-polished silicon (100) (boron doped, 10−30 Ω·cm, 500 μm thickness) was purchased from Si-MAT, Germany. All chemicals and reagents were purchased from Sigma-Aldrich, unless otherwise noted. The following reagents were used as received: hydrogen peroxide solution (30 wt % in H_2O_2, semiconductor grade), sulfuric acid (95.0−98.0%, semiconductor grade), hydrochloride acid (ACS reagent grade), tetrasodium salt hydrate of ethylenediaminetetraacetic acid (EDTA, 98%), ethanol (100%), sodium ascorbate (98%), copper(II) sulfate pentahydrate (99%), *N,N,N′,N′*-tetramethylethylenediamine (TMEDA, ≥99.5%), copper(I) bromide, tetrakis(acetonitrile) copper(I) hexafluorophosphate [$Cu(CH_3CN)_4](PF_6)$, 97%], tris[(1 benzyl-1H-1,2,3-triazol-4-yl)-

methyl]amine (TBTA, 97%), 3-azido-1-propanamine [azido-NH_2, technical, ≥90% (GC)], and dimethyl sulfoxide (DMSO, ≥99.5%). Dichloromethane (DCM) was redistilled before use for cleaning. 1,8-Nonadiyne (98%) was redistilled from sodium borohydride (99.99%) and stored under argon. A Sylgard 184 poly(dimethyl siloxane) (PDMS) kit was purchased from Dow Corning. For photocurrent measurements and cyclic voltammetry, 10 mM phosphate buffer solution at pH 7.4 containing 137 mM NaCl and 2.7 mM KCl was used. All solutions were prepared with ultrapure water (18.2 Ω·cm) from a three-stage Milli-Q 185 water purification system (Millipore, USA). Argon was dried and purified through an oxygen/moisture trap (Agilent Technologies, USA).

3.2.2 Preparation of silicon master and PDMS stamp

The master and PDMS stamps were prepared following a previously reported protocol [4, 232, 250]. Briefly, a silicon master with patterns was prepared by UV photolithography. In this work, the master was provided by Dr Julien Gautrot's group. The PDMS stamps were fabricated by curing a mixture of PDMS resin and curing agent (184 silicone elastomer, Sylgard 184) in a ratio of 10:1 (w/w) on the surface of the master at 60 °C for 12 h. Subsequently, the cured PDMS was peeled off from the master. The patterns of the PDMS stamp consisted of circular islands with (i) a diameter of 100 μm and 40 μm gaps, and (ii) a diameter of 40 μm and 30 μm gaps.

3.2.3 Cleaning of the PDMS stamp

The cured PDMS stamp was cleaned with a soxhlet extractor prior to use as reported previously to remove the uncross-linked fragments or other contaminants which can contaminate the silicon substrate during the microcontact printing process [284]. The soxhlet extractor was commonly used to extract lipid from a solid material. In our experiment, the extractor was connected with a round bottomed flask and a condenser as shown in Figure 3.1. Absolute ethanol was used as the solvent to remove the contaminants in the PDMS stamp. When the solvent was heated, its vapour went up to the condenser

from where it flowed down to the extractor chamber where the PDMS stamp was placed. Once the chamber has filled with the warm solvent, it would be emptied by siphon action and all of the solvent would flow back into the flask. The cycle was repeated overnight many times to make sure all the contaminants were washed away. After the extraction, the PDMS stamp was weighed dry prior to use.

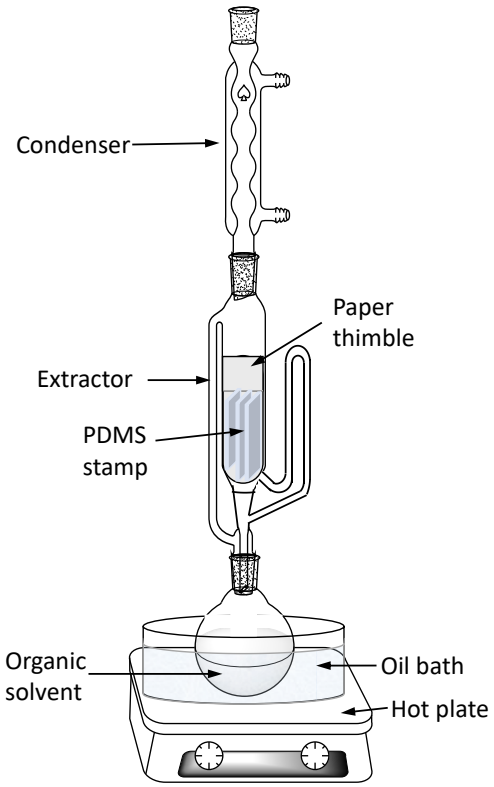

Figure 3.1 Schematic representation of cleaning the PDMS stamp with a soxhlet extractor.

3.2.4 Patterning of SOS surfaces with microcontact printing combined with 'click' chemistry

First, SOS surfaces were modified with 1,8-nonadiyne as described in section 2.2 before the patterning process. Figure 3.2 illustrates the process of 'click' chemistry on surface 1 using μCP. The PDMS stamps were firstly treated in an oxygen plasma (pressure: 0.8 Torr, generator: 40 kHz/100 W) for 30 s to make the stamp surfaces hydrophilic. Then, they were immersed in the 'click' solutions for 30 min. Herein, three alternative 'click' solutions, displayed as solution A, B and C, were employed, consisting of (A) the azido-

NH_2 (10 mM, ethanol/water 2:1), copper(II) sulfate pentahydrate (1.1 mol% relative to the azide), sodium ascorbate (10 mol% relative to the azide) and TMEDA (0.45 mM), (B) the azido-NH_2 (10 mM, DMSO), CuBr (10 mol% relative to the azide) and TMEDA (20 mol % relative to the azide), (C) the azido-NH_2 (10 mM, DMSO), tetrakis(acetonitrile) copper(I) hexafluorophosphate $[Cu(CH_3CN)_4](PF_6)$ (10 mol% relative to the azide) and tris[(1-benzyl-1H-1,2,3-triazol-4-yl)methyl] (TBTA) (10 mol% relative to the azide), respectively. The soaked stamps were dried under nitrogen gas and placed onto the alkyne-terminated surface for 3 h at room temperature. The reactions were carried out in a sealed Petri dish in the presence of a moistened tissue. After removing the stamps, the unreacted reagents were removed by rinsing the substrate consecutively with copious amounts of DMSO, ethanol, water. The resultant corresponding 'click' modified surfaces are referred to as surfaces 2a, 2b and 2c. Then the samples were rinsed in either a 0.5 M hydrochloric acid solution for 2 min, or EDTA (0.05% w/v, pH 7.4) for 24 h to remove the copper residue and rinsed with copious amounts of water. To characterize the 'clicked' surface properly, chemically homogeneous surfaces (surface 2a*, 2b*, and 2c*) were also prepared using a flat featureless PDMS stamp following the same procedure. As control experiments, inks ('click' solutions A, B and C) without azide were printed on surface 1 using the same procedure in Figure 3.2, indicated as control surfaces *a*, *b* and *c*.

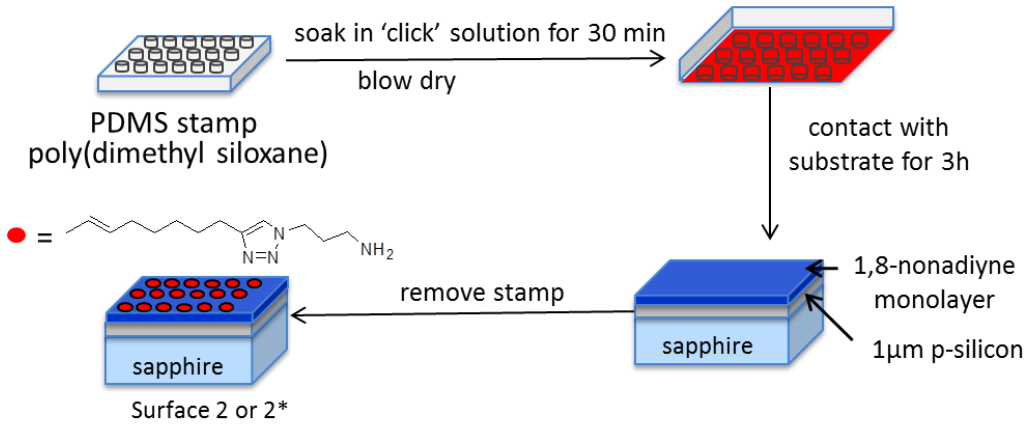

Figure 3.2 Schematic illustration of the µCP of 'click' chemistry: azido-NH_2 was printed on 1,8-nonadiyne modified surface 1 and 'click' reactions occurred exclusively in the

contact area (surface 2: an array of chemical pattern, surface 2: a homogeneous surface functionalized with azido-NH_2 by a flat featureless PDMS stamp). For ellipsometry measurements, the above surface modification was carried out on silicon substrates.*

3.2.5 Surface characterization

The water contact angle, ellipsometry and XPS measurements were carried out to characterize the surface modifications as described in section 2.3.

Cyclic voltammetry was performed in a 10 mM PBS solution (pH=7.4) described above using an Autolab PGSTAT30/FRA2 (Windsor Scientific Ltd., UK) with a three-electrode system including a platinum electrode as the counter electrode, an Ag/AgCl electrode as reference electrode, and a modified SOS substrate as the working electrode. The scan rate was 50 mV/s.

3.2.6 LAPS and SPIM measurement

The LAPS/SPIM setup has been shown in section 2.4. In this work, the sensor chips used for LAPS measurements were all based on SOS substrates. LAPS measurements were carried out using the focused and electronically modulated diode laser LD1539 (Laser 2000, λ= 405 nm, max. 50 mW, focused spot diameter ~1 µm). The modulation frequency was 1 kHz.

3.3 Results and discussion

3.3.1 Characterization of 1,8-nonadiyne monolayer and 'click' functionalization by µCP

1,8-Nonadiyne monolayers were characterized by water contact angle, ellipsometry and XPS. As shown in Table 3.1, a water contact angle of 86˚ which indicated a hydrophobic monolayer, and an ellipsometric thickness of 9.2 Å for an alkyne-terminated surface are

comparable to literature results [133, 181, 182]. XPS spectra of the modified SOS surface (Figure 3.3a) showed the presence of Si, C, and O, which is in good agreement with results published previously [170, 181, 214]. The high-resolution narrow scans of XPS provide information on surface bonding. The C 1s narrow scan included a main C-C peak (~285 eV), and two small peaks from Si-C=C (~284 eV) and C-O (286.5 eV) (Figure 3.3b). The binding energies observed were consistent with the results reported elsewhere [170, 181]. The alkyne-terminated organic monolayers on silicon surfaces provide a platform for further functionalization via CuAAC 'click' chemistry.

Table 3.1 Contact angles and ellipsometry thicknesses of different surfaces

Surface	'Click' catalyst	Water contact angle (°)	Ellipsometry thickness (Å)
1 SOS-nonadiyne	—	86±1	9.2±0.3
2a* SOS-NH_2	$CuSO_4$/sodium ascorbate	56±2	14.9±0.5
2b* SOS-NH_2	CuBr	55±2	14.3±0.6
2c* SOS-NH_2	$[Cu(CH_3CN)_4](PF_6)$	56±3	15.2±0.4

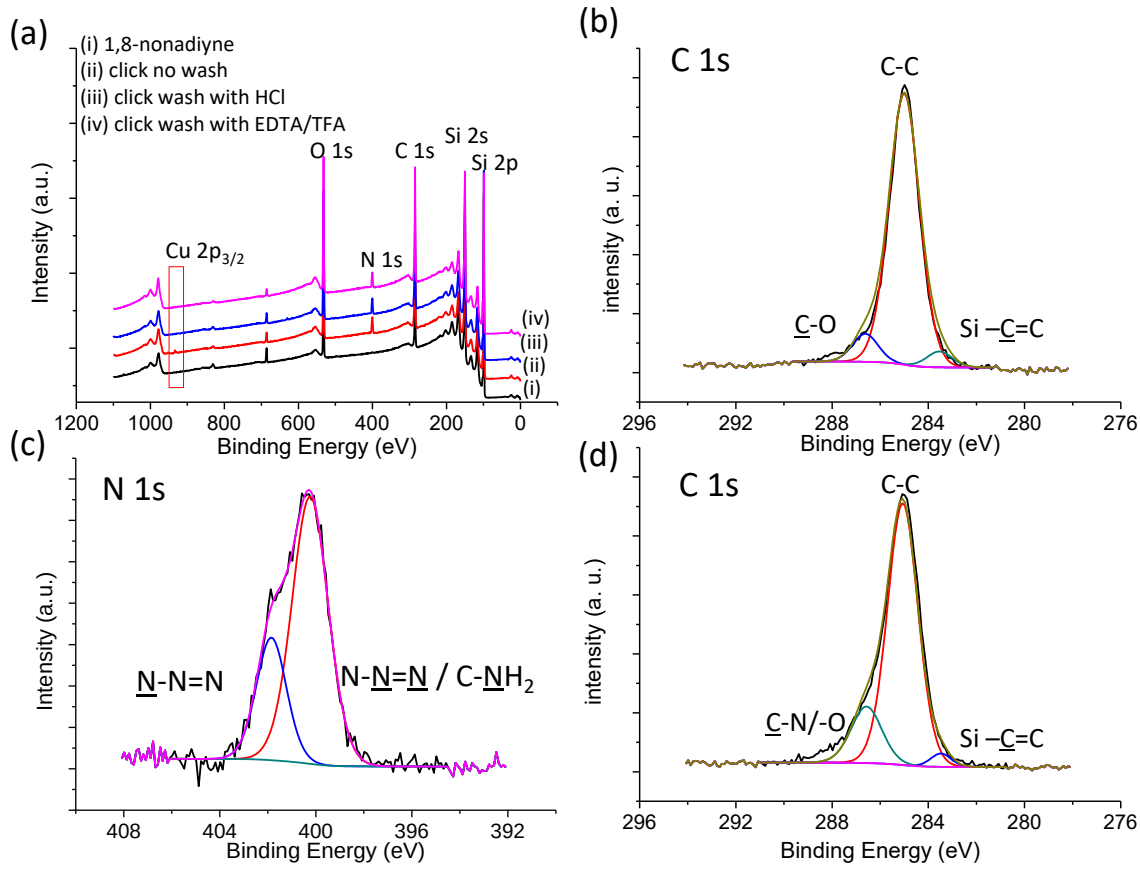

Figure 3.3 (a) XPS spectrum of samples modified with 1,8-nonadiyne (i), and 3-azido-1-propanamine without any further cleaning to remove the copper residue (ii), with further cleaning with 0.5 M HCl for 2 min (iii),and with further cleaning with 0.05% EDTA/TFA for 24 hours (iv). Narrow scans of (b) C 1s of surface 1, (c) N 1s and (d) C 1s of surface 2a.*

For 'click' conditions A, the water contact angle of the 'clicked' surface (surface 2a*) decreased to 56˚ (Table 3.1) due to the amino moieties, which is in agreement with previously reported values [182]. The ellipsometric result shows that after the 'click' reaction, the thickness of the monolayer increased to ~14.9 Å, which is comparable to the thickness of 15.3 Å determined from X-ray reflectivity (XRR) analysis [182]. The successful 'click' reaction was also demonstrated by XPS results. The presence of an N 1s peak at ~401 eV in the XPS survey spectrum (Figure 3.3a) indicated the formation of a triazole. The narrow scan signal of the N 1s region (Figure 3.3c) was deconvoluted and fitted to two peaks at 400.2 eV and 401.8 eV, which were assigned to C-$\underline{N}H_2$/N-$\underline{N}$=$\underline{N}$,

and N-N=N, respectively. The ratio of the peaks areas is about 2.6:1, which is slightly smaller than the stoichiometric ratio of 3:1, but is consistent with literature results [182, 183]. The absence of a peak at 403 eV, which corresponds to the central electron-deficient nitrogen in the azido groups, showed that there was no physisorption of azide on the silicon surface. The narrow scan from the C 1s region (Figure 3.3d) was deconvoluted into three peaks assigned to Si-C=C (284.2 eV), C−C (285.3 eV) and C−N/−O (286.8 eV) [182, 183]. An increased ratio of C−N/−O to Si-C=C was due to the successfully bonded amino group on silicon surfaces. After 'click' modification, a copper peak at ~933 eV was only visible when the sample was not rinsed with either HCl or EDTA solutions (Figure 3.3a). The narrow scan of Cu 2p3/2 could be fitted to only one peak at 933.2 eV (Figure 3.4) which is consistent with copper(I) [170]. No copper peak was visible after rinsing with either reagent. Two alternative strategies for 'click' modification were verified with water contact angle and ellipsometry results (Table 3.1, entries 2b and 2c).

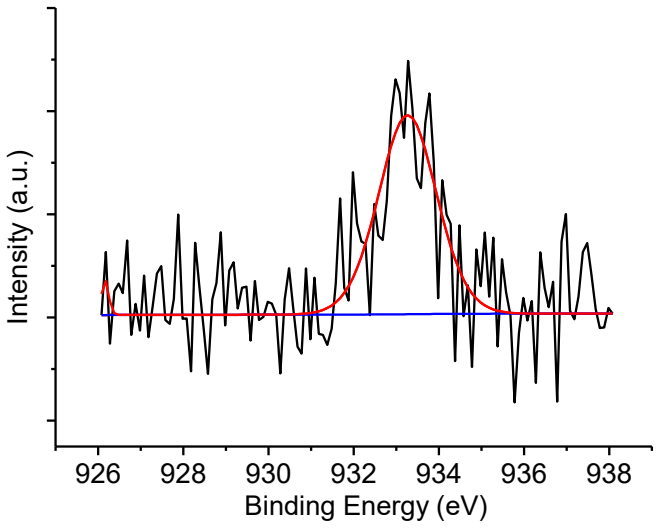

Figure 3.4 Narrow scan of Cu 2p3/2 of surface 2a.*

3.3.2 The effect of the PDMS stamps for μCP on LAPS and SPIM images

LAPS and SPIM have been validated to be very sensitive techniques to detect the properties of surface electrical potential and impedance, respectively, with spatial

resolution. To ensure that no artefacts were introduced by the μCP, control experiments with uncleaned and cleaned blank PDMS stamps on a 1,8-nonadiyne modified SOS sample were carried out. Figure 3.5a showed the SPIM image on a control sample with an uncleaned PDMS stamp at a bias voltage of 0.8 V, which is identical to the pattern on the PDMS stamp used. The time for one scan was about 15 min (area 400 μm x 400 μm, step size 4 μm). There was an increase of the maximum photocurrent which corresponded to a lower impedance on the contact area compared to the rest 1,8-nonadiyne modified surface. Figure 3.5c showed a positive shift of +16 ± 2 mV of the *I-V* curves on the contact area compared to the rest 1,8-nonadiyne modified surface corresponding to a more negatively charged surface on the contact area than the rest 1,8-nonadiyne modified surface. These SPIM and LAPS results indicated that the uncleaned PDMS stamp introduced contaminants or damaged the monolayer, which could be explained by the following two assumptions. One is that the uncross-linked fragments in the uncleaned PDMS stamp acted as a glue which peeled off parts of the insulating 1,8-nonadiyne monolayer in the contact circular area and then decreased the impedance. The resultant oxidation of the contact area rendered it more negatively charged than the intact 1,8-nonadiyne modified area. The other assumption is that there was some platinum catalyst, which was used to catalyse the crosslinking reaction to form the PDMS stamp, left in the contact area, which decreased the impedance of the monolayer. The platinum catalyst was in the form of $PtCl_4^{2-}$ which caused the positive shift of the *I-V* curves on contact area compared to the 1,8-nonadiyne modified area. While after cleaning PDMS stamp with the soxhlet extractor, neither SPIM (Figure 3.5d) nor LAPS images (Figure 3.5e) showed any patterns, confirming that the cleaned PDMS stamp did not leave any residue or damage the monolayer. Thus all the PDMS stamps were cleaned prior to use.

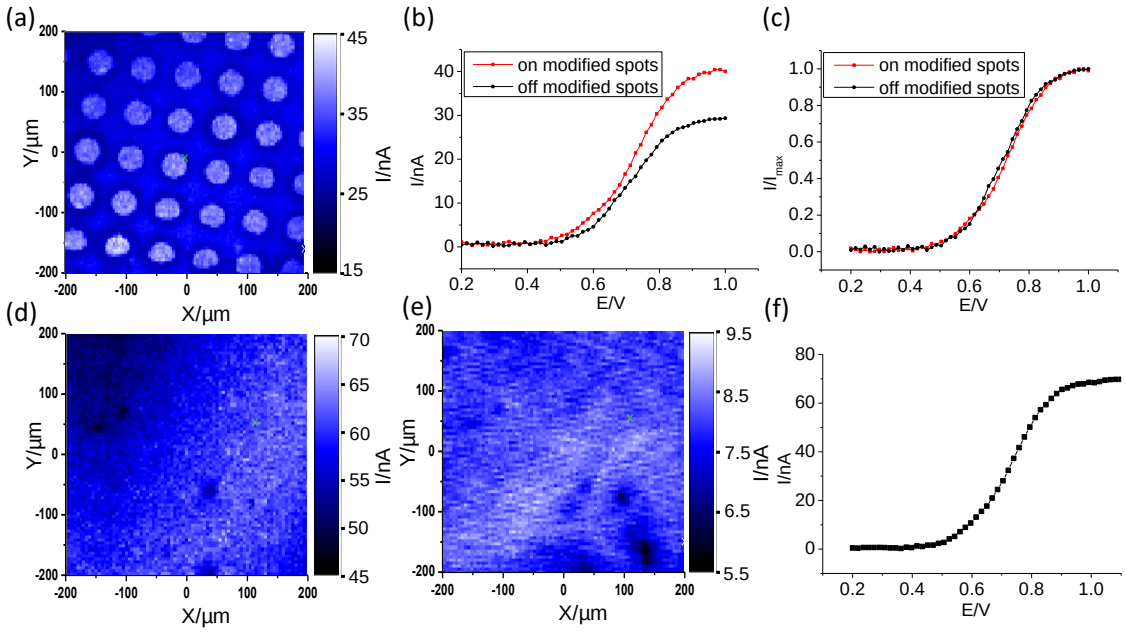

Figure 3.5 (a) SPIM images at a bias voltage of 0.8 V on control sample with uncleaned blank PDMS stamp, (b) the corresponding I-V curves on modified spots and blank 1,8-nonadiyne modified area, (c) normalized I-V curves. (d) SPIM image and (e) LAPS image of control sample with cleaned blank PDMS stamp at bias voltages of 0.8 V and 0.5 V, respectively, and (f) corresponding I-V curve.

3.3.3 Copper residue visualized with LAPS and SPIM.

Figure 3.6a shows the SPIM image of surface 2a after rinsing in 0.5 M HCl solution for 2 min measured at 0.8 V, which is identical to the pattern on the PDMS stamp used. At the selected voltage, the photocurrent was greater on the 'click' reaction modified spots than on the blank 1,8-nonadiyne modified area (also see Figure 3.6b), which was unexpected, as the thickness of the modified spot increased after the 'click' reaction, which should have resulted in a reduced capacitance and thus a decreased photocurrent. In addition, there was also a negative shift of -86 ± 5 mV on the 'click' reaction modified spots compared to the blank 1,8-nonadiyne modified area in the lower part of the normalized *I-V* curves (Figure 3.6c), which was much bigger than a previously reported shift of -50 mV caused by positively charged amino groups [133]. Whilst this is an empirical observation, we speculated that this effect was the result of residual positively

charged copper(I) ions remaining associated with the monolayer, which consequently increased its conductivity thereby increasing the local photocurrent and causing the negative shift of the *I-V* curves. The increase in the maximum photocurrent indicates that copper(I) is not simply adsorbed onto the surface of the monolayer, but that it enters the monolayer. The appearance of a step in the *I-V* curve after µCP indicates the presence of different surface charges within the illuminated spot on the sample due to incomplete coverage caused by the printing process with an insufficient contact of the elastomeric PDMS stamp with the rough SOS substrate (surface roughness ~ 5 nm). This is in agreement with results reported previously for the µCP of polyelectrolytes on monolayer modified SOS surfaces [4].

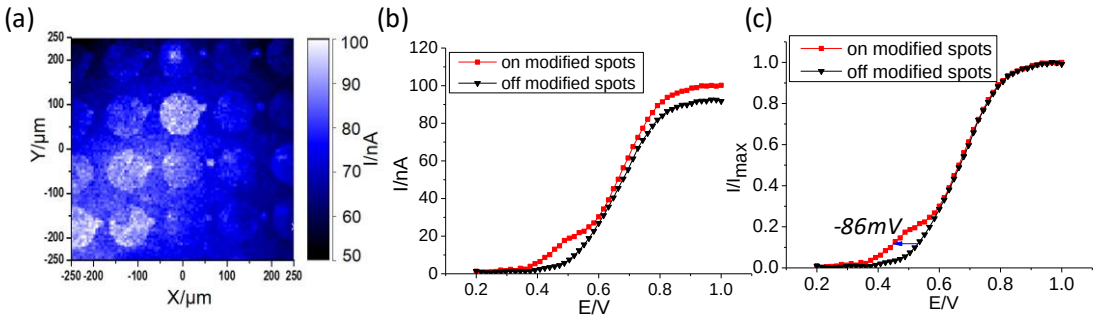

Figure 3.6 The SPIM image of a 1,8-nonadiyne modified SOS sample patterned with 3 azido-1-propanamine with a 'click' reaction (surface 2a) after cleaning with (a) HCl solution and corresponding (b) I-V curves ($I_{max\text{-}on}$ = 101.3 ± 2.7 nA, $I_{max\text{-}off}$ = 91.7 ± 0.6 nA) and (c) normalized curves.

To verify this, a control surface *a* was prepared by printing the copper catalyst without azide on the 1,8-nonadiyne modified surface following the procedure set out in Figure 3.2, and rinsing with 0.5 M HCl solution for 2 min. The corresponding SPIM image at a bias voltage of 0.8 V, also showed an increased photocurrent on modified spots compared to the blank 1,8-nonadiyne modified area (Figure 3.7a and b). The *I-V* curves shifted by - 23 ± 2 mV in the lower part, again indicating positive charge on the modified spots (Figure 3.7c). Thus, the presence of a copper(I) residue on the surface after the 'click' reaction despite cleaning with hydrochloric acid solution was verified using LAPS and

SPIM, although there was an absence of Cu $2p_{3/2}$ emission at ~933 eV in the XPS spectra (Figure 3.3a), demonstrating that LAPS and SPIM are highly sensitive in detecting the presence of copper ions. The copper(I) ion residue was also confirmed by a cyclic voltammogram obtained from the control surface *a*, which showed a peak at 0.24 V, corresponding to the oxidation of copper(I) on the surface [285], while no peak was observed in the cyclic voltammogram measured on a blank 1,8-nonadiyne modified surface (Figure 3.8). Integration of the oxidation peak yielded a surface concentration of 1.1×10^{-11} mol/cm^2.

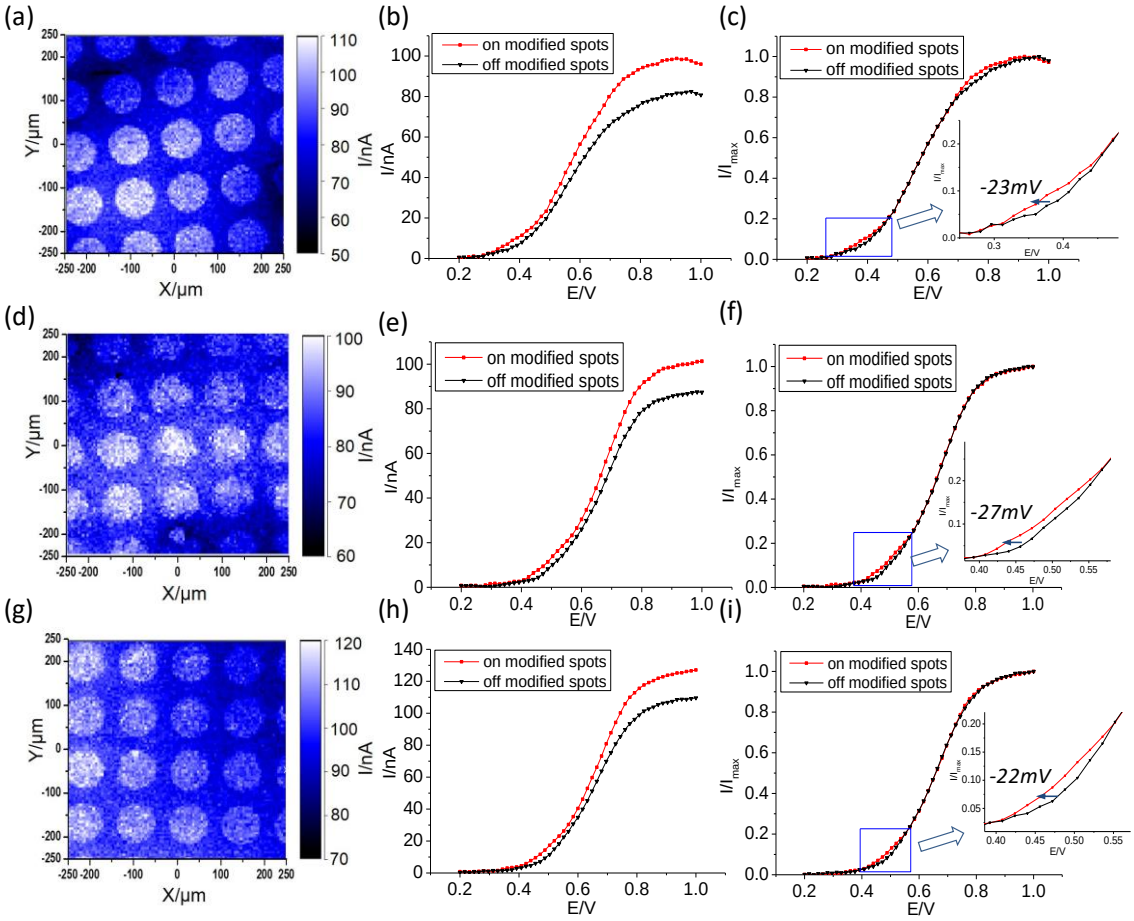

Figure 3.7 SPIM images at a bias voltage of 0.8 V on (a) control surface a, (d) control surface b and (g) control surface c after rinsing with 0.5 M HCl for 2 min, and the corresponding I-V curves (b) ($I_{max\text{-}on}$ = 98.1 ± 1.1 nA, $I_{max\text{-}off}$ = 79.4 ± 1.6 nA), (e) ($I_{max\text{-}on}$ = 98.7 ± 2.6 nA, $I_{max\text{-}off}$ = 87.7 ± 1.0 nA), (h) ($I_{max\text{-}on}$ = 124.4 ± 2.3 nA, $I_{max\text{-}off}$ = 108.6 ± 1.3 nA) on modified spots (red) and non-modified 1,8-nonadiyne areas (black) and

normalized I-V curves (c), (f), (i).

To investigate if a copper(I) residue was also found in 1,8-nonadiyne monolayers for 'click' reactions in organic solvents with subsequent cleaning with HCl solution, 'click' conditions using CuBr and TMEDA in DMSO, which have frequently been used to immobilize water-immiscible molecules via 'click' reactions on alkyne-terminated surfaces [146, 175, 183, 281], were tested and investigated with LAPS and SPIM. Figure 3.7d shows the SPIM image of control surface *b* after rinsing with HCl solution at a bias voltage of 0.8 V, which also displayed a greater photocurrent on modified spots than the unmodified area of 1,8-nonadiyne (also see Figure 3.7e), indicating a smaller impedance on modified spots and, hence, the presence of trapped copper ions in the monolayer, which enhanced its conductivity. The nature of the entrapment is not known. It is possible that copper(I) ions are chelated by the terminal alkyne group of the monolayer or that they penetrate deeper into the monolayer. The corresponding normalized *I-V* curves shifted by -27 ± 2 mV in the lower part for the modified area (Figure 3.7f), resulting from the positively charged copper ions, which was also comparable to the shift of -23 mV obtained from the previous control surface *a* after rinsing with HCl.

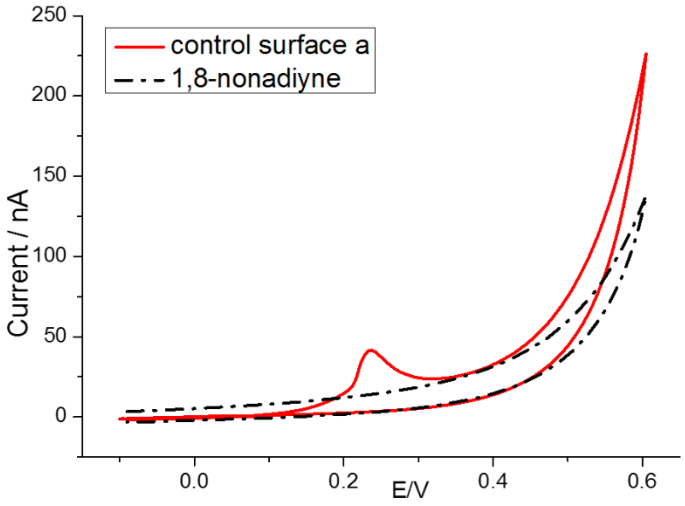

Figure 3.8 Cyclic voltammograms of control surface a after rinsing with HCl (red solid line) and a blank 1,8-nonadiyne modified surface (black dashed line) in 10 mM PBS

solution (pH 7.4) with a scan rate of 50 mV/s.

3.3.4 Strategies for avoiding a copper(I) residue after 'click' modification.

A residue of copper(I) ions in the monolayer following 'click' modification is undesirable because it can interfere with the subsequent function of the device, as clearly demonstrated by the LAPS and SPIM measurements presented above, and because copper ions could adversely affect biological systems. Several strategies were investigated to avoid copper contamination of the monolayer. It was hypothesized that if a stable, bulky copper(I) complex with a large counter ion was employed as the catalyst, it might prevent copper from entering the monolayer. Therefore tetrakis(acetonitrile) copper(I) hexafluorophosphate was combined with the bulky ligand tris[(1-benzyl-1H-1,2,3-triazol-4-yl)methyl] (TBTA) [286-288] and the complex used to catalyze the CuAAC reaction. Again, an increased photocurrent on the 'click' modified spots in the SPIM image (Figure 3.7g and h) and a shift of -22 ± 2 mV in the lower part of the corresponding normalized *I-V* curves (Figure 3.7i) with respect to the 1,8-nonadiyne modified area on control surface *c* were observed, revealing the existence of a copper residue in the monolayer. From the above experiments, it was apparent that rinsing the samples with HCl after 'click' modification was insufficient to remove the copper(I) residue completely, irrespective of the type of copper catalyst or the solvent used for 'click' modification.

Another common method used for removing copper after a 'click' reaction has been rinsing the surface with a 0.05% w/v EDTA solution (pH=7.4) for 24 hours [180, 181, 289]. It is noteworthy that both HCl and trifluoroacetic acid (TFA) were used to adjust the pH of the tetrasodium salt of EDTA solution to be 7.4 in our study, abbreviated as EDTA/HCl and EDTA/TFA solutions below. Figure 3.9a shows the LAPS image of control surface *a* following rinsing with EDTA/HCl at a bias voltage of 0.5 V. The corresponding *I-V* curves displayed no maximum photocurrent difference (Figure 3.9b),

but again a small voltage shift of -10 ± 1 mV in the lower part between modified spots and the blank 1,8-nonadiyne modified area (Figure 3.9c) indicates that whilst more copper has been removed compared to the cleaning method with aqueous HCl solution, there is still residual copper in the monolayer. This result also reveals that the photocurrent measurements are more sensitive in detecting surface charges than impedance. The LAPS and SPIM results observed after rinsing the control surface with an EDTA solution obtained by adjusting the pH of a solution of the disodium salt of EDTA to 7.4 with sodium hydroxide were similar to those after rinsing with EDTA/HCl. In contrast, no pattern was observed in the SPIM image at 0.8 V (Figure 3.9d) and the LAPS image at 0.5 V (Figure 3.9e) of the control surface after rinsing in EDTA/TFA solution for 24 hours. Thus, rinsing samples after a 'click' reaction with an EDTA/TFA solution is clearly more effective in removing copper residues than an EDTA/HCl solution or an EDTA solution without HCl. We assume that the presence of trifluoroacetate ions in the EDTA solution is required to remove copper ions from the film, possibly going through the intermediate of a copper(I) trifluoroacetate alkyne complex [290].

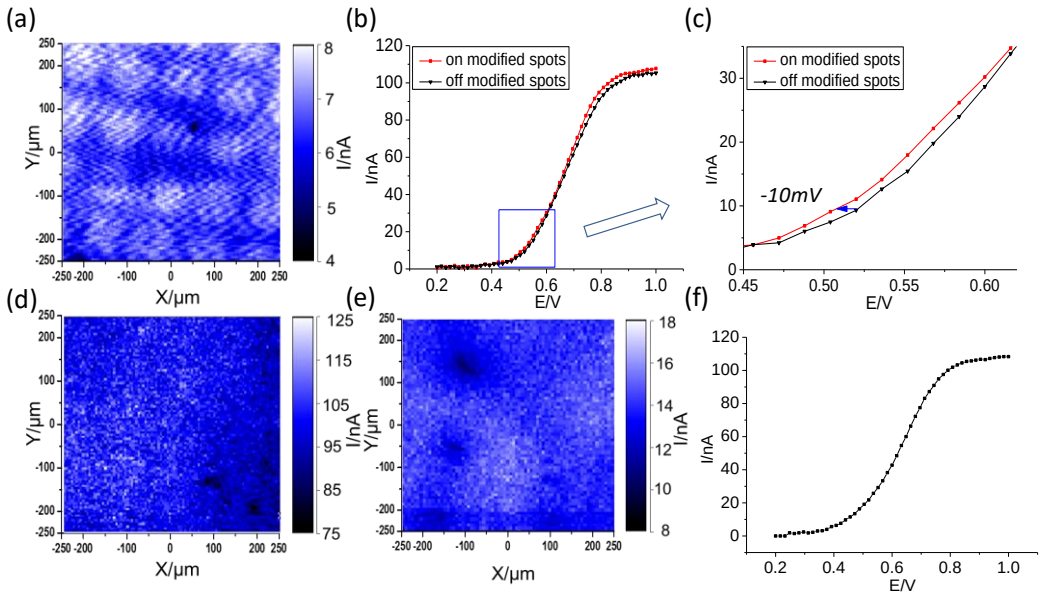

Figure 3.9 (a) LAPS image of control surface a rinsing with EDTA/HCl for 24 hours at a bias voltage of 0.5 V, (b) the corresponding I-V curves on modified spots and blank 1,8-nonadiyne modified area ($I_{max\text{-}on}$ = 104.5 ± 1.4 nA, $I_{max\text{-}off}$ = 105.0 ± 3.6 nA), and (c)

enlarged I-V curves with a voltage shift of -10 mV. (d) SPIM image and (e) LAPS image of control surface a rinsing with EDTA/TFA for 24 hours at bias voltages of 0.8 V and 0.5 V, respectively, and (f) corresponding I-V curve.

3.3.5 SPIM and LAPS measurements of a click modified sample after removal of the copper residue.

Figure 3.10a shows a SPIM image of surface 2a after rinsing in EDTA/TFA solution for 24 hours at a bias voltage of 0.8 V. A dark pattern was obtained, i.e. on the 'click' modified spots, the photocurrent was smaller than on the blank 1,8-nonadiyne modified area, indicating an increased impedance, as expected. The corresponding *I-V* curves measured on 'click' modified spots and off the 'click' modified area (1,8-nonadiyne modified background) are shown in Figure 3.10b. A decrease of ~10% of the maximum photocurrent was obtained in the 'click' modified area, corresponding to a capacitance of 0.86 ± 0.06 μF/cm^2 calculated using an equivalent circuit model and simplified equation described previously [3]. This is around 1.6 times smaller than the capacitance of the organic monolayer of 1,8-nonadiyne alone (1.44 μF/cm^2), which is in agreement with the thickness ratio of the 1,8-nonadiyne monolayer to the 'click' modified monolayer measured by ellipsometry. There was a negative shift of -65 ± 5 mV on the 'click' modified spots compared to the 1,8-nonadiyne modified area (Figure 3.10c), which equals the shift difference between the sample with 'click' reaction after cleaning with HCl solution and the corresponding control sample, demonstrating the successful removal of the copper residue. The potential shift (-65 mV) for this NH_2-terminated surface was greater than previously reported values (-50 mV) for surfaces modified with a longer amino group terminated monolayer of 11-azido-3,6,9-trioxaundecan-1-amine. The hydrophilic nature of the 11-azido-3,6,9-trioxaundecan-1-amine may have allowed electrolyte to enter the monolayer and partially screened the positive charge of the amino groups in contrast to the more hydrophobic 3-azido-1-propanamine used in this work [291].

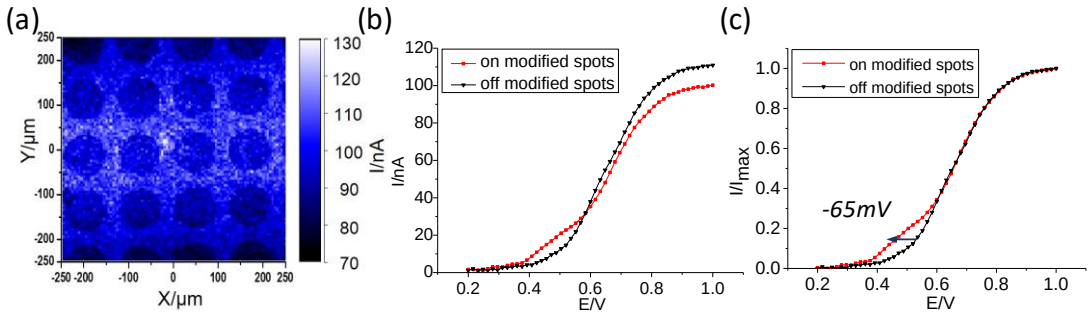

Figure 3.10 (a) The SPIM image of a 1,8-nonadiyne modified SOS sample patterned with 3-azido-1-propanamine with a 'click' reaction (surface 2a) after cleaning with EDTA/TFA solutions, and corresponding (b) I-V curves ($I_{max\text{-}on}$ = 100.2 ± 0.1 nA, $I_{max\text{-}off}$ = 112.9 ± 2.1 nA) and (c) normalized curves.

3.4 Summary

In this study, we have shown that HCl is not effective in removing the copper residue after 'click' reactions on alkyne-terminated self-assembled organic monolayers on silicon surfaces, which, although not detectable by XPS, was characterized successfully by LAPS and SPIM. A voltage shift of -23 mV in the depletion region and the increased maximum photocurrent in the inversion region of the photocurrent curves for the control sample, where only the copper(I) catalyst without azide was printed onto the sample, indicated a positively charged surface and a decreased impedance resulting from copper(I) ions in the monolayer. The presence of the copper(I) residue was also confirmed by the oxidation peak in the cyclic voltammogram on the control sample. The copper residue was completely removed by rinsing samples in a tetrasodium salt of EDTA solution, the pH of which was adjusted to 7.4 with TFA, after the 'click' reaction. The success of the 'click' reaction was confirmed using LAPS and SPIM. The surface charge properties of the amino group introduced via 'click' reactions by μCP was shown by a voltage shift of - 65 mV in the depletion region of the photocurrent curves. The impedance of the 'clicked' monolayers was detected using SPIM. It is envisaged that the high sensitivity of LAPS and SPIM to surface charges and impedance demonstrated in this study makes them promising techniques to measure the electrical properties of biomolecules on surfaces.

4. Patterning osteoblasts on silicon on sapphire substrate in serum-free medium

4.1 Introduction

Controlling cell adhesion on surfaces has attracted more and more attention in recent years due to its great significance in cell biology [292-294], tissue engineering [295-297], drug delivery devices [298, 299], cell-based biosensors [300, 301], and biochips [302-304]. Various methods have been developed to realize the manipulation of cell adhesion, including physically or chemically patterning the substrate surfaces by photolithography [226, 227, 229, 282, 305], soft lithography [237, 306-308], plasma lithography [304, 309], laser ablation [310], laminar-flow patterning [311] and electrochemical patterning [312-314].

One particularly impressive approach to control cell adhesion and patterning is the immobilization of RGD (Arg-Gly-Asp) containing peptides to selected areas of the substrate [315-317]. Various RGD containing peptides have been used to functionalize substrates to enhance cell adhesion, including linear peptides and cyclic peptides [318-322], since their first discovery by Ruoslahti *et al* [323] as a cell binding site in fibronectin. Verrier *et al.* [319] compared the function of RGD containing peptides with different structures (linear and cyclic) in cell adhesion. They cultured human bone marrow stromal cells on cell-culture plates coated with various peptides. The results of cell adhesion assays demonstrated that cells preferred to adhere to surfaces containing cyclic peptides compared to linear ones. Another advantage of the cyclic RGD containing peptides is their high stability and specificity compared to the liner RGD containing peptides, which are susceptible to chemical degradation [324].

In this work, a cyclic-(RGDfK) peptide was chosen as the ligand to control cell attachment because of the presence of the ε-amino group of the lysine side chain which is easily functionalized [316] in addition to the aforementioned advantages. A

biofunctional linker, 4-azidophenyl isothiocyanate (API), was used to modify this cyclic-RGDfK peptide with an azide group [289], allowing a CuAAC 'click' reaction to be performed on the 1,8-nonadiyne modified SOS substrate as described in Chapter 3. To pattern the SOS substrate with cyclic-RGDfK peptide, a 'click' reaction combined with microcontact printing was performed as demonstrated in Chapter 3. Cellular patterning was achieved by seeding cells on the substrate patterned with the cyclic-RGDfK peptide in serum-free medium, which has been used to prevent the surface chemical patterns from being covered by the proteins adsorbed from the serum containing medium [229, 325].

4.2 Experimental methods

4.2.1 Materials

SOS with a 1 μm-thick silicon (100) layer (boron doped, 0.1 Ω·cm) on a 475 μm thick sapphire substrate was purchased from Monocrystal, Russia. Double-polished silicon (100) (boron doped, 10−30 Ω·cm, 500 μm thickness) was purchased from Si-MAT, Germany. All chemicals and reagents were purchased from Sigma-Aldrich, including the cell culture materials of Dulbecco's Modified Eagle's Medium (DMEM), Fetal Bovine Serum (FBS), penicillin-streptomycin, Dulbecco's Phosphate Buffered Saline (DPBS, pH 7.4, 10 mM phosphate buffer solution containing 137 mM NaCl and 2.7 mM KCl) and Trypsin-EDTA, unless otherwise noted. Cyclic-RGDfK peptide (≥ 95%) was purchased from GenScript.Inc. Before its modification, the peptide was purified with a StratoSpheres Solid Phase Extraction tube (Agilent Technologies) to remove the TFA salt. Actin staining reagent Alexa Fluor® 633 Phalloidin was purchased from Lift technologies Ltd. Osteoblasts MG63 (Human osteosarcoma cell line) were provided by Dr Karin Hing's group.

4.2.2 Modification of cyclic-RGDfK peptide with 4-azidophenyl isothiocyanate (API)

The peptide was modified with 4-azidophenyl isothiocyanate (API) through the reaction

of the primary amino group of the peptide lysine residue with the isothiocyanate group to form the azido-peptide as displayed in Figure 4.1a. Briefly, API (11 mg, 60 μmol) was dissolved in DMSO (1mL) to make a solution (60 mM). Then the same molar equivalents of peptide were added to the API solution and the mixture stirred at room temperature for 24 h. The mixed solution was used directly for further 'click' reactions on the 1,8-nonadiyne modified surfaces without any further purification. To confirm the reaction had occurred, the crude mixture was characterized by ^{13}C NMR spectroscopy (when the reaction solvent used was d_6-DMSO) and electrospray ionization mass spectrometry (ESI-MS). For ESI-MS, the mixture was diluted with ultrapure water 100 times.

4.2.3 SOS or Si surface functionalization with cyclic-RGDfK peptide

Firstly, the substrate was modified with 1,8-nonadiyne as described in section 2.2, which provides an acetylene bond for the CuAAC 'click' reaction. Subsequently, the peptide modified substrate was obtained through a typical 'click' process as illustrated in Figure 4.1b. The 1,8-nonadiyne modified silicon substrate was placed in a vessel containing the 'click' solution D of the azido-peptide (10 mM, DMSO), CuBr (10 mol% relative to the azide) and TMEDA (20 mol % relative to the azide) for 24 hours in the dark at room temperature. The unreacted reagents were removed by rinsing the substrate consecutively with copious amounts of DMSO, ethanol and water. A further rinsing with 0.05% (w/v) EDTA/TFA solution for 24 h to remove copper residues.

4.2.4 Surface patterning with cyclic-RGDfK peptide via μCP

To pattern the surface with cyclic-RGDfK peptide, a 'click' reaction combined with μCP was carried out following the same procedure described in section 3.2.4, but with 'click' solution D as the 'ink' as displayed in Figure 4.1b. The pattern of the PDMS stamp consisted of circular islands with a diameter of 100 μm and 40 μm intervals. To characterize the peptide modified surface prepared by μCP properly, a chemically homogeneous surface was prepared using a flat featureless PDMS stamp following the

same procedure.

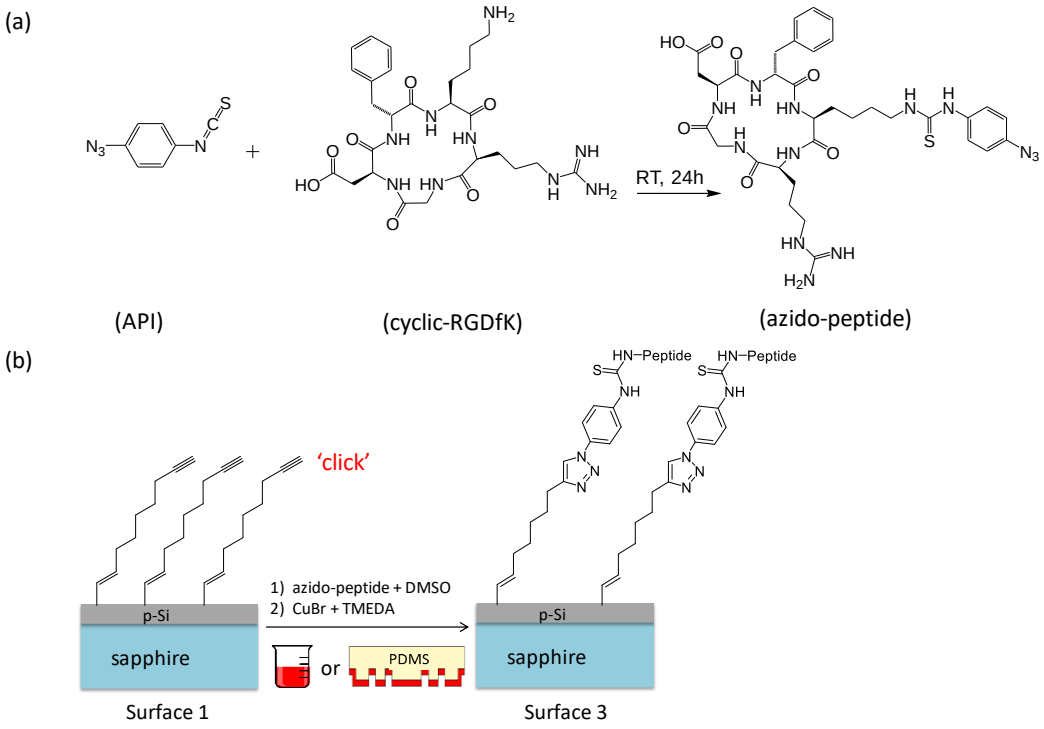

Figure 4.1 (a) Modification of cyclic-RGDfK peptide with API; (b) surface functionality with cyclic-RGDfK peptide via CuAAC 'click' reaction.

4.2.5 Cell culturing and adhesion

Osteoblasts (human osteosarcoma cell line) were provided by Dr Karin Hing's group and cultured with DMEM medium supplemented with 10% fetal bovine serum and 1% penicillin-streptomycin solution in a humidified atmosphere with 5% CO_2 at 37°C with the medium changed every two days. At confluence, cells were passaged by trypsinization and then maintained in the medium. To assess cell adhesion on the RGD peptide modified surface, SOS substrates modified with amino groups which were prepared in Chapter 3 and had a similar water wettability (the water contact angle was 56±2°) and 1,8-nonadiyne monolayers were used as control surfaces. Before seeding cells, samples were sterilized with 70% ethanol and rinsed thoroughly with sterilized water and sterilized PBS solution and blown dry. For cell adhesion assay and cell staining, samples were placed in a 24 well

petri dish. Then cells were washed twice with DPBS solution and trypsinized in a 0.05% trypsin-EDTA solution and centrifuged at 1800 rpm for 5 min. After removing the supernatant, cells were dispersed in serum-free medium (DMEM supplemented with 1% penicillin-streptomycin solution). Then cells were seeded onto samples at a concentration of $5x10^4$ /mL in serum-free medium. Substrates with cells were incubated at 37°C with 5% CO_2 for 24 h for further cell adhesion assay and cell staining experiments. The same incubation protocol was used for both homogeneous and patterned RGD peptide modified substrates.

4.2.6 Cell staining of actin

To prepare samples for staining of actin, substrates with adherent cells were rinsed twice with DPBS solution and then fixed in 1 mL of 4% formaldehyde in DPBS for 10 min at room temperature. After three washes with DPBS, cells were permeabilized by incubation in 1 mL 0.2% Triton X-100 in DPBS for 3 to 5 min and then washed with DPBS three times. To block the non-specific binding, substrates were cultured with 5% BSA in DPBS for 30 min, followed by three washes with DPBS. Actin staining was obtained by using phalloidin labelled with Alexa Fluor® 633 dye, which shows optimal excitation at 632 nm and emission at 647 nm (red). Substrates were incubated with 0.5 mL phalloidin solution (10 µL phalloidin, 0.5 mL of 5% BSA/DPBS) for 1 hour at room temperature and then washed with DPBS five times.

4.2.7 LAPS and SPIM measurement

The LAPS and SPIM setup has been shown in section 2.4. In this work, the sensor chips used for LAPS measurements were all based on SOS substrates. The femtosecond laser was used for LAPS/SPIM measurements. The modulation frequency was 1 kHz. For single cell imaging with LAPS/SPIM, cells were seeded onto a homogenous RGD peptide modified SOS substrate in the assembled LAPS chamber at a concentration of $2.5x10^4$/mL and incubated at 37°C with 5% CO_2 for 24 hours. Before LAPS measurement,

the cell culture medium was replaced with DPBS. A white light illuminated the sensor from the front side to obtain an optical image of the cells from the camera.

4.3 Results and discussion

4.3.1 Functionalization of peptide with azide group

^{13}C NMR and ESI-MS were used to characterize the reaction of peptide with API. ^{13}C NMR spectra were recorded using a Bruker Avance 400 MHz spectrometer employing DMSO-d_6 as the solvent as shown in Figure 4.2a. The sample concentration was approximately 47 mg/mL. Chemical shifts were referenced to the residual carbon peak of DMSO-d_6 at 39.5 ppm. The ^{13}C NMR spectrum in DMSO-d_6 for the modified peptide clearly shows one additional peak at 180.5 ppm, which corresponds to the C=S bond [326], compared to ^{13}C NMR in DMSO-d_6 for the starting materials of peptide and API, indicating the successful coupling of peptide with API.

Figure 4.2b shows the ESI-MS spectrum of the mixture of API and peptide after the reaction. There is an obvious peak at 780.2, which is consistent with the molecular weight expected for the azido-peptide. Meanwhile, there are no obvious peaks around 176.2 and 603.7, which correspond to the starting materials, API and peptide, respectively, indicating the high yield of the coupling reaction of API with the peptide.

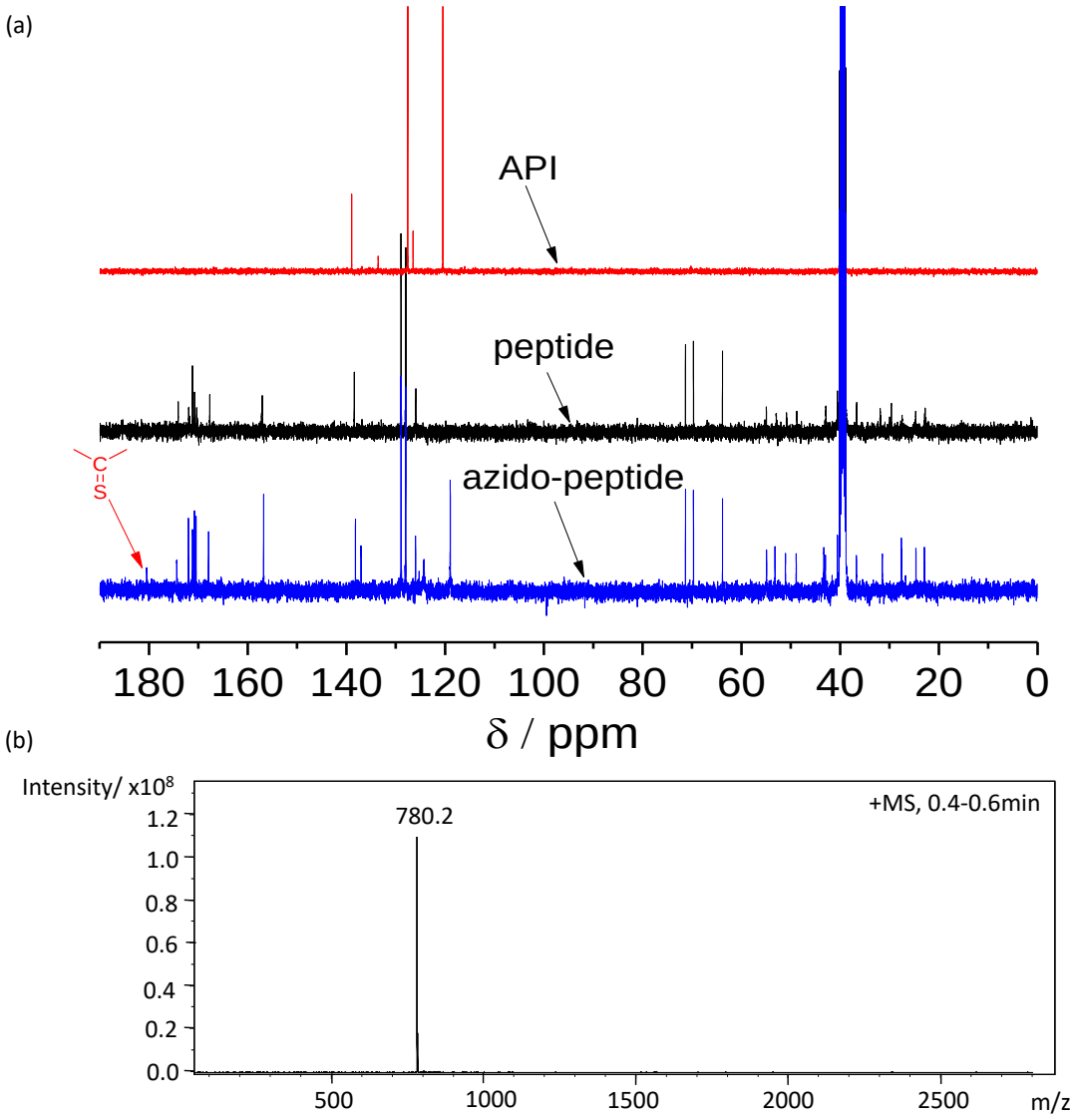

Figure 4.2 (a) ^{13}C NMR spectra of the starting materials and the product of azido-peptide; (b) ESI-MS spectrum of the unpurified azido-peptide.

4.3.2 Characterization of RGD peptide modified SOS or Si substrate

The success of the 1,8-nonadiyne modification has been demonstrated in section 3.3 by water contact angle, ellipsometry and XPS, which were also used to characterize the RGD peptide modified substrates. As displayed in Table 4.1, the water contact angle of RGD peptide modified substrate decreased to 57±3°, which was due to the hydrophilic property of the RGD peptide. The ellipsometric thickness of the RGD peptide functionalized monolayer increased to 2.17 ± 0.03 nm, indicating the success of the 'click' reaction.

Figure 4.3 shows the XPS results of the RGD peptide modified SOS substrate. There is an obvious N 1s peak at ~ 401 eV in the XPS survey spectrum (Figure 4.3a), revealing the successful attachment of the azido-peptide. The narrow scan signal of the N 1s region (Figure 4.3d) was deconvoluted and fitted to three peaks at 398.8 eV, 400.2 eV and 401.5 eV, which were assigned to C=N, C-N/N-N=N, and N-N=N, respectively [182, 327]. The absence of a peak at 403 eV, which corresponds to the central electron-deficient nitrogen in the azido groups, shows that there was no physisorption of the azide onto the silicon surface. The narrow scan from the C 1s region (Figure 4.3c) was deconvoluted into four peaks assigned to Si-C=C (283.8eV), C−C (285.0 eV), C−N/−O (286.7 eV) and C=O (288.7 eV) [322]. Importantly, there was a negligible amount of SiO_X detected in the 101-104 eV region [170] in the narrow scan of Si 2p (Figure 4.3b) on the peptide modified surface, indicating a high-quality surface. The surface coverage of the 1,8-nonadiyne monolayer on SOS surface was calculated to be 46% relative to the surface Si-H sites according to the atomic ratio of C:Si (~ 0.38) derived from XPS result using the model proposed by Cicero *et al.* [186], which was comparable with a surface coverage of 48% as the literature reported [183]. Using the same model, the surface coverage of the cyclic-RGDfK peptide monolayer was calculated to be 15% relative to the surface Si-H sites based on the atomic ratio of carbon (34.62 %) to silicon (50.66 %), indicating a 33% conversion of the surface acetylenes to corresponding triazoles. This low conversion could be caused by the steric hindrance of the cyclic-RGDfK peptide. For the peptide modification via μCP, similar results were obtained from water contact angle, ellipometry (see Table 4.1) and XPS (see Figure 4.3a), indicating the capability of using μCP to perform CuAAC 'click' reaction on SOS or Si surface. While the surface coverage for the peptide modified monolayer prepared via μCP was estimated to be 12% relative to the surface Si-H sites, with the atomic ratio of carbon (29.84%) to silicon (54.63%) using the same model already mentioned, which was slightly smaller than that prepared by a 'click' reaction in solution. This could be caused by the insufficient contact of the PDMS stamp

with the rough SOS substrate (surface roughness ~ 5 nm).

Table 4.1 Contact angle and ellipsometric thickness of 1,8 nonadiyne modified substrate and peptide modified substrate.

Surface	Water contact angle (°)	Ellipsometry thickness (Å)
SOS-nonadiyne	86±1	9.2±0.3
SOS-peptide	57±3	21.7±0.5
SOS-peptide*	58±2	21.4±0.4

*surface prepared by μCP using a flat featureless PDMS stamp.

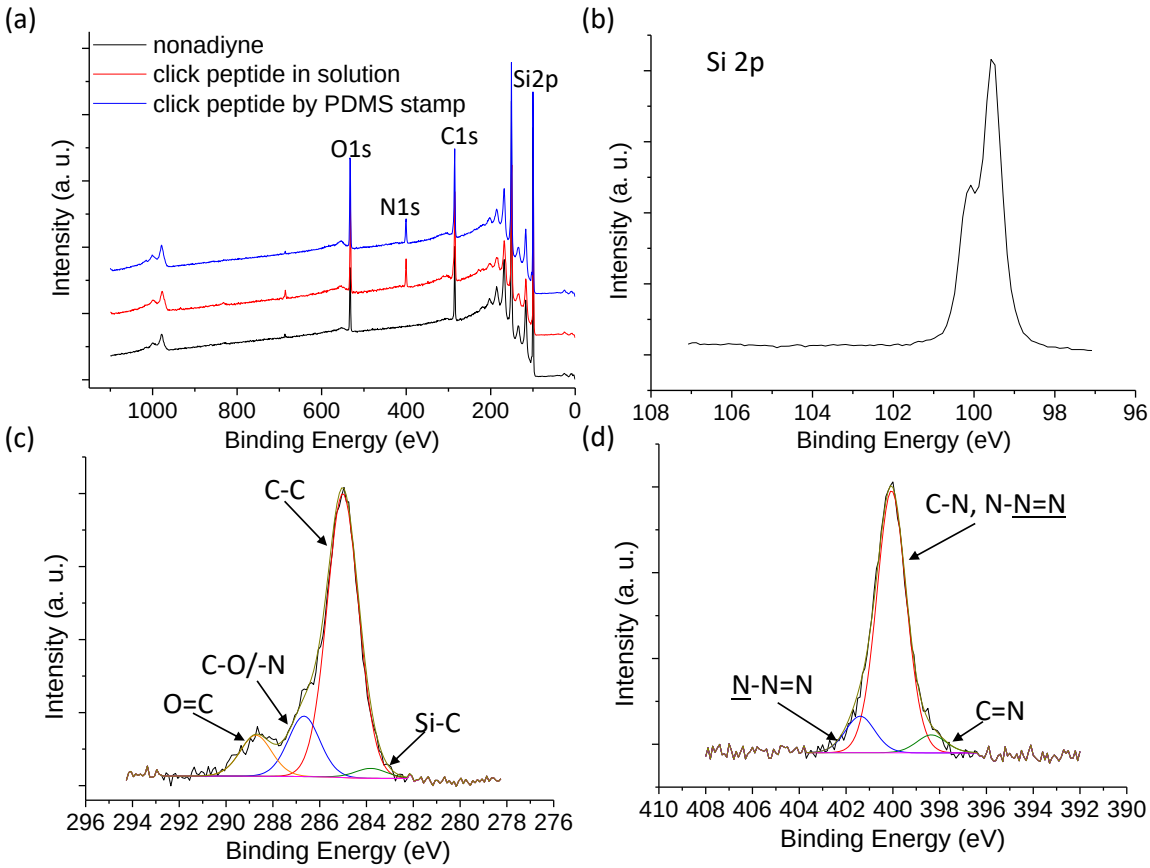

Figure 4.3 XPS spectra of (a) 1,8-nonadiyne modified surface (black line) and cyclic-RGDfK peptide modified surface prepared with a 'click' reaction in solution (red line) and via μCP (blue line) ; narrow scans of (b) Si 2p and (c) C1s and (d) N 1s of cyclic-RGDfK peptide modified surface.

4.3.3 The pH response of the peptide modified SOS surface with LAPS

The pH sensitivity of the peptide modified substrate was tested with LAPS. Figure 4.4 shows the normalized *I-V* curves measured in a series of buffered solutions with pH range from 3 to 9.5, and the corresponding calibration curve. The pH sensitivity was only 26 mV/pH, which was much smaller than the Nernstian response of 59 mV/pH, but similar to the pH response of 30 mV/pH on undecylenic acid modified SOS substrate [4]. This low pH sensitivity could be due to the low density of surface reactive sites on the peptide modified surface, which is caused by the low surface coverage of the peptide monolayer as calculated in section 4.3.2.

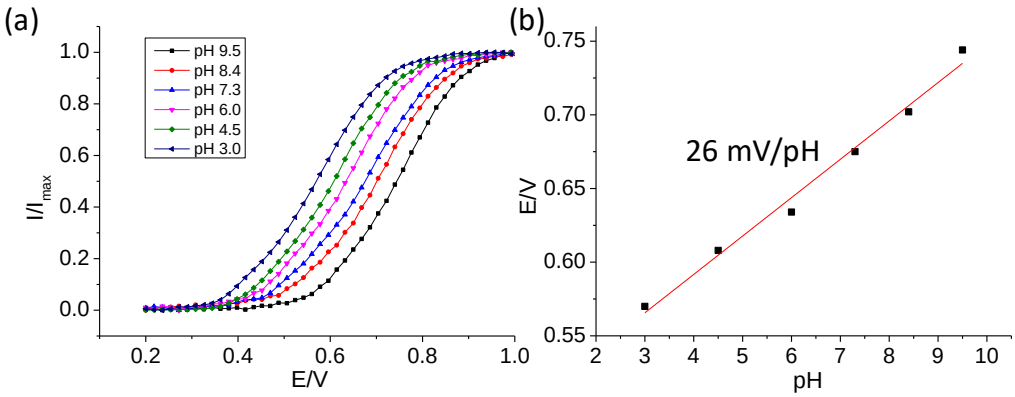

Figure 4.4 (a) LAPS I-V curves of peptide modified SOS substrate at different pH values; (b) the pH sensitivity of the peptide modified surface (R^2=0.9886).

4.3.4 Cell adhesion

After culturing cells on samples for 24 h, samples were washed with DPBS solution twice to remove the unattached and loosely-attached cells. The number of cells on the cyclic-RGDfK peptide modified sample surface (see Figure 4.5a) was much higher than that on the NH_2-terminated surface (see Figure 4.5b) and alkyne-terminated surface (see Figure 4.5c), indicating that functionalization with cyclic-RGDfK peptide did enhance cell adhesion.

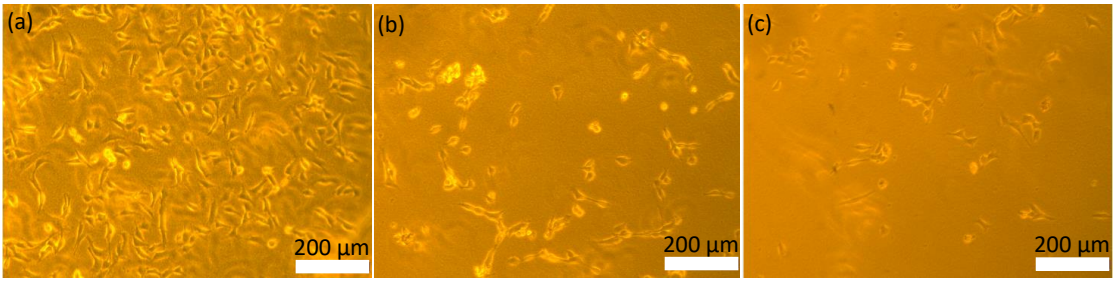

Figure 4.5 Optical images of osteoblasts cultured on (a) cyclic-RGDfK peptide modified, (b) NH_2-terminated and (c) alkyne-terminated surfaces.

The cytoskeleton architecture also showed a big difference on these three surfaces with different functionalities as demonstrated in Figure 4.6. The cells were well spread on cyclic-RGDfK peptide modified surface compared to the alkyne-terminated and NH_2-terminated surfaces. The actin filaments in the cells cultured on cyclic-RGDfK peptide were well-aligned along the long axis of the cells, while in the cells cultured on NH_2–terminated and alkyne-terminated surfaces, the actin was unevenly distributed or presented a thick layer at the cell borders, indicating improved adhesion of osteoblasts on the cyclic-RGDfK peptide modified surface compared to the NH_2–terminated and alkyne-terminated surfaces [328].

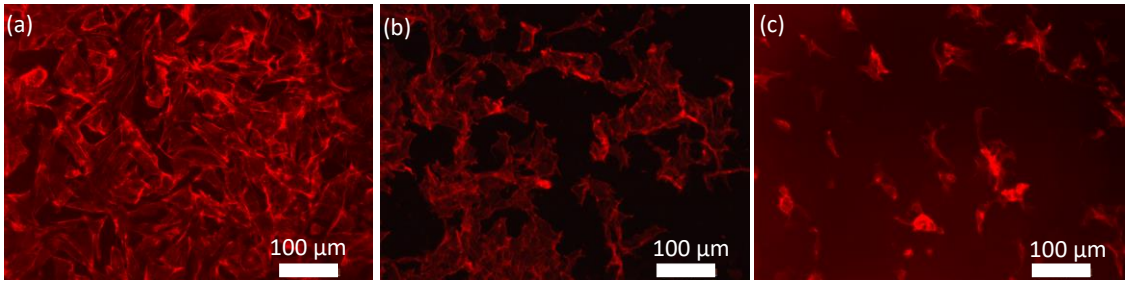

Figure 4.6 Fluorescent images of actin stained by Alexa Fluor® 633 Phalloidin in osteoblasts cultured on (a) cyclic-RGDfK peptide modified, (b) NH_2-terminated and (c) alkyne-terminated surfaces.

4.3.5 Cell patterning

To pattern the osteoblasts, an SOS substrate patterned with cyclic-RGDfK peptide via µCP was used to culture cells. Figure 4.7a shows the optical image of the pattern of

osteoblasts obtained after seeding cells on the cyclic-RGDfK peptide patterned substrate and incubating for 24 hours at 37°C with 5% CO_2 at a concentration of $5x10^4$ /mL in serum-free medium, which was in agreement with the pattern on the PDMS stamp of 100 µm dots separated by 40 µm gaps (see Figure 4.7b). Most cells were attached and confined to the circular island area, indicating that cells prefer the cyclic-RGDfK peptide modified surface to the alkyne-terminated surface. As a control experiment, cells were seeded onto a homogenous cyclic-RGDfK peptide modified surface following the same protocol as described above, where no cell pattern was formed (see Figure 4.5a). Thus, this cell patterning also in turn validated the success of the chemical patterning of cyclic-RGDfK peptide on the SOS substrate.

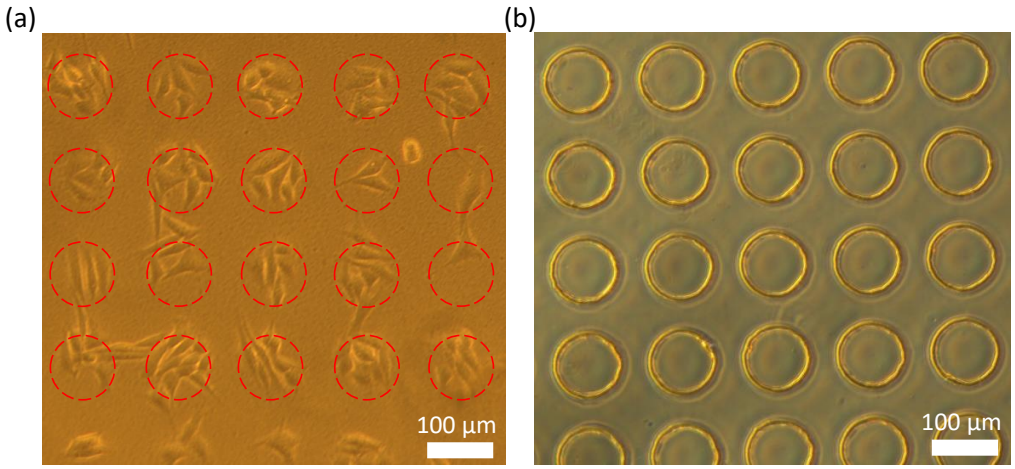

Figure 4.7 Optical images of (a) osteoblasts patterns on patterned cyclic-RGDfK peptide modified SOS substrate and (b) patterns on PDMS stamp used in µCP cyclic-RGDfK peptide with 100 µm dots separated by 40 µm gaps.

4.3.6 Single cell imaging with LAPS/SPIM

LAPS and SPIM measurement based on SOS substrates using a femtosecond laser with two-photon effect as the light source has been demonstrated to be possible with very high resolution (0.8 µm) [4, 15] and has been successfully applied to image the impedance of collapsed microcapsules with unprecedented detail by our group [3], therefore the same photocurrent measurement system was used in this work. Before LAPS and SPIM

measurement of a single cell using the femtosecond laser, its two-photon effect was validated as reported previously [11]. The photocurrent dependence on the light intensity was measured using the femtosecond laser at 1250 nm and a diode laser at 405 nm, respectively. Figure 4.8 displays the double logarithmic plots of photocurrent versus intensity for both lasers, which showed linear relationships. A slope close to 1 was obtained for the diode laser, indicating its single photon effect as expected. In contrast, the slope for the femtosecond laser was close to 2, demonstrating its two-photon effect.

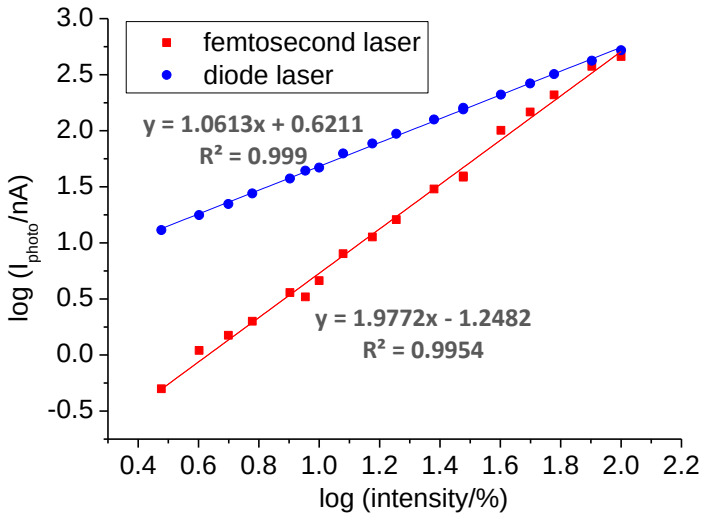

Figure 4.8 Photocurrent dependency on the light intensity of the diode laser and femtosecond laser.

To make sure that the optical image obtained from the camera is aligned with the photocurrent image measured with the femtosecond laser, a calibration experiment was performed using a 1,8-nonadiyne monolayer modified SOS sample with an SU 8 photoresist pattern prepared by photolithography. Figure 4.9a showed the SPIM image of the photoresist pattern measured with the femtosecond laser at a bias voltage of 0.8 V, which matches the optical image obtained from the camera as displayed in Figure 4.9b, revealing a good alignment of the femtosecond laser and the camera. The small photocurrent on the photoresist coated area was due to the high impedance of the photoresist.

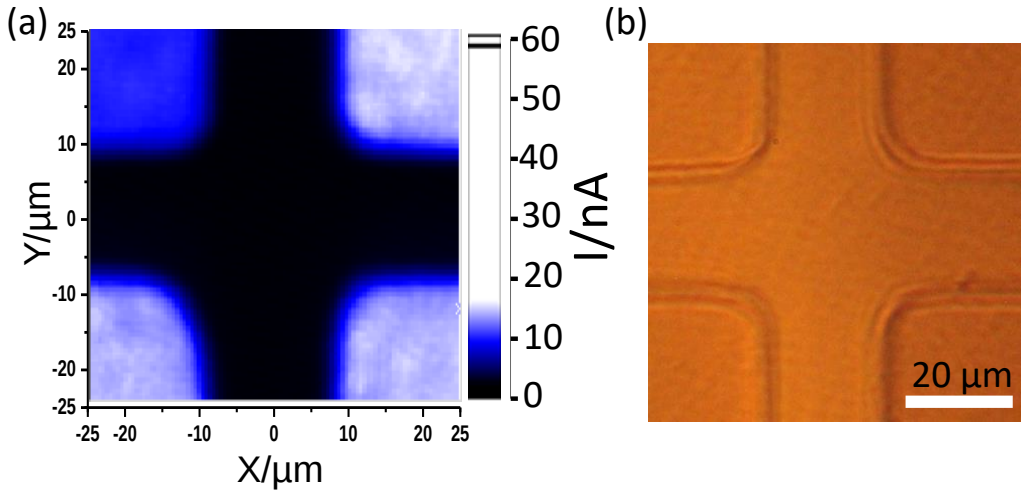

Figure 4.9 (a) SPIM image of the photoresist pattern measured with the femtosecond laser at a bias voltage of 0.8 V and (b) corresponding optical image from the camera.

Figure 4.10 shows the photocurrent imaging results of single osteoblasts cultured on cyclic-RGDfK peptide modified SOS substrate with the femtosecond laser. However, there were no photocurrent contrasts on and off cells both, in the SPIM image which was measured at a bias voltage of 0.8 V (see Figure 4.10a) and in the LAPS image measured at 0.6 V (see Figure 4.10b), although there was a clear optical image of the osteoblasts from the camera (see Figure 4.10c), which could be ascribed to the poor sensitivity of the peptide modified surface to surface charge difference and the low impedance of single cells compared to the high impedance of the SOS substrate.

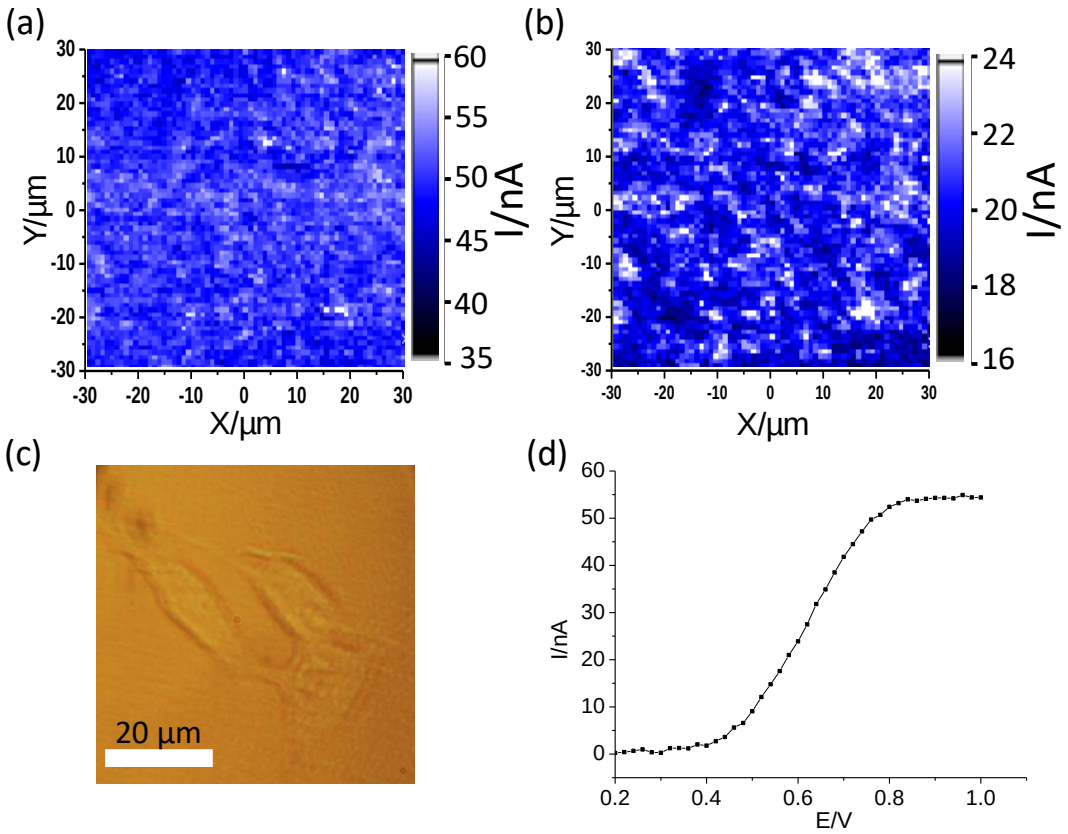

Figure 4.10 (a) SPIM image and (b) LAPS image of the osteoblasts cultured on cyclic-RGDfK peptide modified SOS substrate at a bias voltage of 0.8V and 0.6V with femtosecond laser, respectively, and corresponding (c) optical image of the osteoblast from camera and (d) I-V curve.

A series of similar experiments attempting to image single cells with LAPS and SPIM were also attempted on 1,8-nonadiyne and 3-azido-1-propanamine modified SOS substrates and with another cell type (rat neuroblastoma B50) cultured on the aforementioned surfaces (peptide modified, alkyne-terminated and NH_2-terminated SOS substrates) using the same photocurrent measurement system. However, none of the LAPS and SPIM results showed any photocurrent contrast of cells images, indicating that LAPS and SPIM based on organic monolayers modified SOS substrates using a two-photo effect for charge carriers generation were not sensitive enough for the detection of the surface charge and the impedance of single cells. This could be explained by the gap between the cell and the substrate in contrast to the LAPS images of multilayer yeast cells

which have been reported by our group recently [9], where the yeast cells were pushed against the substrate using agarose gel to make a close contact of the cells with the substrate. The LAPS measurements were carried out using an electrolyte solution with high ionic strength (~150 mM), and under this condition the Debye length was less than 1 nm [291], which makes it difficult to detect the surface charge of single cells.

4.4 Summary

In summary, cyclic-RGDfK peptide was successfully modified on the substrate via a CuAAC 'click' reaction, which was validated by the water contact angle, ellipsometry and XPS results. The cell adhesion assay showed that there were more cells attached on the cyclic-RGDfK peptide modified surfaces compared to the amine-terminated and alkyne-terminated monolayers modified surfaces, demonstrating that this RGD containing peptide does enhance the attachment and affinity of the cells on the surface. An SOS surface patterned with the cyclic-RGDfK peptide was obtained by μCP combined with the CuAAC 'click' reaction. Furthermore, cell patterning was achieved by culturing cells on the cyclic-RGDfK peptide patterned SOS substrate, which in turn verified the success of the chemical patterning of cyclic-RGDfK peptide via μCP on SOS substrates.

Photocurrent imaging of single cells (both osteoblasts and neurons) with LAPS and SPIM using a femtosecond laser with a two-photon effect as the light source was attempted on the cyclic-RGDfK peptide modified SOS substrate, 1,8-nonadiyne modified SOS substrate and 3-azido-1-propanamine modified SOS substrate, respectively. However, no photocurrent contrast was observed on and off cells in both LAPS and SPIM images for all of the attempts, which is attributed to the poor sensitivity of the present LAPS and SPIM system to single cells surface charge and impedance. Despite the failure of the direct imaging of the electrical parameters of single cells, the surfaces developed could be adapted for measuring metabolites and ion concentrations in the future.

To solve the aforementioned problems, an alternative semiconductor material was proposed and in the following chapter the preliminary data on photocurrent imaging of single cells with this substrate are presented.

5. Preliminary results of single cells imaging using light-addressable potentiometric sensors with ITO coated glass as the substrate

5.1 Introduction

Live-cell imaging methods that have been used to investigate the structural organization and dynamic processes of living cells or tissues non-invasively comprise optical microscopies and electrochemical imaging methods. Optical microscopy, especially fluorescence microscopy, is most widely performed in live-cell imaging for the study of the physiological state of cells, cellular transport or cell growth [329]. Electrochemical imaging methods are alternative techniques for live-cell imaging, including scanning electrochemical microscopy (SECM) [251, 330], scanning ion conductance microscopy (SICM) [257, 258], plasmonic-based electrochemical impedance microscopy (P-EIM) [262], and light-addressable potentiometric sensors (LAPS) [331]. They can map parameters such as Faradaic current, ion conductivity, local impedance, extracellular potentials and charges, which cannot be measured with optical microscopy. SECM maps local electrochemical current by scanning a microelectrode across the surface, while the SICM maps the ion conductance by scanning a nanopipette. Plasmonic-based EIM monitors local impedance by measuring the surface plasmon resonance (SPR) response to an applied ac signal. LAPS measures the local photocurrent in response to the surface potential by illuminating the semiconductor with a focused, modulated laser beam without the need for scanning microtips or labels, which would be highly advantageous for the non-invasive imaging of cells.

Traditional semiconductor materials used as LAPS substrates include bulk silicon which was the first and most commonly used semiconductor substrate in LAPS and SPIM [5]. Sensor substrates based on thin silicon [16, 29], porous silicon [332], and amorphous silicon [17, 25, 27, 28], silicon on insulator (SOI) [11] and ultra-thin silicon on sapphire (SOS) [4, 15] were developed to improve the photocurrent response and the resolution.

Other semiconductor materials such as GaAs [22], GaN [23], and TiO_2 [333] were also investigated as alternative sensor materials for LAPS and light-addressable electrodes. So far, the best resolution of sub-micron (0.8 μm) was achieved by our group using an SOS as LAPS substrate and a focused femtosecond laser with a two-photon effect as the light source. However, using this LAPS measurement system failed to image the electrical parameters of single cells as demonstrated in Chapter 4. Thus, it is of great importance to seek alternative substrate materials for LAPS imaging.

In this work, indium tin oxide (ITO) coated glass was investigated as a new substrate material for LAPS and SPIM imaging. ITO is a heavily doped n-type semiconductor with a large bandgap of around 3.5 eV to 4.3 eV [334]. It is widely used as transparent conducting oxide because of its electrical conductivity, optical transparency and the ease to be deposited as films. In this work, a photocurrent of blank ITO could be excited by the UV part of a 405 nm diode laser that has been commonly used as a light source in LAPS. The mature ITO coated glass is cheap, robust, stable and easy to be modified, making it a suitable substrate for LAPS and SPIM imaging. It could significantly expand the application of LAPS imaging for general use. The photocurrent response, the pH response, LAPS and SPIM imaging and its lateral resolution using ITO coated glass without any modification were investigated in this work. Importantly, single cell imaging using LAPS based on ITO coated glass as the substrate was realized for the first time.

5.2 Experimental methods

5.2.1 Materials

Indium tin oxide (ITO) coated glass (50 Ω/cm^2) was purchased from Diamond Coatings Limited, UK. All chemicals were purchased form Sigma-Aldrich, including the cell culture materials of Dulbecco's Modified Eagle's Medium (DMEM), Fetal Bovine Serum (FBS), penicillin-streptomycin, Dulbecco's Phosphate Buffered Saline (DPBS, pH 7.4, 10 mM phosphate buffer solution containing 137 mM NaCl and 2.7 mM KCl) and

Trypsin-EDTA. All solutions were prepared using ultrapure water (18.2 MΩ·cm) from a Milli-Q water purification system (Millipore, USA). Osteoblasts MG63 (Human osteosarcoma cell line) were provided by Dr Karin Hing's group. Rat neuroblastoma B50 cells were obtained from Professor Gleb B. Sukhorukov's group and were originally purchased from Sigma-Aldrich.

5.2.2 Preparation of ITO coated glass

The ITO coated glass was cut into 1 cm × 1 cm pieces. They were cleaned by ultrasonication for 15 min with acetone, isopropanol, and ultrapure water. After drying with nitrogen, the ITO coated glass was kept at room temperature before use.

5.2.3 Cell culturing on ITO

Osteoblasts MG 63 and rat neuroblastoma B50 were cultured in a cell culture flask with DMEM supplemented with 10% FBS and 1% penicillin-streptomycin solution in a humidified atmosphere with 5% CO_2 at 37°C with the medium changed every two days. At confluence, cells were passaged by trypsinization and then maintained in the medium. Before seeding cells, ITO coated glass substrates and LAPS chamber were sterilized with 70% ethanol and rinsed thoroughly with sterilized water and sterilized DPBS solution and blown dry. Then cells were trypsinized in a 0.05% trypsin–EDTA solution and centrifuged at 1800 rpm for 5 min. After removing the supernatant, cells were dispersed in the cell culture medium described above. For single cell imaging with LAPS, cells were seeded onto the ITO coated glass surface in the assembled LAPS chamber at a concentration of $2.5x10^4$/mL and incubated at 37 °C with 5% CO_2 for 24 hours. Before LAPS measurement, the cell culture medium was replaced with DPBS.

5.2.4 Linear Sweep Voltammetry

Linear sweep voltammetry (LSV) was carried out in 10 mM PBS buffer pH 7.4 containing 137 mM NaCl and 2.7 mM KCl using an Autolab PGSTAT30/FRA2 (Windsor Scientific

Ltd, UK) using a platinum electrode and a Ag/AgCl electrode as the counter and reference electrodes, respectively. The scan rate was 5 mV/s. A diode laser (λ = 405 nm, max 500 mW) was used as the light source.

5.2.5 LAPS measurement

The LAPS setup has been shown in section 2.4. In this work, the substrate was ITO coated glass. The diode laser LD1539 (Laser 2000, λ = 405 nm, max 50 mW) was used for charge carrier generation. The modulation frequency was 10 Hz. A white light illuminated the sensor from the front side to obtain an optical image of the cells from the camera.

5.3 Results and discussion

5.3.1 The photocurrent response of ITO coated glass

The blank ITO coated glass showed an obvious photocurrent using LSV at anodic potentials with chopped 405 nm diode laser illumination (Figure 5.1a). Based on a bandgap of 4.3 eV to 3.5 eV, charge carriers in ITO should be excited at wavelengths below 288 nm to 354 nm, which indicated that charge carrier excitation was caused by the UV part of the wavelength distribution of the diode laser. This was also confirmed by a UV-Vis spectrum of the ITO coated glass (Figure 5.1b) which shows that the material is transparent to visible light and only absorbs light at wavelengths < 430 nm. Compared to a negligible background dark current, the photocurrent under illumination increased with the applied potential. An impedance spectrum of the ITO in PBS (Figure 5.1c and d) was dominated by a double layer capacitance of 13.2 μF/cm^2 over a large range of frequencies demonstrating the blocking nature of the ITO-solution interface in the dark. This provided the basis for using ITO coated glass as a substrate for LAPS and SPIM.

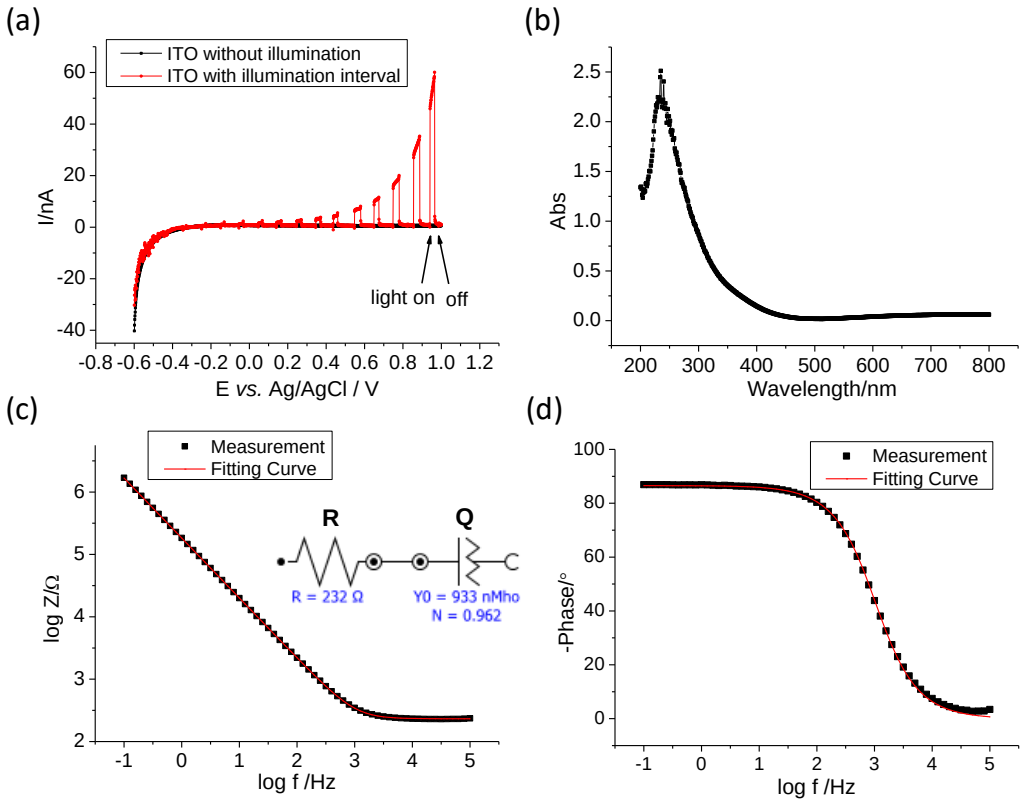

Figure 5.1 (a) LSV curves of ITO coated glass in the dark and with chopped illumination; (b)UV/Vis absorption spectra of ITO coated glass surface; Bode plots of (c) magnitude and (d) phase of ITO coated surface in 10 mM pH 7.4 PBS buffer at the open circuit potential in the dark. The equivalent circuit inset comprises a serial combination of the solution resistance (R) and a constant phase element (Q), which represents the double layer capacitance for a circular surface area with 3 mm diameter (13.2 μF/cm^2).

5.3.2 The pH response of ITO coated glass

LAPS has been developed for the detection of pH, ions, redox pairs and enzymatic reactions [335]. As the photocurrent-voltage (*I-V*) curve of LAPS responds to the surface potential, the pH could be monitored by a potential shift with a pH-sensitive layer, which has become a standard test. The *I-V* responses of ITO coated glass were measured in a series of pH phosphate buffer solutions (pH 4-9) with 0.1 M KCl using the LAPS setup shown in Figure 5.2. The ITO coated glass sensor showed an average pH sensitivity of 70 mV/pH at a constant photocurrent of 10 nA (Figure 5.2), making this a promising pH

imaging sensor that could be adapted for other biochemical analysis with LAPS. After measuring *I-V* curves in buffer solutions from pH 4 to 9 in sequence, the *I-V* curve returned to its initial positon when the pH was changed back to 4, showing good reversibility and stability of ITO coated glass for pH sensing. It is worth noting that the pH sensitivity of 70 mV/pH in this case is a non-Nernstian response. In contrast to traditional LAPS measurements where the semiconductor substrate is insulated, the ac photocurrent measured with blank ITO originates from the anodic photocurrent shown in Figure 5.1a, which is affected by the pH dependent kinetics of the photoelectrochemical oxidation reaction [146, 336].

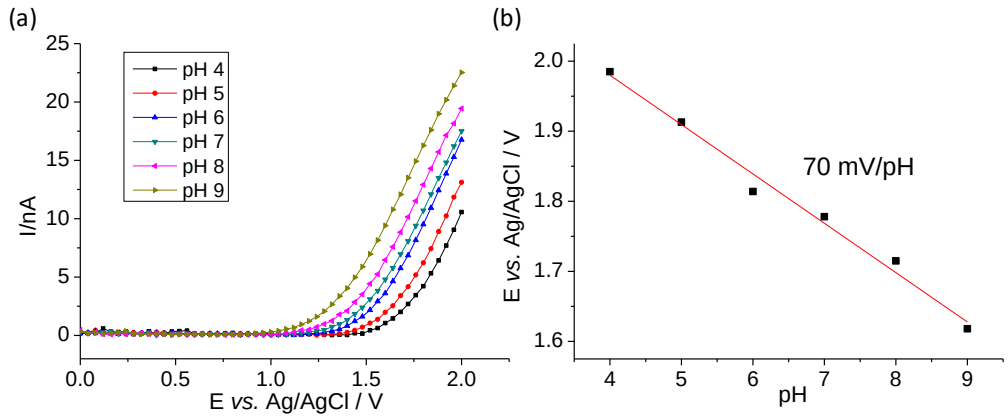

Figure 5.2 (a) LAPS I-V curves of ITO coated glass at different pH values; (b) the pH sensitivity of the ITO coated glass (R^2=0.98).

With such a high pH sensitivity (70 mV/pH), the ITO-based LAPS was applied to detect the cellular metabolism of a layer of osteoblasts by monitoring the photocurrent change caused by the pH change of the environment which was induced by metabolic products (carbon dioxide or lactic acid). In this experiment, osteoblasts were seeded on the sensor substrate at a concentration of $5x10^5$ /mL to keep a high density of cells attached on the sensor substrate (Figure 5.3a) following the same procedure described in section 5.2.3. A control substrate was prepared without any cells, but incubated with cell culture medium for 24 hours. For LAPS measurement, DPBS with 1 mM phosphate was used as the electrolyte solution and an unfocused blue laser was used as the light source illuminating

the entire measurement area. Figure 5.3c shows a series of *I-V* curves recorded before and after adding 40 µL 1 M glucose solution in the LAPS chamber which contained 4 mL electrolyte solution for 60 min with cells attached on the ITO coated glass surface. Figure 5.3d displays the voltage shift versus the time of before and after adding the glucose at a constant current value of 10 nA. At the time of 0 min, glucose was added to the electrolyte solution. Then the *I-V* curves continued shifting to the right which corresponded to a decreasing pH referring to the *I-V* curves shown in Figure 5.2a, due to the released acid product during the glycolysis. About 40 min after adding glucose, the *I-V* curves became stable, when the glycolysis reached a steady state. The maximum voltage shift was + 51 mV, corresponding to a pH change of 0.73 unit. However, the pH change of the DPBS with 1 mM phosphate electrolyte solution after adding the same amount of glucose for 1 hour with cells cultured in a petri dish was only 0.08 pH unit measured by pH meter. Thus it can be concluded that the pH change estimated from the LAPS measurement resulted from the change of the hydrogen ion concentration at the interface between the cells and the sensor surface, but not the pH change in the bulk electrolyte solution. For the control experiment, the *I-V* curves remained stable before and after adding glucose solution (Figure 5.3b). Thus, ITO-based LAPS was shown to be suitable detect the local pH change induced by cellular metabolism.

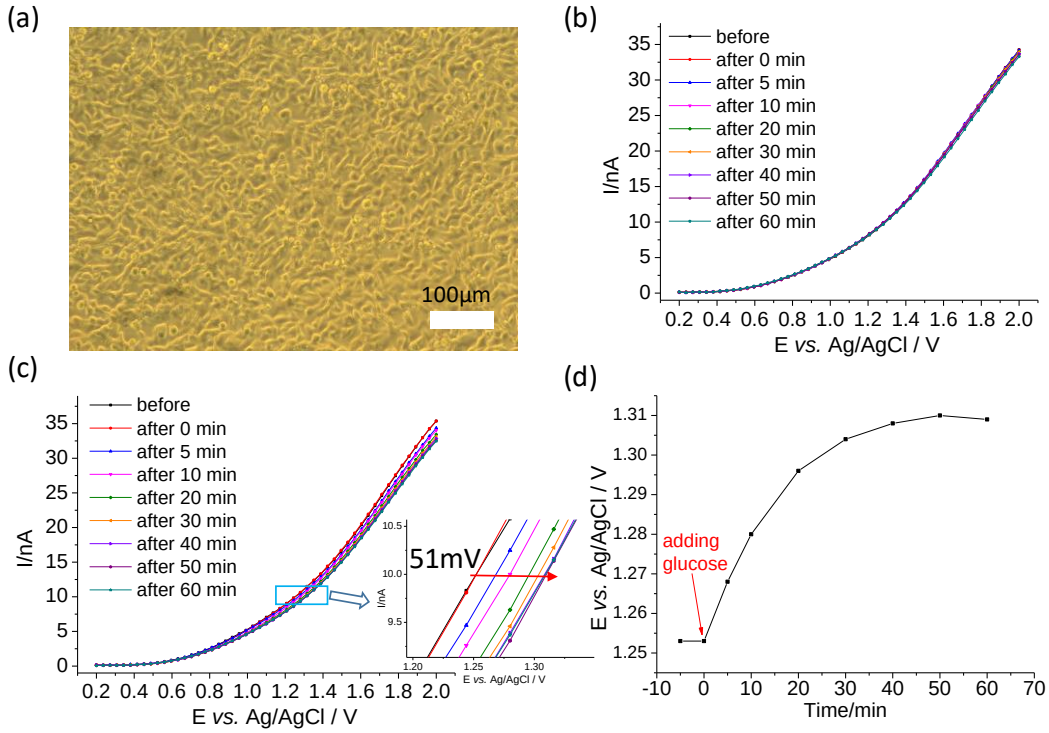

Figure 5.3 (a) optical image of an osteoblast monolayer cultured on ITO coated glass surface; (b) I-V curves on control sample (only cell culture medium incubated ITO coated glass substrate) before and after adding glucose solution for 60 min; (c) I-V curves on osteoblasts covered ITO coated glass substrate before and after adding glucose solution for 60 min and (d) corresponding voltage shift versus the time of before and after adding the glucose at a constant current value of 10 nA.

5.3.3 LAPS and SPIM imaging of ITO coated glass

Figure 5.4a shows the LAPS *I-V* characteristics of ITO coated glass with an unfocused laser source modulated at 10 Hz in pH 7.4 phosphate buffer. The ac photocurrent increased with the bias voltage and reached a plateau at about 2.3 V. At voltages greater than 2.5 V, the photocurrent dropped to zero because of the production of oxygen bubbles on the ITO surface at high positive potentials. In the following experiments, 2 V or an even lower voltage of 1.5 V was, therefore, chosen as the general measurement voltage.

To investigate the effect of the modulation frequency on the photocurrent, both the

photocurrent and background ac current under dark condition at 2 V were measured from 10 Hz to 10000 Hz. As shown in Figure 5.4b, the ac photocurrent decreased with increasing frequency while the dark current increased, which was caused by the background noise. The signal to noise ratio of the photocurrent decreased with increasing frequency. At frequencies greater than 10000 Hz the photocurrent could not be distinguished from the background dark current. 10 Hz was chosen as the measurement frequency in this work. To increase the measurement speed, higher frequencies up to 1000 Hz could also be used, albeit at the cost of a decreased signal to noise ratio and, therefore, somewhat reduced LAPS and SPIM imaging quality.

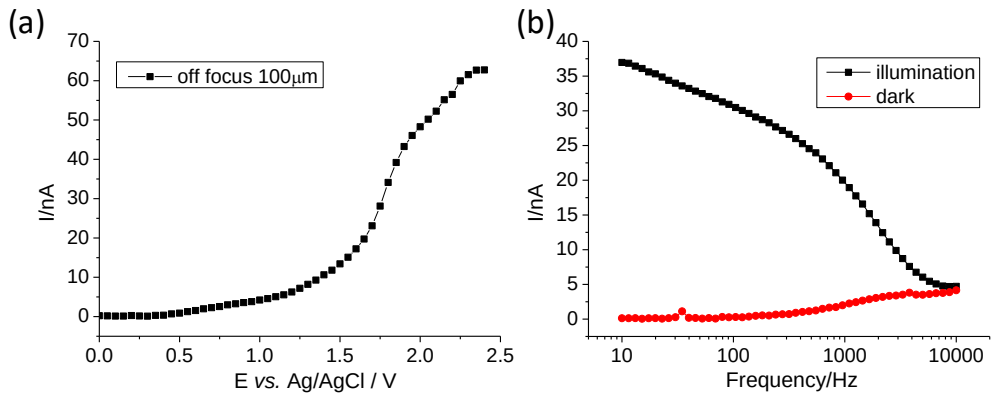

Figure 5.4 (a) LAPS I-V curve of blank ITO in pH 7.4 PBS buffer at 10 Hz with an unfocused laser source; (b) The frequency dependence of photocurrent and background AC current under dark condition.

To investigate the light-addressability of ITO coated glass, the blank ITO sample was used for photocurrent imaging. The modulated laser beam was focused through the glass substrate onto the ITO layer. A scan of the photocurrent with the distance of the sample from the microscope objective (z axis) was used to find the laser beam focus (Figure 5.5b). The photocurrent reached a minimum in focus as the amount of photo-generated carriers decreased with the decrease of the illuminated area when focusing. The focused spot diameter was about 1 μm. The LAPS *I-V* curve in focus showed similar but lower photocurrent response compared to the unfocused laser source (Figure 5.5c). A typical

100 × 100 pixel photocurrent image of a circular area of blank ITO sealed with a rubber O-ring is shown in Figure 5.5a.

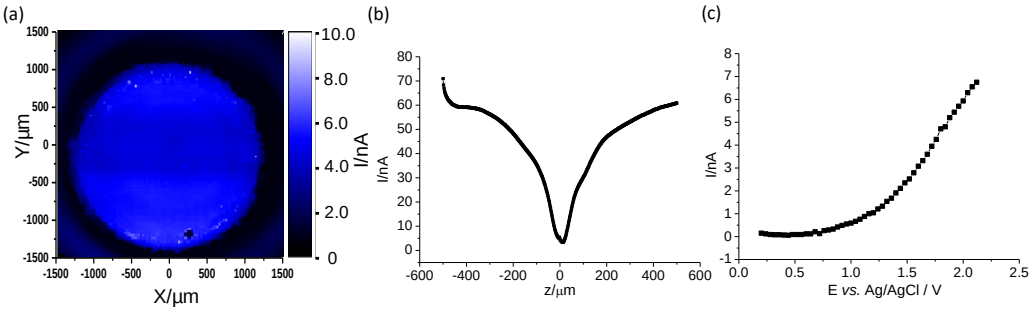

Figure 5.5 (a) The LAPS image of blank ITO at 2 V and 10 Hz with a focused laser beam; (b) z axis line scan of the photocurrent around the focus; (c) the LAPS I-V curve in focus at 10 Hz.

To characterize the lateral resolution, a poly (methyl methacrylate) (PMMA) dot was deposited from a 2% (w/v) polymer solution in anisole onto the ITO coated glass surface and allowed to dry. Figure 5.6a shows the SPIM area scan of the PMMA dot on the ITO coated glass surface measured at a bias voltage of 2 V and a modulation frequency of 10 Hz with a focused laser beam. The polymer dot is clearly visible as a reduction in photocurrent in the coated area. In the polymer dot covered area, the photocurrent decreased to nearly zero because of the high impedance of the PMMA dot. For lateral resolution measurements, a photocurrent line scan across the edge of polymer film was carried out with the focused laser beam and 1 μm step size (Figure 5.6b). The full width at half maximum (FWHM) value of the first derivative of the edge response is a typical indicator of the lateral resolution [21]. As shown in Figure 5.6c, the FWHM lateral resolution was about 2.3 μm, which is comparable to ultra-thin silicon on sapphire illuminated with a 405 nm blue laser, which showed a resolution of 1.5 μm [15]. The good lateral resolution can be attributed to the small thickness of the ITO coating in the order of hundreds of nanometers resulting in a small effective diffusion length of minority charge carriers and the high quality focus of the laser beam.

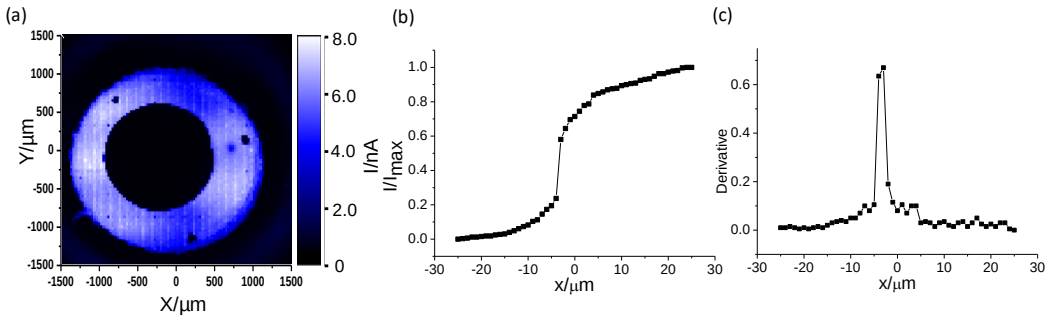

Figure 5.6 (a) The LAPS image of a PMMA dot at 2 V and 10 Hz with a focused laser beam; (b) x-axis photocurrent scan across the edge of the PMMA dot; (c) the first derivative of (b) with FWHM of 2.3 µm

To validate the surface potential imaging using ITO-based LAPS, a polycation of poly allylamine hydrochloride (PAH) dot was drop coated from a 20% (w/w) aqueous solution onto the ITO coated glass surface and allowed to dry. Figure 5.7a shows the LAPS images at 1.5 V with a modulation frequency of 10 Hz on the PAH dot coated ITO surfaces with a focused laser beam. At the selected voltage, an obvious white dot which corresponds to a greater photocurrent on the PAH dot than the blank ITO surface can be observed from the LAPS image shown in Figure 5.7a, which could be caused by a lower impedance or more positive charge of the PAH dot than the blank ITO surface. To verify this, electrochemical impedance measurements were carried out on an ITO sample before and after coating the 20% (w/w) PAH aqueous solution on the entire ITO surface. While the impedance spectra (Figure 5.7c) of ITO surfaces before and after PAH coating showed no difference at 1.5 V at a frequency of 10 Hz, which revealed the photocurrent difference between on the PAH dot and the blank ITO coated glass substrate was not resulting from the impedance but the surface charge. It is worth mentioning that there was a negative voltage shift of the *I-V* curves on the PAH dot compared to the blank ITO surface as displayed in Figure 5.7b, while the *I-V* curves of pH response shown in Figure 5.2a demonstrated a positive voltage shift for a lower pH value, which indicates a different response mechanism to traditional LAPS measurements. A possible explanation for this is that the positive surface potential introduced by the PAH increases the local potential

and enhances the anodic process on the electrode surface, while a decrease in pH decreases the local OH^- concentration thereby reducing the rate of the anodic process and causing a shift of the I-V curve in the opposite direction. Thus, the ITO-based LAPS was successfully applied to imaging surface potentials.

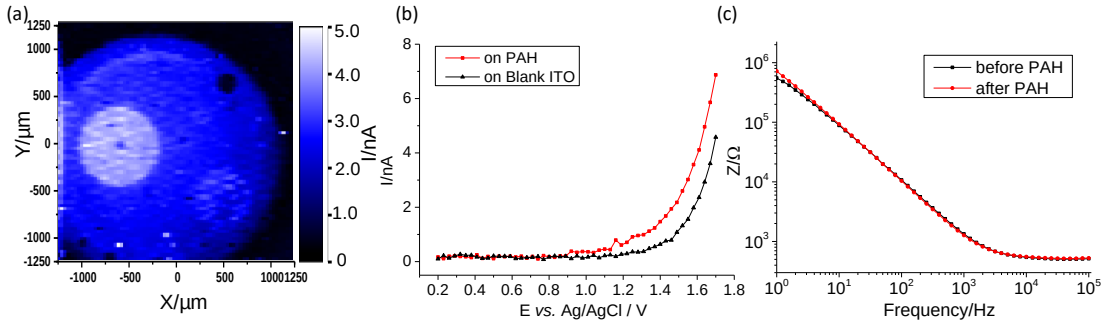

Figure 5.7 (a) LAPS image of ITO coated glass surface with a PAH dot at 1.5V with a frequency of 10Hz and (b) corresponding I-V curves on the PAH dot (red) and on the blank ITO (black); (c) Bode plots of ITO coated glass surface before (black) and after (red) coating with a complete PAH layer at 1.5V.

5.3.4 Cell imaging with LAPS and SPIM

Figure 5.8a showed the LAPS image of four osteoblasts on ITO coated glass surface at 1.5 V and a frequency of 10 Hz, which matched the optical image obtained from the camera (Figure 5.8e). The photocurrent on the cell was smaller than on the bare ITO surface, which could be caused by the negative charge of the cell surface or the impedance of the cell. While the impedance spectra (Figure 5.8f) of ITO surfaces before and after culturing a complete layer of osteoblasts (shown in Figure 5.3a) showed no difference at 1.5 V at the frequency of 10 Hz, which revealed that the photocurrent difference on the cell and off the cell was not due to the impedance but the negative surface charge of the cell. This charge effect-induced LAPS imaging of the cells on ITO coated glass surface was also confirmed by the LAPS image of the phase mode (Figure 5.8c) measured at 1.5 V and a frequency of 10 Hz, which was reported to be free from the variation of the maximum photocurrents obtained at the inversion voltage [12, 13]. The phase angle on

the cell was larger than on the blank ITO, also indicating the negative surface charge of the cells.

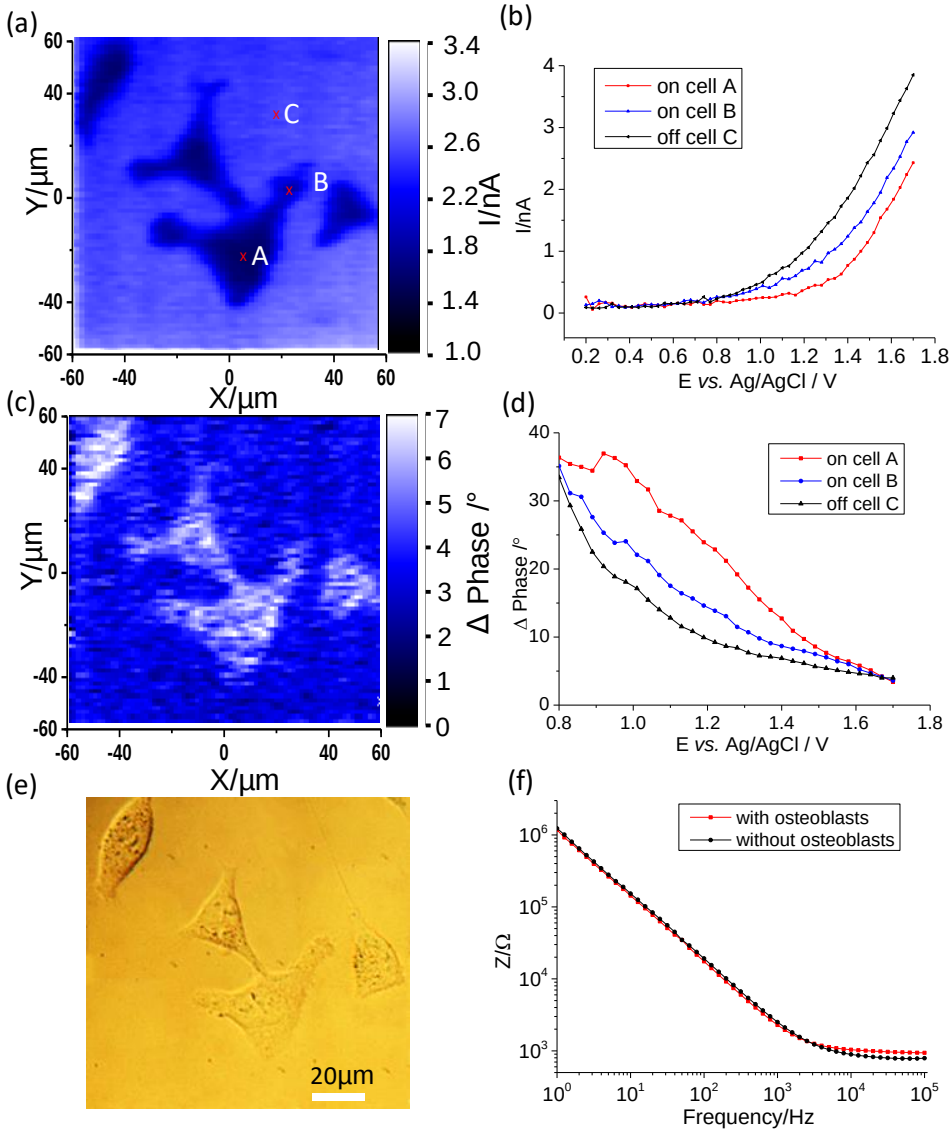

Figure 5.8 (a) LAPS image of osteoblasts on ITO coated glass surface at 1.5 V with a frequency of 10 Hz and corresponding (b) I-V curves on cell (point A red and B blue) and off cell C (black),(c) Δphase angle image,(d) Δphase angle-voltage curves, (e) optical image and (f) Bode plots of ITO coated glass surface at 1.5V before (black) and after (red) culturing a layer of osteoblasts.

It is also worth noting that the LAPS image of cells shown in Figure 5.8a presents a clear photocurrent distribution along the cells, where the photocurrent in the cell centre was

smaller than the photocurrent on the cell edge. *I-V* curves displayed in Figure 5.8b were measured at different points on a cell (points A and B) and off the cell (point C). There was a bigger positive voltage shift of *I-V* curves on point A than on point B compared to the *I-V* curve obtained on point C off the cell, which indicated a higher negative charge density in the cell centre than the cell edge, demonstrating that ITO-based LAPS was successfully applied to imaging the surface charge distribution of a single cell.

Besides imaging osteoblasts, rat neuroblastoma cells were also visualized with ITO-based LAPS. Figure 5.9a shows the LAPS image of three neurons attached on the ITO coated glass surface at 1.5 V and a frequency of 10 Hz, which matched the corresponding optical image in Figure 5.9c. There was an obvious photocurrent contrast on the neurons and on the blank ITO coated glass surface. Figure 5.9b shows the *I-V* curves on the cell centre point D and on the cell edge point E and off the cells point F. The value of the positive shift of *I-V* curve measured on point D in the cell centre compared to the *I-V* curve on point F off the cell was greater than that of the *I-V* curve on point E on the cell edge relative to the *I-V* curve on point F off the cell, which demonstrated more negative charge in the cell centre than the cell edge. The maximum voltage shift of *I-V* curves on the neuron compared to off the neuron is + 197 mV obtained from Figure 5.9b, which is slightly smaller than the maximum voltage shift of *I-V* curves (+ 218 mV) recorded on the osteoblast relative to off the osteoblast (see Figure 5.8b), indicating a higher negative charge density on the surface of osteoblasts than on the surface of neurons. It is important to note that there were some medium contaminants on the sensor substrate shown in the optical camera image (Figure 5.9c), while the LAPS image only showed the photocurrent signal from the neurons, further proving that the photocurrent signals were from cells.

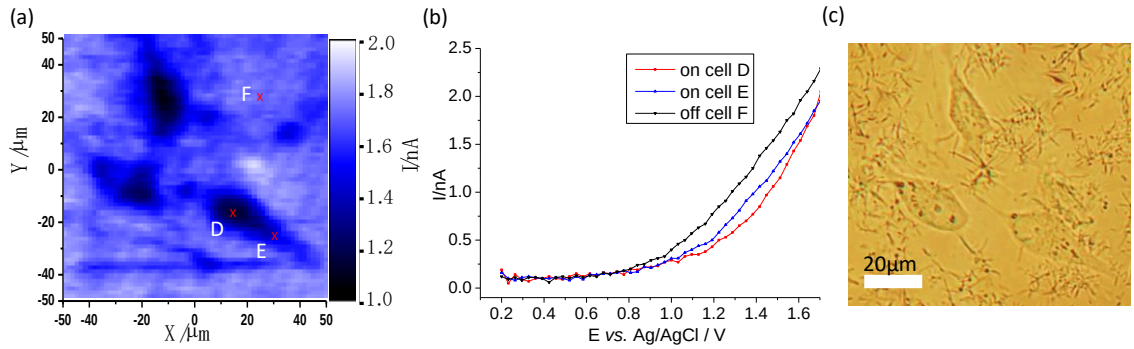

Figure 5.9 (a) LAPS image of neurons on ITO coated glass surface at 1.5V and a frequency of 10Hz and corresponding (b) I-V curves on cell (point D red and E blue) and off cell F (black) and (c) optical image.

5.4 Summary

ITO coated glass was tested as a substrate material for LAPS and SPIM imaging. It showed an obvious photocurrent when illuminated with a 405 nm diode laser. The unmodified ITO coated glass surface showed a repeatable pH response in LAPS measurements and was successfully applied to detect the pH change of cellular metabolism in the surface attachment area of the cells. Local photocurrents were produced by scanning a focused laser beam across the sample for LAPS and SPIM imaging. Good lateral resolution of 2.3 μm was obtained using a PMMA dot deposited on ITO as the model system. Surface potential imaging with the ITO-based LAPS was verified using a PAH dot patterned ITO surface. There was a negative shift of the *I-V* curves on the PAH dot compared to the blank ITO surface, which was opposite to the shift direction of *I-V* curve recorded for a lower pH, indicating a different response mechanism compared to traditional LAPS measurement. Herein, we conclude that the photocurrent of ITO-based LAPS is affected by the anodic oxidation process. The positive surface potential introduced by the PAH increases the local potential and enhances the anodic process on the electrode surface, while a decrease in pH decreases the local OH^- concentration thereby reducing the rate of the anodic process and causing a shift of the I-V curve in the opposite direction. Furthermore, surface charge imaging of a single cell was realized

using LAPS for the first time.

The mature, commercial ITO coating technology reduces the cost compared to previously used, expensive semiconductor substrates. The ITO coated glass does not need an extra insulating layer and an ohmic contact as ITO has good electrical conductivity, which further simplifies the application of ITO coated glass. This simple, low-cost and robust substrate material is therefore likely to make the LAPS and SPIM imaging technology attractive for widespread use as chemical sensors, biosensors and cell-based biosensors.

6. Conclusions

LAPS and SPIM based on different substrate materials were successfully employed to image organic monolayers and single cells in this work.

Initially, SOS substrates modified with 1,8-nonadiyne self-assembled organic monolayers, were used as sensor chips for LAPS and SPIM. The alkyne-terminated surfaces were further functionalized with an azido molecule (3-azido-1-propanamine) via a Cu(I)-catalyzed azide alkyne cycloaddition (CuAAC) 'click' reaction. A surface patterned with this azide was obtained by combining the CuAAC 'click' reaction with microcontact printing (μCP). In this work, it was established for the first time that alkyne-terminated surfaces modified with CuAAC 'click' reactions were contaminated with copper residues, which were not detectable by XPS, after the 'click' modified surfaces were rinsed with hydrochloride acid (HCl) solution, which has been frequently used to remove copper residues in the past. The copper residue was found and visualized with LAPS and SPIM, which showed negative voltage shifts of *I-V* curves and increases in the maximum photocurrent on the copper contaminated areas, corresponding to positive charges and decreased impedance induced by the copper contamination, respectively. Different strategies were then tested to avoid the copper contamination, including using stable, bulky copper(I) complex with a large counter ion to prevent the copper from entering the monolayer and rinsing the 'clicked' surface with different copper-removal solutions. The copper residue was completely removed by rinsing samples in a tetrasodium salt of ethylenediaminetetraacetic acid (EDTA) solution, the pH of which was adjusted to 7.4 with trifluoroacetic acid (TFA), after the 'click' reaction. The 'clicked' monolayer was then characterized with LAPS and SPIM, showing a negative voltage shift of *I-V* curves due to the positively charged amine groups and a decreased maximum photocurrent due to the increased impedance compared to the unreacted 1,8-nonadiyne surface, for the first time. It is envisaged that the high sensitivity of LAPS and SPIM to surface charges and impedance demonstrated in this study makes them promising techniques to measure the

electrical properties of biomolecules on surfaces.

Furthermore, the SOS substrate was functionalized with an RGD containing peptide, which was used to culture cells for the following electrochemical imaging of single cells using LAPS and SPIM. In this work, cyclic-RGDfK peptide was successfully immobilized on the SOS substrate by firstly modifying the cyclic-RGDfK peptide with an azido group by a linker molecule, 4-azidophenyl isothiocyanate (API), followed by a CuAAC 'click' reaction, which was validated by the water contact angle, ellipsometry and XPS results. The cell adhesion assay demonstrated that this RGD containing peptide enhanced the attachment of the cells on the substrate. An SOS surface patterned with the cyclic-RGDfK peptide was obtained by μCP combined with the CuAAC 'click' reaction, which was addressed for the first time. Then cell patterning was achieved by culturing cells on the cyclic-RGDfK peptide patterned SOS substrate, which in turn verified the success of the chemical patterning of cyclic-RGDfK peptide via μCP on SOS substrates. LAPS and SPIM imaging of single cells using this cyclic-RGDfK peptide modified SOS substrate and a two-photon effect for charge carrier generation was attempted. However, no photocurrent contrast was observed on and off cells in both LAPS and SPIM images, which was attributed to the poor sensitivity of the present LAPS and SPIM system to single cells surface charge and impedance.

To solve the aforementioned problem, an alternative semiconductor material of ITO coated glass was proposed and investigated as a new substrate material for LAPS and SPIM imaging for the first time. An obvious photocurrent was observed when the ITO coated glass substrate was illuminated with a 405 nm diode laser. The unmodified ITO coated glass surface showed a repeatable pH response in LAPS measurements and was successfully applied to detect the pH change of cellular metabolism in the surface attachment area of the cells. Local photocurrents were produced by scanning a focused laser beam across the sample for LAPS and SPIM imaging. Good lateral resolution of 2.3 μm was obtained using a poly(methyl methacrylate) (PMMA) dot deposited on ITO

as the model system.

Surface potential imaging with the ITO-based LAPS was verified using a polycation of poly allylamine hydrochloride (PAH) dot patterned ITO surface. It was found that introducing a positive surface charge with PAH and a decrease in pH caused the *I-V* curves to shift in opposite directions, indicating a different response mechanism compared to traditional LAPS measurement. It was therefore concluded that the photocurrent of ITO-based LAPS was affected by the anodic oxidation process. The positive surface potential introduced by the PAH increased the local potential and enhanced the anodic process on the electrode surface, while a decrease in pH decreased the local OH^- concentration thereby reducing the rate of the anodic process and causing a shift of the *I-V* curve in the opposite direction. Furthermore, surface charge imaging of single cells was realized using this ITO-based LAPS system for the first time. Two types of cells including osteoblasts and rat neuroblastoma cells were tested. LAPS images showed negative surface charges, and a charge distribution of a higher charge density on the cell centre compared to the cell edge, for both types of cells.

7. Future work

To continue this project, there remains a lot of work to do. The cyclic-RGDfK peptide modified SOS substrates used for LAPS measurement could be adapted for measuring the release of metabolites such as H^+ from single cells by adding some glucose to the electrolyte solution, even though the electrical parameters such as impedance and surface charge of single cells could not be detected. In terms of the cellular patterns achieved in chapter 4, there were still some cells adhering on areas off the cyclic-RGDfK modified islands. To fully control the cell attachment only in the patterned area, a cytophobic molecule of poly(ethylene glycol) can be immobilized on the off-pattern area to block the cell attachment.

Although single cells electrochemical imaging using LAPS has been achieved with ITO, there remain some problems to be solved. For example, the mechanism of using ITO-based LAPS to image the surface charge of single cells is still not understood thoroughly, since the measurement was carried out using an electrolyte solution with high-ionic strength (~150 mM), and under this condition the Debye length was depressed to less than 1 nm. Another issue is that the impedance of single cells has not been detected by SPIM using the same system. Since the impedance of cells on substrates is usually considered to be a measure of cell adhesion on a substrate, modifying the ITO substrate with cytophilic proteins or the RGD containing peptide to improve cell adhesion would be an option to realize the impedance imaging of single cells. The stability of the ITO coated glass substrate under the illumination of a focused light with a bias voltage was also a problem, which could be caused by the hole accumulation at the surface of ITO, which induced composition changes in ITO. This photodegradation problem of ITO might be solved by modifying ITO surface with redox agents.

Despite the existing problems, using LAPS to image single cells is a novel electrochemical imaging method, which can be further applied for the investigation of the metabolic processes of single cells, the differentiation or proliferation of cells on different

types of surfaces to aid the development of tissue engineering materials and for the high-throughput screening of drug induced cell responses, and as a diagnostic tool to distinguish healthy and diseased cells.

8. References

[1] K. Nienhaus, G.U. Nienhaus, Fluorescent Proteins for Live-Cell Imaging with Super-Resolution, Chemical Society Reviews, 43(2014) 1088-106.

[2] S.A. Jones, S.H. Shim, J. He, X.W. Zhuang, Fast, Three-Dimensional Super-Resolution Imaging of Live Cells, Nature Methods, 8(2011) 499-U96.

[3] J. Wang, I. Campos, F. Wu, J.Y. Zhu, G.B. Sukhorukov, M. Palma*, et al.*, The Effect of Gold Nanoparticles on the Impedance of Microcapsules Visualized by Scanning Photo-Induced Impedance Microscopy, Electrochimica Acta, 208(2016) 39-46.

[4] J. Wang, Y.L. Zhou, M. Watkinson, J. Gautrot, S. Krause, High-Sensitivity Light-Addressable Potentiometric Sensors Using Silicon on Sapphire Functionalized with Self-Assembled Organic Monolayers, Sensors And Actuators B-Chemical, 209(2015) 230-6.

[5] D.G. Hafeman, J.W. Parce, H.M. McConnell, Light-Addressable Potentiometric Sensor for Biochemical Systems, Science, 240(1988) 1182-5.

[6] M. Nakao, T. Yoshinobu, H. Iwasaki, Scanning-Laser-Beam Semiconductor pH-Imaging Sensor, Sensors And Actuators B-Chemical, 20(1994) 119-23.

[7] C.F. Werner, C. Krumbe, K. Schumacher, S. Groebel, H. Spelthahn, M. Stellberg*, et al.*, Determination of the Extracellular Acidification of Escherichia Coli by a Light-Addressable Potentiometric Sensor, physica status solidi (a), 208(2011) 1340-4.

[8] C.S. Wu, A. Poghossian, T.S. Bronder, M.J. Schoning, Sensing of Double-Stranded DNA Molecules by Their Intrinsic Molecular Charge Using the Light-Addressable Potentiometric Sensor, Sensors And Actuators B-Chemical, 229(2016) 506-12.

[9] D.-W. Zhang, F. Wu, J. Wang, M. Watkinson, S. Krause, Image Detection of Yeast Saccharomyces Cerevisiae by Light-Addressable Potentiometric Sensors (LAPS), Electrochemistry Communications, 72(2016) 41-5.

[10] B. Stein, M. George, H.E. Gaub, W.J. Parak, Extracellular Measurements of Averaged Ionic Currents with the Light-Addressable Potentiometric Sensor (LAPS), Sensors And Actuators B-Chemical, 98(2004) 299-304.

[11] S. Krause, W. Moritz, H. Talabani, M. Xu, A. Sabot, G. Ensell, Scanning Photo-Induced Impedance Microscopy—Resolution Studies and Polymer Characterization, Electrochimica Acta, 51(2006) 1423-30.

[12] K.-i. Miyamoto, T. Wagner, S. Mimura, S.i. Kanoh, T. Yoshinobu, M.J. Schöning, Constant-Phase-Mode Operation of the Light-Addressable Potentiometric Sensor, Sensors and Actuators B: Chemical, 154(2011) 119-23.

[13] K.-i. Miyamoto, T. Wagner, T. Yoshinobu, S.i. Kanoh, M.J. Schöning, Phase-Mode LAPS and Its Application to Chemical Imaging, Sensors and Actuators B: Chemical, 154(2011) 28-32.

[14] K.-i. Miyamoto, T. Wagner, S. Mimura, S.i. Kanoh, T. Yoshinobu, M.J. Schöning, Constant-Phase-Mode Operation of the Light-Addressable Potentiometric Sensor, Procedia Chemistry, 1(2009) 1487-90.

[15] L. Chen, Y. Zhou, S. Jiang, J. Kunze, P. Schmuki, S. Krause, High Resolution LAPS and SPIM, Electrochemistry Communications, 12(2010) 758-60.

[16] Y. Ito, High-Spatial Resolution LAPS, Sensors And Actuators B-Chemical, 52(1998) 107-11.

[17] W. Moritz, T. Yoshinobu, F. Finger, S. Krause, M. Martin-Fernandez, M.J. Schöning, High Resolution LAPS Using Amorphous Silicon as the Semiconductor Material, Sensors and Actuators B: Chemical,

103(2004) 436-41.
[18] W.J. Parak, M. George, J. Domke, M. Radmacher, J.C. Behrends, M.C. Denyer*, et al.*, Can the Light-Addressable Potentiometric Sensor (LAPS) Detect Extracellular Potentials of Cardiac Myocytes?, IEEE Transactions on Biomedical Engineering, 47(2000) 1106-13.
[19] Y. Guo, K.-i. Miyamoto, T. Wagner, M.J. Schöning, T. Yoshinobu, Device Simulation of the Light-Addressable Potentiometric Sensor for the Investigation of the Spatial Resolution, Sensors and Actuators B: Chemical, 204(2014) 659-65.
[20] Q. Zhang, Theoretical Analysis and Design of Submicron-LAPS, Sensors and Actuators B: Chemical, 105(2005) 304-11.
[21] M. George, W.J. Parak, I. Gerhardt, W. Moritz, F. Kaesen, H. Geiger*, et al.*, Investigation of the Spatial Resolution of the Light-Addressable Potentiometric Sensor, Sensors And Actuators a-Physical, 86(2000) 187-96.
[22] W. Moritz, I. Gerhardt, D. Roden, M. Xu, S. Krause, Photocurrent Measurements for Laterally Resolved Interface Characterization, Fresenius Journal Of Analytical Chemistry, 367(2000) 329-33.
[23] A. Das, A. Das, L.B. Chang, C.S. Lai, R.M. Lin, F.C. Chu*, et al.*, GaN Thin Film Based Light Addressable Potentiometric Sensor for pH Sensing Application, Applied Physics Express, 6(2013).
[24] A. Das, Y.-H. Lin, C.-S. Lai, Miniaturized Amorphous-Silicon Based Chemical Imaging Sensor System Using a Mini-Projector as a Simplified Light-Addressable Scanning Source, Sensors and Actuators B: Chemical, 190(2014) 664-72.
[25] T. Yoshinobu, M.J. Schoning, F. Finger, W. Moritz, H. Iwasaki, Fabrication of Thin-Film LAPS with Amorphous Silicon, Sensors, 4(2004) 163-9.
[26] J.C. van den Heuvel, R.C. van Oort, M.J. Geerts, Diffusion Length Measurements of Thin Amorphous Silicon Layers, Solid State Communications, 69(1989) 807-10.
[27] Y. Zhou, L. Chen, S. Krause, J.-N. Chazalviel, Scanning Photoinduced Impedance Microscopy Using Amorphous Silicon Photodiode Structures, Analytical Chemistry, 79(2007) 6208-14.
[28] Y. Zhou, S. Jiang, S. Krause, J.-N. Chazalviel, Biosensor Arrays Based on the Degradation of Thin Polymer Films Interrogated by Scanning Photoinduced Impedance Microscopy, Analytical Chemistry, 79(2007) 8974-8.
[29] M. Nakao, S. Inoue, T. Yoshinobu, H. Iwasaki, High-Resolution pH Imaging Sensor for Microscopic Observation of Microorganisms, Sensors And Actuators B-Chemical, 34(1996) 234-9.
[30] M. Nakao, T. Yoshinobu, H. Iwasaki, Improvement of Spatial-Resolution of a Laser-Scanning pH-Imaging Sensor, Japanese Journal Of Applied Physics Part 2-Letters, 33(1994) L394-L7.
[31] W.J. Parak, U.G. Hofmann, H.E. Gaub, J.C. Owicki, Lateral Resolution of Light-Addressable Potentiometric Sensors: An Experimental and Theoretical Investigation, Sensors And Actuators a-Physical, 63(1997) 47-57.
[32] Y. Guo, K. Seki, K.-i. Miyamoto, T. Wagner, M.J. Schöning, T. Yoshinobu, Device Simulation of the Light-Addressable Potentiometric Sensor with a Novel Photoexcitation Method for a Higher Spatial Resolution, Procedia Engineering, 87(2014) 456-9.
[33] K. Miyamoto, K. Seki, Y. Guo, T. Wagner, M.J. Schöning, T. Yoshinobu, Enhancement of the Spatial Resolution of the Chemical Imaging Sensor by a Hybrid Fiber-Optic Illumination, Procedia Engineering, 87(2014) 612-5.
[34] A. Das, T.-C. Chen, C.-M. Yang, C.-S. Lai, A High-Speed, Flexible-Scanning Chemical Imaging System

Using a Light-Addressable Potentiometric Sensor Integrated with an Analog Micromirror, Sensors and Actuators B: Chemical, 198(2014) 225-32.
[35] A. Das, C.-M. Yang, T.-C. Chen, C.-S. Lai, Analog Micromirror-LAPS for Chemical Imaging and Zoom-in Application, Vacuum, 118(2015) 161-6.
[36] T. Wagner, K. Miyamoto, C.F. Werner, M.J. Schoning, T. Yoshinobu, Utilising Digital Micro-Mirror Device (DMD) as Scanning Light Source for Light-Addressable Potentiometric Sensors (LAPS), Sensor Letters, 9(2011) 812-5.
[37] Y.H. Lin, A. Das, C.S. Lai, A Simple and Convenient Set-up of Light Addressable Potentiometric Sensors (LAPS) for Chemical Imaging Using a Commercially Available Projector as a Light Source, International Journal Of Electrochemical Science, 8(2013) 7062-74.
[38] K.-i. Miyamoto, K. Kaneko, A. Matsuo, T. Wagner, S.i. Kanoh, M.J. Schöning*, et al.*, Miniaturized Chemical Imaging Sensor System Using an OLED Display Panel, Sensors and Actuators B: Chemical, 170(2012) 82-7.
[39] T. Wagner, C.F. Werner, K.-i. Miyamoto, M.J. Schöning, T. Yoshinobu, Development and Characterisation of a Compact Light-Addressable Potentiometric Sensor (LAPS) Based on the Digital Light Processing (DLP) Technology for Flexible Chemical Imaging, Sensors and Actuators B: Chemical, 170(2012) 34-9.
[40] C.F. Werner, T. Wagner, K.-i. Miyamoto, T. Yoshinobu, M.J. Schöning, High Speed and High Resolution Chemical Imaging Based on a New Type of OLED-LAPS Set-Up, Sensors and Actuators B: Chemical, 175(2012) 118-22.
[41] Q. Zhang, P. Wang, W.J. Parak, M. George, G. Zhang, A Novel Design of Multi-Light LAPS Based on Digital Compensation of Frequency Domain, Sensors and Actuators B: Chemical, 73(2001) 152-6.
[42] T. Wagner, R. Molina, T. Yoshinobu, J.P. Kloock, M. Biselli, M. Canzoneri*, et al.*, Handheld Multi-Channel LAPS Device as a Transducer Platform for Possible Biological and Chemical Multi-Sensor Applications, Electrochimica Acta, 53(2007) 305-11.
[43] K. Miyamoto, Y. Kuwabara, S.i. Kanoh, T. Yoshinobu, T. Wagner, M.J. Schöning, Chemical Image Scanner Based on Fdm-LAPS, Sensors and Actuators B: Chemical, 137(2009) 533-8.
[44] T. Wagner, C.F.B. Werner, K.-I. Miyamoto, M.J. Schöning, T. Yoshinobu, A High-Density Multi-Point LAPS Set-up Using a VCSEL Array and FPGA Control, Sensors and Actuators B: Chemical, 154(2011) 124-8.
[45] K. Miyamoto, A. Itabashi, T. Wagner, M.J. Schoning, T. Yoshinobu, High-Speed Chemical Imaging inside a Microfluidic Channel, Sensors And Actuators B-Chemical, 194(2014) 521-7.
[46] A. Seki, K. Motoya, S. Watanabe, I. Kubo, Novel Sensors for Potassium, Calcium and Magnesium Ions Based on a Silicon Transducer as a Light-Addressable Potentiometric Sensor, Analytica Chimica Acta, 382(1999) 131-6.
[47] Y. Mourzina, T. Yoshinobu, J. Schubert, H. Lüth, H. Iwasaki, M.J. Schöning, Ion-Selective Light-Addressable Potentiometric Sensor (LAPS) with Chalcogenide Thin Film Prepared by Pulsed Laser Deposition, Sensors and Actuators B: Chemical, 80(2001) 136-40.
[48] Y. Ermolenko, T. Yoshinobu, Y. Mourzina, K. Furuichi, S. Levichev, Y. Vlasov*, et al.*, Lithium Sensor Based on the Laser Scanning Semiconductor Transducer, Analytica Chimica Acta, 459(2002) 1-9.
[49] C.H. Chin, T.F. Lu, J.C. Wang, J.H. Yang, C.E. Lue, C.M. Yang*, et al.*, Effects of Cf4 Plasma Treatment on pH and PNA Sensing Properties of Light-Addressable Potentiometric Sensor with a 2-nm-Thick Sensitive HfO_2 Layer Grown by Atomic Layer Deposition, Japanese Journal Of Applied Physics, 50(2011).

[50] Y. Ermolenko, T. Yoshinobu, Y. Mourzina, S. Levichev, K. Furuichi, Y. Vlasov*, et al.*, Photocurable Membranes for Ion-Selective Light-Addressable Potentiometric Sensor, Sensors and Actuators B: Chemical, 85(2002) 79-85.
[51] H. Men, S.F. Zou, A. Legin, P. Wang, A Novel Mercury Ion Selective Thin Film Sensor, Chinese Journal Of Analytical Chemistry, 33(2005) 428-31.
[52] H. Men, S. Zou, Y. Li, Y. Wang, X. Ye, P. Wang, A Novel Electronic Tongue Combined MLAPS with Stripping Voltammetry for Environmental Detection, Sensors and Actuators B: Chemical, 110(2005) 350-7.
[53] W. Hu, H. Cai, J. Fu, P. Wang, G. Yang, Line-Scanning LAPS Array for Measurement of Heavy Metal Ions with Micro-Lens Array Based on Mems, Sensors And Actuators B-Chemical, 129(2008) 397-403.
[54] J.P. Kloock, L. Moreno, A. Bratov, S. Huachupoma, J. Xu, T. Wagner*, et al.*, PLD-Prepared Cadmium Sensors Based on Chalcogenide Glasses—ISFET, LAPS and Mise Semiconductor Structures, Sensors and Actuators B: Chemical, 118(2006) 149-55.
[55] A.B.M. Ismail, K. Furuichi, T. Yoshinobu, H. Iwasaki, Light-Addressable Potentiometric Fluoride (F^-) Sensor, Sensors and Actuators B: Chemical, 86(2002) 94-7.
[56] J.-C. Wang, Y.-R. Ye, Y.-H. Lin, Light-Addressable Potentiometric Sensor with Nitrogen-Incorporated Ceramic SM_2O_3 Membrane for Chloride Ions Detection, Journal of the American Ceramic Society, 98(2015) 443-7.
[57] Y.G. Mourzina, Y.E. Ermolenko, T. Yoshinobu, Y. Vlasov, H. Iwasaki, M.J. Schoning, Anion-Selective Light-Addressable Potentiometric Sensors (LAPS) for the Determination of Nitrate and Sulphate Ions, Sensors And Actuators B-Chemical, 91(2003) 32-8.
[58] M. Adami, M. Martini, L. Piras, Characterization and Enzymatic Application of a Redox Potential Biosensor Based on a Silicon Transducer, Biosensors & Bioelectronics, 10(1995) 633-8.
[59] N. Oba, T. Yoshinobu, H. Iwasaki, Redox Potential Imaging Sensor, Japanese Journal Of Applied Physics Part 2-Letters, 35(1996) L460-L3.
[60] M. Adami, L. Piras, M. Lanzi, A. Fanigliulo, S. Vakula, C. Nicoli, Monitoring of Enzymatic Activity and Quantitative Measurements of Substrates by Means of a Newly Designed Silicon-Based Potentiometric Sensor, Sensors and Actuators B: Chemical, 18(1994) 178-82.
[61] I.G. Mourzina, T. Yoshinobu, Y.E. Ermolenko, Y.G. Vlasov, M.J. Schoning, H. Iwasaki, Immobilization of Urease and Cholinesterase on the Surface of Semiconductor Transducer for the Development of Light-Addressable Potentiometric Sensors, Microchimica Acta, 144(2004) 41-50.
[62] K.R. Rogers, M. Foley, S. Alter, P. Koga, M. Eldefrawi, Light Addressable Potentiometric Biosensor for the Detection of Anticholinesterases, Analytical Letters, 24(1991) 191-8.
[63] M.S. Dehlawi, A.T. Eldefrawi, M.E. Eldefrawi, N.A. Anis, J.J. Valdes, Choline Derivatives and Sodium Fluoride Protect Acetylcholinesterase against Irreversible Inhibition and Aging by Dfp and Paraoxon, Journal of Biochemical Toxicology, 9(1994) 261-8.
[64] J.C. Fernando, K.R. Rogers, N.A. Anis, J.J. Valdes, R.G. Thompson, A.T. Eldefrawi*, et al.*, Rapid Detection of Anticholinesterase Insecticides by a Reusable Light Addressable Potentiometric Biosensor, Journal Of Agricultural And Food Chemistry, 41(1993) 511-6.
[65] M. Adami, M. Sartore, C. Nicolini, Pab: A Newly Designed Potentiometric Alternating Biosensor System, Biosensors and Bioelectronics, 10(1995) 155-67.
[66] A. Seki, S.-i. Ikeda, I. Kubo, I. Karube, Biosensors Based on Light-Addressable Potentiometric Sensors for Urea, Penicillin and Glucose, Analytica Chimica Acta, 373(1998) 9-13.

[67] J.R. Siqueira, C.F. Werner, M. Bäcker, A. Poghossian, V. Zucolotto, O.N. Oliveira*, et al.*, Layer-by-Layer Assembly of Carbon Nanotubes Incorporated in Light-Addressable Potentiometric Sensors, The Journal of Physical Chemistry C, 113(2009) 14765-70.
[68] J.R. Siqueira Jr., M. Bäcker, A. Poghossian, V. Zucolotto, O.N. Oliveira Jr., M.J. Schöning, Associating Biosensing Properties with the Morphological Structure of Multilayers Containing Carbon Nanotubes on Field-Effect Devices, Physica status solidi A, Applications and materials science, 207(2010) 781-6.
[69] E.G. Kondrat'eva, T.A. Osipova, V.I. Sklyar, A.N. Reshetilov, Biosensors Based on a Light-Addressable Potentiometric Sensor (LAPS) for Analysis in Both Aqueous Solutions and Organic Solvents, Applied Biochemistry and Biotechnology, 88(2000) 335-44.
[70] K. Aoki, H. Uchida, T. Katsube, Y. Ishimaru, T. Iida, Integration of Bienzymatic Disaccharide Sensors for Simultaneous Determination of Disaccharides by Means of Light Addressable Potentiometric Sensor, Analytica Chimica Acta, 471(2002) 3-12.
[71] K.A. Uithoven, J.C. Schmidt, M.E. Ballman, Rapid Identification of Biological Warfare Agents Using an Instrument Employing a Light Addressable Potentiometric Sensor and a Flow-through Immunofiltration-Enzyme Assay System, Biosensors & Bioelectronics, 14(2000) 761-70.
[72] W.M. Hurni, W.J. Miller, R.F. Zuk, V.T. Kung, Detection of Antibody to the Pres2 Sequence of the Hepatitis B Virus Envelope Protein Using an Immuno-Ligand Assay with a Silicon Sensor Detection System, Journal of Immunological Methods, 145(1991) 19-26.
[73] K. Dill, J.D. Olson, Picogram Detection Levels of Asialofetuin Via the Carbohydrate Moieties Using the Light Addressable Potentiometric Sensor, Glycoconjugate Journal, 12(1995) 660-3.
[74] K. Dill, C. Fraser, J.A. Blomdahl, J.D. Olson, Determination of Dissociation Constant and Concentration of an Anti-DNA Antibody by Using the Light-Addressable Potentiometric Sensor, Journal Of Biochemical And Biophysical Methods, 31(1996) 17-21.
[75] K. Dill, S.D.H. Chan, T.W. Gibbs, Detection of Plasmids Using DNA and Rna Probes and the Light-Addressable Potentiometric Sensor, Journal Of Biochemical And Biophysical Methods, 35(1997) 197-202.
[76] W.E. Lee, H.G. Thompson, J.G. Hall, R.E. Fulton, J.P. Wong, Rapid Immunofiltration Assay of Newcastle Disease Virus Using a Silicon Sensor, Journal of Immunological Methods, 166(1993) 123-31.
[77] W.-G. Hu, H.G. Thompson, A.Z. Alvi, L.P. Nagata, M.R. Suresh, R.E. Fulton, Development of Immunofiltration Assay by Light Addressable Potentiometric Sensor with Genetically Biotinylated Recombinant Antibody for Rapid Identification of Venezuelan Equine Encephalitis Virus, Journal of Immunological Methods, 289(2004) 27-35.
[78] K. Dill, J.H. Song, J.A. Blomdahl, J. D. Olson, Rapid, Sensitive and Specific Detection of Whole Cells and Spores Using the Light-Addressable Potentiometric Sensor, Journal of Biochemical and Biophysical Methods, 34(1997) 161-6.
[79] A.G. Gehring, D.L. Patterson, S.-I. Tu, Use of a Light-Addressable Potentiometric Sensor for the Detection Ofescherichia Colio157:H7, Analytical Biochemistry, 258(1998) 293-8.
[80] C. Ercole, M.D. Gallo, M. Pantalone, S. Santucci, L. Mosiello, C. Laconi*, et al.*, A Biosensor for Escherichia Coli Based on a Potentiometric Alternating Biosensing (Pab) Transducer, Sensors and Actuators B: Chemical, 83(2002) 48-52.
[81] C. Ercole, M. Del Gallo, L. Mosiello, S. Baccella, A. Lepidi, Escherichia Coli Detection in Vegetable Food by a Potentiometric Biosensor, Sensors And Actuators B-Chemical, 91(2003) 163-8.
[82] K. Dill, L.H. Stanker, C.R. Young, Detection of Salmonella in Poultry Using a Silicon Chip-Based Biosensor,

Journal Of Biochemical And Biophysical Methods, 41(1999) 61-7.
[83] L. Mosiello, C. Laconi, M. Del Gallo, C. Ercole, A. Lepidi, Development of a Monoclonal Antibody Based Potentiometric Biosensor for Terbuthylazine Detection, Sensors And Actuators B-Chemical, 95(2003) 315-20.
[84] L. Piras, M. Adami, S. Fenu, M. Dovis, C. Nicolini, Immunoenzymatic Application of a Redox Potential Biosensor, Analytica Chimica Acta, 335(1996) 127-35.
[85] B. Stein, M. George, H.E. Gaub, J.C. Behrends, W.J. Parak, Spatially Resolved Monitoring of Cellular Metabolic Activity with a Semiconductor-Based Biosensor, Biosensors & Bioelectronics, 18(2003) 31-41.
[86] L.H. Bruner, K.R. Miller, J.C. Owicki, J.W. Parce, V.C. Muir, Testing Ocular Irritancy Invitro with the Silicon Microphysiometer, Toxicology In Vitro, 5(1991) 277-84.
[87] P. Gavazzo, S. Paddeu, M. Sartore, C. Nicolini, Study of the Relationship between Extracellular Acidification and Cell Viability by a Silicon-Based Sensor, Sensors And Actuators B-Chemical, 19(1994) 368-72.
[88] H. Yu, H. Cai, W. Zhang, L. Xiao, Q. Liu, P. Wang, A Novel Design of Multifunctional Integrated Cell-Based Biosensors for Simultaneously Detecting Cell Acidification and Extracellular Potential, Biosensors and Bioelectronics, 24(2009) 1462-8.
[89] P.M. Shaibani, K. Jiang, G. Haghighat, M. Hassanpourfard, H. Etayash, S. Naicker*, et al.*, The Detection of Escherichia Coli (E. Coli) with the pH Sensitive Hydrogel Nanofiber-Light Addressable Potentiometric Sensor (Nf-LAPS), Sensors and Actuators B: Chemical, 226(2016) 176-83.
[90] J.W. Parce, J.C. Owicki, K.M. Kercso, Biosensors for Directly Measuring Cell Affecting Agents, Annales De Biologie Clinique, 48(1990) 639-41.
[91] Q. Liu, N. Hu, F. Zhang, H. Wang, W. Ye, P. Wang, Neurosecretory Cell-Based Biosensor: Monitoring Secretion of Adrenal Chromaffin Cells by Local Extracellular Acidification Using Light-Addressable Potentiometric Sensor, Biosensors and Bioelectronics, 35(2012) 421-4.
[92] N. Hu, J. Zhou, K. Su, D. Zhang, L. Xiao, T. Wang*, et al.*, An Integrated Label-Free Cell-Based Biosensor for Simultaneously Monitoring of Cellular Physiology Multiparameter in Vitro, Biomedical Microdevices, 15(2013) 473-80.
[93] L. Du, L. Zou, L. Zhao, L. Huang, P. Wang, C. Wu, Label-Free Functional Assays of Chemical Receptors Using a Bioengineered Cell-Based Biosensor with Localized Extracellular Acidification Measurement, Biosensors and Bioelectronics, 54(2014) 623-7.
[94] K. Su, J. Zhou, L. Zou, T. Wang, L. Zhuang, N. Hu*, et al.*, Integrated Multifunctional Cell-Based Biosensor System for Monitoring Extracellular Acidification and Cellular Growth, Sensors and Actuators A: Physical, 220(2014) 144-52.
[95] A. Seki, K. Kawakubo, M. Iga, S. Nomura, Microbial Assay for Tryptophan Using Silicon-Based Transducer, Sensors And Actuators B-Chemical, 94(2003) 253-6.
[96] W. Yicong, W. Ping, Y. Xuesong, Z. Qingtao, L. Rong, Y. Weimin*, et al.*, A Novel Microphysiometer Based on MLAPS for Drugs Screening, Biosensors and Bioelectronics, 16(2001) 277-86.
[97] H. Tanaka, T. Yoshinobu, H. Iwasaki, Application of the Chemical Imaging Sensor to Electrophysiological Measurement of a Neural Cell, Sensors and Actuators B: Chemical, 59(1999) 21-5.
[98] A.B.M. Ismail, T. Yoshinobu, H. Iwasaki, H. Sugihara, T. Yukimasa, I. Hirata*, et al.*, Investigation on Light-Addressable Potentiometric Sensor as a Possible Cell–Semiconductor Hybrid, Biosensors and Bioelectronics, 18(2003) 1509-14.

[99] G.X. Xu, X.S. Ye, L.F. Qin, Y. Xu, Y. Li, R. Li*, et al.*, Cell-Based Biosensors Based on Light-Addressable Potentiometric Sensors for Single Cell Monitoring, Biosensors & Bioelectronics, 20(2005) 1757-63.
[100] Q. Liu, H. Cai, Y. Xu, Y. Li, R. Li, P. Wang, Olfactory Cell-Based Biosensor: A First Step Towards a Neurochip of Bioelectronic Nose, Biosensors and Bioelectronics, 22(2006) 318-22.
[101] C. Wu, P. Chen, H. Yu, Q. Liu, X. Zong, H. Cai*, et al.*, A Novel Biomimetic Olfactory-Based Biosensor for Single Olfactory Sensory Neuron Monitoring, Biosensors and Bioelectronics, 24(2009) 1498-502.
[102] Q. Liu, W. Ye, H. Yu, N. Hu, L. Du, P. Wang*, et al.*, Olfactory Mucosa Tissue-Based Biosensor: A Bioelectronic Nose with Receptor Cells in Intact Olfactory Epithelium, Sensors and Actuators B: Chemical, 146(2010) 527-33.
[103] Q. Liu, H. Huang, H. Cai, Y. Xu, Y. Li, R. Li*, et al.*, Embryonic Stem Cells as a Novel Cell Source of Cell-Based Biosensors, Biosensors and Bioelectronics, 22(2007) 810-5.
[104] Q. Liu, H. Cai, Y. Xu, L. Xiao, M. Yang, P. Wang, Detection of Heavy Metal Toxicity Using Cardiac Cell-Based Biosensor, Biosensors and Bioelectronics, 22(2007) 3224-9.
[105] W. Zhang, Y. Li, Q. Liu, Y. Xu, H. Cai, P. Wang, A Novel Experimental Research Based on Taste Cell Chips for Taste Transduction Mechanism, Sensors and Actuators B: Chemical, 131(2008) 24-8.
[106] P. Chen, X.-d. Liu, B. Wang, G. Cheng, P. Wang, A Biomimetic Taste Receptor Cell-Based Biosensor for Electrophysiology Recording and Acidic Sensation, Sensors and Actuators B: Chemical, 139(2009) 576-83.
[107] L.B. Gu, J.H. Han, D.F. Qui, H. Zhang, The Research of Light Addressable Potentiometric Sensor on Detection of Alpha Feto-Protein, Chinese Journal Of Analytical Chemistry, 33(2005) 17-21.
[108] Y. Jia, M. Qin, H. Zhang, W. Niu, X. Li, L. Wang*, et al.*, Label-Free Biosensor: A Novel Phage-Modified Light Addressable Potentiometric Sensor System for Cancer Cell Monitoring, Biosensors and Bioelectronics, 22(2007) 3261-6.
[109] Y. Jia, C. Gao, D. Feng, M. Wu, Y. Liu, X. Chen*, et al.*, Bio-Initiated Light Addressable Potentiometric Sensor for Unlabeled Biodetection and Its Medici Simulation, Analyst, 136(2011) 4533-8.
[110] Y.-F. Jia, C.-Y. Gao, J. He, D.-F. Feng, K.-L. Xing, M. Wu*, et al.*, Unlabeled Multi Tumor Marker Detection System Based on Bioinitiated Light Addressable Potentiometric Sensor, Analyst, 137(2012) 3806-13.
[111] J. Liang, M. Guan, G. Huang, H. Qiu, Z. Chen, G. Li*, et al.*, Highly Sensitive Covalently Functionalized Light-Addressable Potentiometric Sensor for Determination of Biomarker, Materials Science and Engineering: C, 63(2016) 185-91.
[112] X.-l. Zong, C.-s. Wu, X.-l. Wu, Y.-f. Lu, P. Wang, A Non-Labeled DNA Biosensor Based on Light Addressable Potentiometric Sensor Modified with Tio2 Thin Film, Journal of Zhejiang University SCIENCE B, 10(2009) 860.
[113] Y. Jia, X.-B. Yin, J. Zhang, S. Zhou, M. Song, K.-L. Xing, Graphene Oxide Modified Light Addressable Potentiometric Sensor and Its Application for Ssdna Monitoring, Analyst, 137(2012) 5866-73.
[114] T. Bronder, C.S. Wu, A. Poghossian, C.F. Werner, M. Keusgen, M.J. Schöning, Label-Free Detection of DNA Hybridization with Light-Addressable Potentiometric Sensors: Comparison of Various DNA-Immobilization Strategies, Procedia Engineering, 87(2014) 755-8.
[115] C. Wu, T. Bronder, A. Poghossian, C.F. Werner, M. Baecker, M.J. Schoening, Label-Free Electrical Detection of DNA with a Multi-Spot LAPS: First Step Towards Light-Addressable DNA Chips, Physica Status Solidi a-Applications And Materials Science, 211(2014) 1423-8.
[116] C. Wu, T. Bronder, A. Poghossian, C.F. Werner, M.J. Schoning, Label-Free Detection of DNA Using a Light-Addressable Potentiometric Sensor Modified with a Positively Charged Polyelectrolyte Layer,

Nanoscale, 7(2015) 6143-50.
[117] C. Wu, L. Du, L. Zou, L. Zhao, P. Wang, An Atp Sensitive Light Addressable Biosensor for Extracellular Monitoring of Single Taste Receptor Cell, Biomedical Microdevices, 14(2012) 1047-53.
[118] C. Shao, S. Zhou, X.B. Yin, Y.J. Gu, Y.F. Jia, Influences of Probe's Morphology for Metal Ion Detection Based on Light-Addressable Potentiometric Sensors, Sensors, 16(2016).
[119] Y. Gu, C. Ju, Y. Li, Z. Shang, Y. Wu, Y. Jia*, et al.*, Detection of Circulating Tumor Cells in Prostate Cancer Based on Carboxylated Graphene Oxide Modified Light Addressable Potentiometric Sensor, Biosensors and Bioelectronics, 66(2015) 24-31.
[120] S. Krause, H. Talabani, M. Xu, W. Moritz, J. Griffiths, Scanning Photo-Induced Impedance Microscopy—an Impedance Based Imaging Technique, Electrochimica Acta, 47(2002) 2143-8.
[121] H. Yu, J. Wang, Q. Liu, W. Zhang, H. Cai, P. Wang, High Spatial Resolution Impedance Measurement of Eis Sensors for Light Addressable Cell Adhesion Monitoring, Biosensors and Bioelectronics, 26(2011) 2822-7.
[122] C. Wu, J. Zhou, N. Hu, D. Ha, X. Miao, P. Wang, Cellular Impedance Sensing Combined with LAPS as a New Means for Real-Time Monitoring Cell Growth and Metabolism, Sensors and Actuators A: Physical, 199(2013) 136-42.
[123] M. Sartore, M. Adami, C. Nicolini, L. Bousse, S. Mostarshed, D. Hafeman, Minority Carrier Diffusion Length Effects on Light-Addressable Potentiometric Sensor (LAPS) Devices, Sensors and Actuators A: Physical, 32(1992) 431-6.
[124] M. Adami, M. Sartore, E. Baldini, A. Rossi, C. Nicolini, New Measuring Principle for LAPS Devices, Sensors And Actuators B-Chemical, 9(1992) 25-31.
[125] T. Yoshinobu, M.J. Schöning, R. Otto, K. Furuichi, Y. Mourzina, Y. Ermolenko*, et al.*, Portable Light-Addressable Potentiometric Sensor (LAPS) for Multisensor Applications, Sensors and Actuators B: Chemical, 95(2003) 352-6.
[126] M.J. Schöning, T. Wagner, C. Wang, R. Otto, T. Yoshinobu, Development of a Handheld 16 Channel Pen-Type LAPS for Electrochemical Sensing, Sensors and Actuators B: Chemical, 108(2005) 808-14.
[127] T. Wagner, T. Yoshinobu, C. Rao, R. Otto, M.J. Schöning, “All-in-One” Solid-State Device Based on a Light-Addressable Potentiometric Sensor Platform, Sensors and Actuators B: Chemical, 117(2006) 472-9.
[128] T. Wagner, C. Rao, J.P. Kloock, T. Yoshinobu, R. Otto, M. Keusgen*, et al.*, “LAPS Card”—a Novel Chip Card-Based Light-Addressable Potentiometric Sensor (LAPS), Sensors and Actuators B: Chemical, 118(2006) 33-40.
[129] M. Nakao, S. Inoue, R. Oishi, T. Yoshinobu, H. Iwasaki, Observation of Microorganism Colonies Using a Scanning-Laser-Beam pH-Sensing Microscope, Journal of Fermentation and Bioengineering, 79(1995) 163-6.
[130] S. Inoue, M. Nakao, T. Yoshinobu, H. Iwasaki, Chemical-Imaging Sensor Using Enzyme, Sensors And Actuators B-Chemical, 32(1996) 23-6.
[131] T. Yoshinobu, N. Oba, H. Iwasaki, Visualization of Chemical Waves in Belousav-Zhabotinsky Reaction by Chemical Imaging Sensors, Journal Of the Electrochemical Society, 144(1997) 3919-21.
[132] T. Yoshinobu, T. Harada, H. Iwasaki, Application of the pH-Imaging Sensor to Determining the Diffusion Coefficients of Ions in Electrolytic Solutions, Japanese Journal Of Applied Physics Part 2-Letters, 39(2000) L318-L20.
[133] J. Wang, F. Wu, M. Watkinson, J.Y. Zhu, S. Krause, "Click" Patterning of Self-Assembled Monolayers

on Hydrogen-Terminated Silicon Surfaces and Their Characterization Using Light-Addressable Potentiometric Sensors, Langmuir, 31(2015) 9646-54.
[134] F. Wu, D.-W. Zhang, J. Wang, M. Watkinson, S. Krause, Copper Contamination of Self-Assembled Organic Monolayer Modified Silicon Surfaces Following a "Click" Reaction Characterized with LAPS and SPIM, Langmuir, 33(2017) 3170-7.
[135] K.-i. Miyamoto, Y. Hirayama, T. Wagner, M.J. Schöning, T. Yoshinobu, Visualization of Enzymatic Reaction in a Microfluidic Channel Using Chemical Imaging Sensor, Electrochimica Acta, 113(2013) 768-72.
[136] F. Schreiber, Structure and Growth of Self-Assembling Monolayers, Progress In Surface Science, 65(2000) 151-256.
[137] R. Boukherroub, S. Morin, D.D.M. Wayner, F. Bensebaa, G.I. Sproule, J.M. Baribeau*, et al.*, Ideal Passivation of Luminescent Porous Silicon by Thermal, Noncatalytic Reaction with Alkenes and Aldehydes, Chemistry Of Materials, 13(2001) 2002-11.
[138] P.T. Hurley, E.J. Nemanick, B.S. Brunschwig, N.S. Lewis, Covalent Attachment of Acetylene and Methylacetylene Functionality to Si(111) Surfaces: Scaffolds for Organic Surface Functionalization While Retaining Si-C Passivation of Si(111) Surface Sites, Journal Of the American Chemical Society, 128(2006) 9990-1.
[139] E.J. Nemanick, P.T. Hurley, L.J. Webb, D.W. Knapp, D.J. Michalak, B.S. Brunschwig*, et al.*, Chemical and Electrical Passivation of Single-Crystal Silicon(100) Surfaces through a Two-Step Chlorination/Alkylation Process, Journal Of Physical Chemistry B, 110(2006) 14770-8.
[140] S. Ciampi, J.B. Harper, J.J. Gooding, Wet Chemical Routes to the Assembly of Organic Monolayers on Silicon Surfaces Via the Formation of Si-C Bonds: Surface Preparation, Passivation and Functionalization, Chemical Society Reviews, 39(2010) 2158-83.
[141] N. Alderman, L. Danos, M.C. Grossel, T. Markvart, Kelvin Probe Studies of Alkyl Monolayers on Silicon (111) for Surface Passivation, Rsc Advances, 3(2013) 20125-31.
[142] O. Yaffe, L. Scheres, S.R. Puniredd, N. Stein, A. Biller, R.H. Lavan*, et al.*, Molecular Electronics at Metal/Semiconductor Junctions. Si Inversion by Sub-Nanometer Molecular Films, Nano Letters, 9(2009) 2390-4.
[143] R. Har-Lavan, O. Yaffe, P. Joshi, R. Kazaz, H. Cohen, D. Cahen, Ambient Organic Molecular Passivation of Si Yields near-Ideal, Schottky-Mott Limited, Junctions, Aip Advances, 2(2012).
[144] O. Yaffe, T. Ely, R. Har-Lavan, D.A. Egger, S. Johnston, H. Cohen*, et al.*, Effect of Molecule-Surface Reaction Mechanism on the Electronic Characteristics and Photovoltaic Performance of Molecularly Modified Si, Journal Of Physical Chemistry C, 117(2013) 22351-61.
[145] R. Har-Lavan, R. Schreiber, O. Yaffe, D. Cahen, Molecular Field Effect Passivation: Quinhydrone/Methanol Treatment of N-Si(100), Journal Of Applied Physics, 113(2013).
[146] Y. Yang, S. Ciampi, M.H. Choudhury, J.J. Gooding, Light Activated Electrochemistry: Light Intensity and pH Dependence on Electrochemical Performance of Anthraquinone Derivatized Silicon, Journal Of Physical Chemistry C, 120(2016) 2874-82.
[147] D. Samanta, A. Sarkar, Immobilization of Bio-Macromolecules on Self-Assembled Monolayers: Methods and Sensor Applications, Chemical Society Reviews, 40(2011) 2567-92.
[148] A. Seki, S. Nomura, Urease-Based Heavy Metal Ion Sensing Using a Silicon Transducer, Sensors And Materials, 16(2004) 377-82.
[149] W. Cai, J.R. Peck, D.W. van der Weide, R.J. Hamers, Direct Electrical Detection of Hybridization at

DNA-Modified Silicon Surfaces, Biosensors & Bioelectronics, 19(2004) 1013-9.
[150] F. Wei, B. Sun, Y. Guo, X.S. Zhao, Monitoring DNA Hybridization on Alkyl Modified Silicon Surface through Capacitance Measurement, Biosensors & Bioelectronics, 18(2003) 1157-63.
[151] W.E. Lee, H.G. Thompson, J.G. Hall, D.E. Bader, Rapid Detection and Identification of Biological and Chemical Agents by Immunoassay, Gene Probe Assay and Enzyme Inhibition Using a Silicon-Based Biosensor, Biosensors & Bioelectronics, 14(2000) 795-804.
[152] J.N. Chazalviel, P. Allongue, A.C. Gouget-Laemmel, C.H. de Villeneuve, A. Moraillon, F. Ozanam, Covalent Functionalizations of Silicon Surfaces and Their Application to Biosensors, Science Of Advanced Materials, 3(2011) 332-53.
[153] S.R. Wasserman, Y.T. Tao, G.M. Whitesides, Structure and Reactivity of Alkylsiloxane Monolayers Formed by Reaction of Alkyltrichlorosilanes on Silicon Substrates, Langmuir, 5(1989) 1074-87.
[154] S.R. Wasserman, G.M. Whitesides, I.M. Tidswell, B.M. Ocko, P.S. Pershan, J.D. Axe, The Structure of Self-Assembled Monolayers of Alkylsiloxanes on Silicon - a Comparison of Results from Ellipsometry and Low-Angle X-Ray Reflectivity, Journal Of the American Chemical Society, 111(1989) 5852-61.
[155] I.M. Tidswell, B.M. Ocko, P.S. Pershan, S.R. Wasserman, G.M. Whitesides, J.D. Axe, X-Ray Specular Reflection Studies of Silicon Coated by Organic Monolayers (Alkylsiloxanes), Physical Review B, 41(1990) 1111-28.
[156] M.V. Baker, J.D. Watling, Functionalization of Alkylsiloxane Monolayers Via Free-Radical Bromination, Langmuir, 13(1997) 2027-32.
[157] D. Vuillaume, C. Boulas, J. Collet, G. Allan, C. Delerue, Electronic Structure of a Heterostructure of an Alkylsiloxane Self-Assembled Monolayer on Silicon, Physical Review B, 58(1998) 16491-8.
[158] N. Rozlosnik, M.C. Gerstenberg, N.B. Larsen, Effect of Solvents and Concentration on the Formation of a Self-Assembled Monolayer of Octadecylsiloxane on Silicon (001), Langmuir, 19(2003) 1182-8.
[159] P. Thissen, O. Seitz, Y.J. Chabal, Wet Chemical Surface Functionalization of Oxide-Free Silicon, Progress In Surface Science, 87(2012) 272-90.
[160] W.J.I. DeBenedetti, Y.J. Chabal, Functionalization of Oxide-Free Silicon Surfaces, Journal Of Vacuum Science & Technology A, 31(2013).
[161] R.H. Tian, O. Seitz, M. Li, W.C. Hu, Y.J. Chabal, J.M. Gao, Infrared Characterization of Interfacial Si-O Bond Formation on Silanized Flat Sio2/Si Surfaces, Langmuir, 26(2010) 4563-6.
[162] Y.L. Wang, M. Lieberman, Growth of Ultrasmooth Octadecyltrichlorosilane Self-Assembled Monolayers on Sio2, Langmuir, 19(2003) 1159-67.
[163] G.S. Higashi, R.S. Becker, Y.J. Chabal, A.J. Becker, Comparison of Si(111) Surfaces Prepared Using Aqueous-Solutions of Nh_4f Versus Hf, Applied Physics Letters, 58(1991) 1656-8.
[164] D.K. Aswal, S. Lenfant, D. Guerin, J.V. Yakhmi, D. Vuillaume, Self Assembled Monolayers on Silicon for Molecular Electronics, Analytica Chimica Acta, 568(2006) 84-108.
[165] J. Veerbeek, J. Huskens, Applications of Monolayer‐Functionalized H‐Terminated Silicon Surfaces: A Review, Small Methods, (2017).
[166] M.R. Linford, C.E.D. Chidsey, Alkyl Monolayers Covalently Bonded to Silicon Surfaces, Journal Of the American Chemical Society, 115(1993) 12631-2.
[167] M.R. Linford, P. Fenter, P.M. Eisenberger, C.E.D. Chidsey, Alkyl Monolayers on Silicon Prepared from 1-Alkenes and Hydrogen-Terminated Silicon, Journal Of the American Chemical Society, 117(1995) 3145-55.

[168] G.F. Cerofolini, C. Galati, S. Reina, L. Renna, The Addition of Functional Groups to Silicon Via Hydrosilation of 1-Alkynes at Hydrogen-Terminated, 1 X 1 Reconstructed, (100) Silicon Surfaces, Semiconductor Science And Technology, 18(2003) 423-9.
[169] G.F. Cerofolini, C. Galati, S. Reina, L. Renna, Functionalization of the (100) Surface of Hydrogen-Terminated Silicon Via Hydrosilation of 1-Alkyne, Materials Science & Engineering C-Biomimetic And Supramolecular Systems, 23(2003) 253-7.
[170] S. Ciampi, T. Bocking, K.A. Kilian, M. James, J.B. Harper, J.J. Gooding, Functionalization of Acetylene-Terminated Monolayers on Si(100) Surfaces: A Click Chemistry Approach, Langmuir, 23(2007) 9320-9.
[171] A.B. Sieval, R. Opitz, H.P.A. Maas, M.G. Schoeman, G. Meijer, F.J. Vergeldt*, et al.*, Monolayers of 1-Alkynes on the H-Terminated Si(100) Surface, Langmuir, 16(2000) 10359-68.
[172] A. Ng, S. Ciampi, M. James, J.B. Harper, J.J. Gooding, Comparing the Reactivity of Alkynes and Alkenes on Silicon (100) Surfaces, Langmuir, 25(2009) 13934-41.
[173] L. Scheres, M. Giesbers, H. Zuilhof, Self-Assembly of Organic Monolayers onto Hydrogen-Terminated Silicon: 1-Alkynes Are Better Than 1-Alkenes, Langmuir, 26(2010) 10924-9.
[174] L. Scheres, M. Giesbers, H. Zuilhof, Organic Monolayers onto Oxide-Free Silicon with Improved Surface Coverage: Alkynes Versus Alkenes, Langmuir, 26(2010) 4790-5.
[175] P. Michaels, M.T. Alam, S. Ciampi, W. Rouesnel, S.G. Parker, M.H. Choudhury*, et al.*, A Robust DNA Interface on a Silicon Electrode, Chemical Communications, 50(2014) 7878-80.
[176] T. Jalkanen, E. Makila, T. Sakka, J. Salonen, Y.H. Ogata, Thermally Promoted Addition of Undecylenic Acid on Thermally Hydrocarbonized Porous Silicon Optical Reflectors, Nanoscale Research Letters, 7(2012).
[177] T. Hu, Y. Zhang, T.C. Chilcott, H.G.L. Coster, Investigation of Carboxylic-Functionalized Self-Assembled Monolayers on Silicon and Gold and Their Application as pH-Sensitive Probes Using Electrical Impedance Spectroscopy, in: N.A. AbuOsman, F. Ibrahim, W.A.B. WanAbas, H.S. AbdulRahman, H.N. Ting (Eds.), 4th Kuala Lumpur International Conference on Biomedical Engineering 2008, Vols 1 and 22008, pp. 86-90.
[178] H. Jin, C.R. Kinser, P.A. Bertin, D.E. Kramer, J.A. Libera, M.C. Hersam*, et al.*, X-Ray Studies of Self-Assembled Organic Monolayers Grown on Hydrogen-Terminated Si(Iii), Langmuir, 20(2004) 6252-8.
[179] R. Boukherroub, J.T.C. Wojtyk, D.D.M. Wayner, D.J. Lockwood, Thermal Hydrosilylation of Undecylenic Acid with Porous Silicon, Journal Of the Electrochemical Society, 149(2002) H59-H63.
[180] S. Ciampi, G. Le Saux, J.B. Harper, J.J. Gooding, Optimization of Click Chemistry of Ferrocene Derivatives on Acetylene-Functionalized Silicon(100) Surfaces, Electroanalysis, 20(2008) 1513-9.
[181] S. Ciampi, P.K. Eggers, G. Le Saux, M. James, J.B. Harper, J.J. Gooding, Silicon (100) Electrodes Resistant to Oxidation in Aqueous Solutions: An Unexpected Benefit of Surface Acetylene Moieties, Langmuir, 25(2009) 2530-9.
[182] M. James, S. Ciampi, T.A. Darwish, T.L. Hanley, S.O. Sylvester, J.J. Gooding, Nanoscale Water Condensation on Click-Functionalized Self-Assembled Monolayers, Langmuir, 27(2011) 10753-62.
[183] S. Ciampi, M. James, M.H. Choudhury, N.A. Darwish, J.J. Gooding, The Detailed Characterization of Electrochemically Switchable Molecular Assemblies on Silicon Electrodes, Physical Chemistry Chemical Physics, 15(2013) 9879-90.
[184] Y.F. Wu, M.B. Kashi, Y. Yang, V.R. Goncales, S. Ciampi, R.D. Tilley*, et al.*, Light-Activated Electrochemistry on Alkyne-Terminated Si(100) Surfaces Towards Solution-Based Redox Probes, Electrochimica Acta, 213(2016) 540-6.
[185] J. Terry, M.R. Linford, C. Wigren, R.Y. Cao, P. Pianetta, C.E.D. Chidsey, Determination of the Bonding

of Alkyl Monolayers to the Si(111) Surface Using Chemical-Shift, Scanned-Energy Photoelectron Diffraction, Applied Physics Letters, 71(1997) 1056-8.
[186] R.L. Cicero, M.R. Linford, C.E.D. Chidsey, Photoreactivity of Unsaturated Compounds with Hydrogen-Terminated Silicon(111), Langmuir, 16(2000) 5688-95.
[187] R. Boukherroub, D.D.M. Wayner, Controlled Functionalization and Multistep Chemical Manipulation of Covalently Modified Si(111) Surfaces, Journal Of the American Chemical Society, 121(1999) 11513-5.
[188] Q.Y. Sun, L. de Smet, B. van Lagen, M. Giesbers, P.C. Thune, J. van Engelenburg*, et al.*, Covalently Attached Monolayers on Crystalline Hydrogen-Terminated Silicon: Extremely Mild Attachment by Visible Light, Journal Of the American Chemical Society, 127(2005) 2514-23.
[189] M.P. Stewart, J.M. Buriak, Exciton-Mediated Hydrosilylation on Photoluminescent Nanocrystalline Silicon, Journal Of the American Chemical Society, 123(2001) 7821-30.
[190] L. de Smet, G.A. Stork, G.H.F. Hurenkamp, Q.Y. Sun, H. Topal, P.J.E. Vronen*, et al.*, Covalently Attached Saccharides on Silicon Surfaces, Journal Of the American Chemical Society, 125(2003) 13916-7.
[191] Q.Y. Sun, L. de Smet, B. van Lagen, A. Wright, H. Zuilhof, E.J.R. Sudholter, Covalently Attached Monolayers on Hydrogen Terminated Si(100): Extremely Mild Attachment by Visible Light, Angewandte Chemie-International Edition, 43(2004) 1352-5.
[192] X.Y. Wang, R.E. Ruther, J.A. Streifer, R.J. Hamers, Uv-Induced Grafting of Alkenes to Silicon Surfaces: Photoemission Versus Excitons, Journal Of the American Chemical Society, 132(2010) 4048-+.
[193] J.M. Schmeltzer, L.A. Porter, M.P. Stewart, J.M. Buriak, Hydride Abstraction Initiated Hydrosilylation of Terminal Alkenes and Alkynes on Porous Silicon, Langmuir, 18(2002) 2971-4.
[194] R. Boukherroub, S. Morin, F. Bensebaa, D.D.M. Wayner, New Synthetic Routes to Alkyl Monolayers on the Si(111) Surface, Langmuir, 15(1999) 3831-5.
[195] W. Cai, Z. Lin, T. Strother, L.M. Smith, R.J. Hamers, Chemical Modification and Patterning of Iodine-Terminated Silicon Surfaces Using Visible Light, Journal Of Physical Chemistry B, 106(2002) 2656-64.
[196] R. Voicu, R. Boukherroub, V. Bartzoka, T. Ward, J.T.C. Wojtyk, D.D.M. Wayner, Formation, Characterization, and Chemistry of Undecanoic Acid-Terminated Silicon Surfaces: Patterning and Immobilization of DNA, Langmuir, 20(2004) 11713-20.
[197] H. Kim, P.E. Colavita, K.M. Metz, B.M. Nichols, B. Sun, J. Uhlrich*, et al.*, Photochemical Functionalization of Gallium Nitride Thin Films with Molecular and Biomolecular Layers, Langmuir, 22(2006) 8121-6.
[198] W.N. Peng, S.M. Rupich, N. Shafiq, Y.N. Gartstein, A.V. Malko, Y.J. Chabal, Silicon Surface Modification and Characterization for Emergent Photovoltaic Applications Based on Energy Transfer, Chemical Reviews, 115(2015) 12764-96.
[199] C.H. deVilleneuve, J. Pinson, M.C. Bernard, P. Allongue, Electrochemical Formation of Close-Packed Phenyl Layers on Si(111), Journal Of Physical Chemistry B, 101(1997) 2415-20.
[200] P. Allongue, C.H. de Villeneuve, J. Pinson, F. Ozanam, J.N. Chazalviel, X. Wallart, Organic Monolayers on Si(111) by Electrochemical Method, Electrochimica Acta, 43(1998) 2791-8.
[201] P. Allongue, V. Costakieling, H. Gerischer, Etching of Silicon in Naoh Solutions .2. Electrochemical Studies of N-Si(111) and N-Si(100) and Mechanism of the Dissolution, Journal Of the Electrochemical Society, 140(1993) 1018-26.
[202] A. Bansal, X.L. Li, I. Lauermann, N.S. Lewis, S.I. Yi, W.H. Weinberg, Alkylation of Si Surfaces Using a Two-Step Halogenation Grignard Route, Journal Of the American Chemical Society, 118(1996) 7225-6.

[203] J. He, S.N. Patitsas, K.F. Preston, R.A. Wolkow, D.D.M. Wayner, Covalent Bonding of Thiophenes to Si(111) by a Halogenation/Thienylation Route, Chemical Physics Letters, 286(1998) 508-14.
[204] N. Shirahata, A. Hozumi, T. Yonezawa, Monolayer-Derivative Functionalization of Non-Oxidized Silicon Surfaces, Chemical Record, 5(2005) 145-59.
[205] T.P. Chopra, R.C. Longo, K. Cho, Y.J. Chabal, Ammonia Modification of Oxide-Free Si(111) Surfaces, Surface Science, 650(2016) 285-94.
[206] F.Y. Tian, A.V. Teplyakov, Silicon Surface Functionalization Targeting Si-N Linkages, Langmuir, 29(2013) 13-28.
[207] W.F. Bergerson, J.A. Mulder, R.P. Hsung, X.Y. Zhu, Assembly of Organic Molecules on Silicon Surfaces Via the Si-N Linkage, Journal Of the American Chemical Society, 121(1999) 454-5.
[208] X.Y. Zhu, J.A. Mulder, W.F. Bergerson, Chemical Vapor Deposition of Organic Monolayers on Si(100) Via Si-N Linkages, Langmuir, 15(1999) 8147-54.
[209] X.Y. Zhu, J.E. Houston, Molecular Lubricants for Silicon-Based Microelectromechanical Systems (Mems): A Novel Assembly Strategy, Tribology Letters, 7(1999) 87-90.
[210] C.A. Hacker, K.A. Anderson, L.J. Richter, C.A. Richter, Comparison of Si-O-C Interfacial Bonding of Alcohols and Aldehydes on Si(111) Formed from Dilute Solution with Ultraviolet Irradiation, Langmuir, 21(2005) 882-9.
[211] X.Y. Zhu, V. Boiadjiev, J.A. Mulder, R.P. Hsung, R.C. Major, Molecular Assemblies on Silicon Surfaces Via Si-O Linkages, Langmuir, 16(2000) 6766-72.
[212] R.D. Rohde, H.D. Agnew, W.-S. Yeo, R.C. Bailey, J.R. Heath, A Non-Oxidative Approach toward Chemically and Electrochemically Functionalizing Si(111), Journal Of the American Chemical Society, 128(2006) 9518-25.
[213] P.G. Cao, K. Xu, J.R. Heath, Azidation of Silicon(111) Surfaces, Journal Of the American Chemical Society, 130(2008) 14910-+.
[214] S. Ciampi, M. James, P. Michaels, J.J. Gooding, Tandem "Click" Reactions at Acetylene-Terminated Si(100) Monolayers, Langmuir, 27(2011) 6940-9.
[215] K. Brooks, J. Yatvin, C.D. McNitt, R.A. Reese, C. Jung, V.V. Popik*, et al.*, Multifunctional Surface Manipulation Using Orthogonal Click Chemistry, Langmuir, 32(2016) 6600-5.
[216] H.C. Kolb, M.G. Finn, K.B. Sharpless, Click Chemistry: Diverse Chemical Function from a Few Good Reactions, Angewandte Chemie-International Edition, 40(2001) 2004-21.
[217] B.T. Worrell, J.A. Malik, V.V. Fokin, Direct Evidence of a Dinuclear Copper Intermediate in Cu(I)-Catalyzed Azide-Alkyne Cycloadditions, Science, 340(2013) 457-60.
[218] L. Britcher, T.J. Barnes, H.J. Griesser, C.A. Prestidge, Pegylation of Porous Silicon Using Click Chemistry, Langmuir, 24(2008) 7625-7.
[219] G.T. Qin, C. Santos, W. Zhang, Y. Li, A. Kumar, U.J. Erasquin*, et al.*, Biofunctionalization on Alkylated Silicon Substrate Surfaces Via "Click" Chemistry, Journal Of the American Chemical Society, 132(2010) 16432-41.
[220] Y. Li, C. Cai, Click Chemistry-Based Functionalization on Non-Oxidized Silicon Substrates, Chemistry-an Asian Journal, 6(2011) 2592-605.
[221] A.G. Marrani, E.A. Dalchiele, R. Zanoni, F. Decker, F. Cattaruzza, D. Bonifazi*, et al.*, Functionalization of Si(100) with Ferrocene Derivatives Via "Click" Chemistry, Electrochimica Acta, 53(2008) 3903-9.
[222] X. Yao, R. Peng, J.D. Ding, Cell-Material Interactions Revealed Via Material Techniques of Surface

Patterning, Advanced Materials, 25(2013) 5257-86.
[223] D. Falconnet, A. Koenig, T. Assi, M. Textor, A Combined Photolithographic and Molecular-Assembly Approach to Produce Functional Micropatterns for Applications in the Biosciences, Advanced Functional Materials, 14(2004) 749-56.
[224] Y. Zhu, A.H. Soeriyadi, S.G. Parker, P.J. Reece, J.J. Gooding, Chemical Patterning on Preformed Porous Silicon Photonic Crystals: Towards Multiplex Detection of Protease Activity at Precise Positions, Journal Of Materials Chemistry B, 2(2014) 3582-8.
[225] Y. Zhu, B. Gupta, B. Guan, S. Ciampi, P.J. Reece, J.J. Gooding, Photolithographic Strategy for Patterning Preformed, Chemically Modified, Porous Silicon Photonic Crystal Using Click Chemistry, Acs Applied Materials & Interfaces, 5(2013) 6514-21.
[226] H. Sorribas, C. Padeste, L. Tiefenauer, Photolithographic Generation of Protein Micropatterns for Neuron Culture Applications, Biomaterials, 23(2002) 893-900.
[227] S. Marchesan, C.D. Easton, K.E. Styan, P. Leech, T.R. Gengenbach, J.S. Forsythe*, et al.*, Su-8 Photolithography on Reactive Plasma Thin-Films: Coated Microwells for Peptide Display, Colloids And Surfaces B-Biointerfaces, 108(2013) 313-21.
[228] D. Cimen, T. Caykara, Micro-Patterned Polymer Brushes by a Combination of Photolithography and Interface-Mediated Raft Polymerization for DNA Hybridization, Polymer Chemistry, 6(2015) 6812-8.
[229] P. Molnar, W.S. Wang, A. Natarajan, J.W. Rumsey, J.J. Hickman, Photolithographic Patterning of C2c12 Myotubes Using Vitronectin as Growth Substrate in Serum-Free Medium, Biotechnology Progress, 23(2007) 265-8.
[230] Z.H. Nie, E. Kumacheva, Patterning Surfaces with Functional Polymers, Nature Materials, 7(2008) 277-90.
[231] D.I. Rozkiewicz, D. Janczewski, W. Verboom, B.J. Ravoo, D.N. Reinhoudt, "Click" Chemistry by Microcontact Printing, Angewandte Chemie-International Edition, 45(2006) 5292-6.
[232] S.H. Hsu, D.N. Reinhoudt, J. Huskens, A.H. Velders, Imidazolide Monolayers for Reactive Microcontact Printing, Journal Of Materials Chemistry, 18(2008) 4959-63.
[233] L. Yan, W.T.S. Huck, X.M. Zhao, G.M. Whitesides, Patterning Thin Films of Poly(Ethylene Imine) on a Reactive Sam Using Microcontact Printing, Langmuir, 15(1999) 1208-14.
[234] G. Csucs, R. Michel, J.W. Lussi, M. Textor, G. Danuser, Microcontact Printing of Novel Co-Polymers in Combination with Proteins for Cell-Biological Applications, Biomaterials, 24(2003) 1713-20.
[235] S.A. Lange, V. Benes, D.P. Kern, J.K.H. Horber, A. Bernard, Microcontact Printing of DNA Molecules, Analytical Chemistry, 76(2004) 1641-7.
[236] D.I. Rozkiewicz, J. Gierlich, G.A. Burley, K. Gutsmiedl, T. Carell, B.J. Ravoo*, et al.*, Transfer Printing of DNA by "Click" Chemistry, Chembiochem, 8(2007) 1997-2002.
[237] R.S. Kane, S. Takayama, E. Ostuni, D.E. Ingber, G.M. Whitesides, Patterning Proteins and Cells Using Soft Lithography, Biomaterials, 20(1999) 2363-76.
[238] D.I. Rozkiewicz, Y. Kraan, M.W.T. Werten, F.A. de Wolf, V. Subramaniam, B.J. Ravoo*, et al.*, Covalent Microcontact Printing of Proteins for Cell Patterning, Chemistry-a European Journal, 12(2006) 6290-7.
[239] A. Bernard, J.P. Renault, B. Michel, H.R. Bosshard, E. Delamarche, Microcontact Printing of Proteins, Advanced Materials, 12(2000) 1067-70.
[240] B.C. Wheeler, J.M. Corey, G.J. Brewer, D.W. Branch, Microcontact Printing for Precise Control of Nerve Cell Growth in Culture, Journal Of Biomechanical Engineering-Transactions Of the Asme, 121(1999) 73-8.

[241] M. Mrksich, L.E. Dike, J. Tien, D.E. Ingber, G.M. Whitesides, Using Microcontact Printing to Pattern the Attachment of Mammalian Cells to Self-Assembled Monolayers of Alkanethiolates on Transparent Films of Gold and Silver, Experimental Cell Research, 235(1997) 305-13.
[242] Z. Wang, P. Zhang, B. Kirkland, Y. Liu, J. Guan, Microcontact Printing of Polyelectrolytes on Peg Using an Unmodified Pdms Stamp for Micropatterning Nanoparticles, DNA, Proteins and Cells, Soft Matter, 8(2012) 7630-7.
[243] A. Kumar, G.M. Whitesides, Features of Gold Having Micrometer to Centimeter Dimensions Can Be Formed through a Combination of Stamping with an Elastomeric Stamp and an Alkanethiol Ink Followed by Chemical Etching, Applied Physics Letters, 63(1993) 2002-4.
[244] T. Kaufmann, B.J. Ravoo, Stamps, Inks and Substrates: Polymers in Microcontact Printing, Polymer Chemistry, 1(2010) 371-87.
[245] H. Nandivada, H.Y. Chen, L. Bondarenko, J. Lahann, Reactive Polymer Coatings That "Click"", Angewandte Chemie-International Edition, 45(2006) 3360-3.
[246] J.M. Spruell, B.A. Sheriff, D.I. Rozkiewicz, W.R. Dichtel, R.D. Rohde, D.N. Reinhoudt*, et al.*, Heterogeneous Catalysis through Microcontact Printing, Angewandte Chemie-International Edition, 47(2008) 9927-32.
[247] D.I. Rozkiewicz, B.J. Ravoo, D.N. Reinhoudt, Reversible Covalent Patterning of Self-Assembled Monolayers on Gold and Silicon Oxide Surfaces, Langmuir, 21(2005) 6337-43.
[248] D.C. Trimbach, B. Keller, R. Bhat, S. Zankovych, R. Pohlmann, S. Schroter*, et al.*, Enhanced Osteoblast Adhesion to Epoxide-Functionalized Surfaces, Advanced Functional Materials, 18(2008) 1723-31.
[249] M. Rauschenberg, E.C. Fritz, C. Schulz, T. Kaufmann, B.J. Ravoo, Molecular Recognition of Surface-Immobilized Carbohydrates by a Synthetic Lectin, Beilstein Journal Of Organic Chemistry, 10(2014) 1354-64.
[250] J. Mehlich, B.J. Ravoo, Click Chemistry by Microcontact Printing on Self-Assembled Monolayers: A Structure-Reactivity Study by Fluorescence Microscopy, Organic & Biomolecular Chemistry, 9(2011) 4108-15.
[251] S. Bergner, P. Vatsyayan, F.M. Matysik, Recent Advances in High Resolution Scanning Electrochemical Microscopy of Living Cells - a Review, Analytica Chimica Acta, 775(2013) 1-13.
[252] Y. Takahashi, A.I. Shevchuk, P. Novak, B. Babakinejad, J. Macpherson, P.R. Unwin*, et al.*, Topographical and Electrochemical Nanoscale Imaging of Living Cells Using Voltage-Switching Mode Scanning Electrochemical Microscopy, Proceedings Of the National Academy Of Sciences Of the United States Of America, 109(2012) 11540-5.
[253] W. Wang, Y. Xiong, F.Y. Du, W.H. Huang, W.Z. Wu, Z.L. Wang*, et al.*, Imaging and Detection of Morphological Changes of Single Cells before and after Secretion Using Scanning Electrochemical Microscopy, Analyst, 132(2007) 515-8.
[254] D. Polcari, P. Dauphin-Ducharme, J. Mauzeroll, Scanning Electrochemical Microscopy: A Comprehensive Review of Experimental Parameters from 1989 to 2015, Chemical Reviews, 116(2016) 13234-78.
[255] A. Page, D. Perry, P.R. Unwin, Multifunctional Scanning Ion Conductance Microscopy, Proceedings of the Royal Society A: Mathematical, Physical and Engineering Science, 473(2017).
[256] M.Y. Kang, D. Momotenko, A. Page, D. Perry, P.R. Unwin, Frontiers in Nanoscale Electrochemical Imaging: Faster, Multifunctional, and Ultrasensitive, Langmuir, 32(2016) 7993-8008.

[257] J. Seifert, J. Rheinlaender, P. Novak, Y.E. Korchev, T.E. Schaffer, Comparison of Atomic Force Microscopy and Scanning Ion Conductance Microscopy for Live Cell Imaging, Langmuir, 31(2015) 6807-13.
[258] H. Yamada, Imaging a Single Living Cell Via Shear Force-Based Scanning Ion Conductance Microscopy in Standing Approach Mode with Differential Control, Electrochimica Acta, 136(2014) 233-9.
[259] D. Perry, B.P. Nadappuram, D. Momotenko, P.D. Voyias, A. Page, G. Tripathi*, et al.*, Surface Charge Visualization at Viable Living Cells, Journal Of the American Chemical Society, 138(2016) 3152-60.
[260] K. McKelvey, D. Perry, J.C. Byers, A.W. Colburn, P.R. Unwin, Bias Modulated Scanning Ion Conductance Microscopy, Analytical Chemistry, 86(2014) 3639-46.
[261] K.J. Foley, X. Shan, N.J. Tao, Surface Impedance Imaging Technique, Analytical Chemistry, 80(2008) 5146-51.
[262] W. Wang, K. Foley, X. Shan, S.P. Wang, S. Eaton, V.J. Nagaraj*, et al.*, Single Cells and Intracellular Processes Studied by a Plasmonic-Based Electrochemical Impedance Microscopy, Nature Chemistry, 3(2011) 249-55.
[263] J. Lu, J.H. Li, Label-Free Imaging of Dynamic and Transient Calcium Signaling in Single Cells, Angewandte Chemie-International Edition, 54(2015) 13576-80.
[264] X.W. Liu, Y.Z. Yang, W. Wang, S.P. Wang, M. Gao, J. Wu*, et al.*, Plasmonic-Based Electrochemical Impedance Imaging of Electrical Activities in Single Cells, Angewandte Chemie-International Edition, 56(2017) 8855-9.
[265] S.E. Creager, J. Clarke, Contact-Angle Titrations of Mixed Omega-Mercaptoalkanoic Acid Alkanethiol Monolayers on Gold - Reactive Vs Nonreactive Spreading, and Chain-Length Effects on Surface Pk(a) Values, Langmuir, 10(1994) 3675-83.
[266] Y.L. Ji, H.H. Chen, Q.S. Yu, X.H. Ma, H.B. Ma, Contact Angle Variation on a Copper Surface Treated with Self-Assembled Monolayer (Sam) of N-Octadecyl Mercaptan, Journal Of Heat Transfer-Transactions Of the Asme, 133(2011).
[267] D. Polster, H. Graaf, Advancing and Receding Angles - Dynamic Contact Angle Measurements on Mixed Alkyl Monolayers, Applied Surface Science, 265(2013) 88-93.
[268] T.R.L. Yuehua Yuan, Contact Angle and Wetting Properties, in: B.H. G. Bracco (Ed.) Surface Science Techniques, Springer Berlin Heidelberg, 2013, pp. 3-34.
[269] M.D. Porter, T.B. Bright, D.L. Allara, C.E.D. Chidsey, Spontaneously Organized Molecular Assemblies .4. Structural Characterization of Normal-Alkyl Thiol Monolayers on Gold by Optical Ellipsometry, Infrared-Spectroscopy, and Electrochemistry, Journal Of the American Chemical Society, 109(1987) 3559-68.
[270] I. J. A. Woollam Co., Completeease ^{Tm} Data Analysis Manual, Lincoln, NE2011.
[271] V. Bindu, T. Pradeep, Characterisation of Alkanethiol (Cnh2n+1sh, N = 3, 4, 6, 8, 10, 12 and 18) Self Assembled Monolayers by X-Ray Photoelectron Spectroscopy, Vacuum, 49(1998) 63-6.
[272] H. Okawa, T. Wada, H. Sasabe, K. Kajikawa, K. Seki, Y. Ouchi, X-Ray Photoelectron Spectroscopy Study of a Self-Assembled Monolayer of Thiophene Thiol, Japanese Journal Of Applied Physics Part 1-Regular Papers Short Notes & Review Papers, 39(2000) 252-5.
[273] L.J. Webb, E.J. Nemanick, J.S. Biteen, D.W. Knapp, D.J. Michalak, M.C. Traub*, et al.*, High-Resolution X-Ray Photoelectron Spectroscopic Studies of Alkylated Silicon(111) Surfaces, Journal Of Physical Chemistry B, 109(2005) 3930-7.
[274] M. Zharnikov, High-Resolution X-Ray Photoelectron Spectroscopy in Studies of Self-Assembled Organic Monolayers, Journal Of Electron Spectroscopy And Related Phenomena, 178(2010) 380-93.

[275] J.M. Hollander, W.L. Jolly, X-Ray Photoelectron Spectroscopy, Accounts Of Chemical Research, 3(1970) 193-200.
[276] W.E. Swartz, X-Ray Photoelectron Spectroscopy, Analytical Chemistry, 45(1973) 788-800.
[277] E. Barsoukov, J.R. Macdonald, Impedance Spectroscopy: Theory, Experiment, and Applications: John Wiley & Sons; 2005.
[278] A. Lasia, Electrochemical Impedance Spectroscopy and Its Applications, in: B.E. Conway, J.O.M. Bockris, R.E. White (Eds.), Modern Aspects of Electrochemistry, Springer US, Boston, MA, 2002, pp. 143-248.
[279] E. Balaur, T. Djenizian, R. Boukherroub, J.N. Chazalviel, F. Ozanam, P. Schmuki, Electron Beam-Induced Modification of Organic Monolayers on Si(111) Surfaces Used for Selective Electrodeposition, Electrochemistry Communications, 6(2004) 153-7.
[280] G.R. Abel, Jr., B.H. Cao, J.E. Hein, T. Ye, Covalent, Sequence-Specific Attachment of Long DNA Molecules to a Surface Using DNA-Templated Click Chemistry, Chemical Communications, 50(2014) 8131-3.
[281] M.H. Choudhury, S. Ciampi, Y. Yang, R. Tavallaie, Y. Zhu, L. Zarei*, et al.*, Connecting Electrodes with Light: One Wire, Many Electrodes, Chemical Science, 6(2015) 6769-76.
[282] M.S. Hahn, L.J. Taite, J.J. Moon, M.C. Rowland, K.A. Ruffino, J.L. West, Photolithographic Patterning of Polyethylene Glycol Hydrogels, Biomaterials, 27(2006) 2519-24.
[283] M. Mrksich, G.M. Whitesides, Patterning Self-Assembled Monolayers Using Microcontact Printing - a New Technology for Biosensors, Trends In Biotechnology, 13(1995) 228-35.
[284] C. Thibault, C. Severac, A.F. Mingotaud, C. Vieu, M. Mauzac, Poly(Dimethylsiloxane) Contamination in Microcontact Printing and Its Influence on Patterning Oligonucleotides, Langmuir, 23(2007) 10706-14.
[285] G. De Leener, F. Evoung-Evoung, A. Lascaux, J. Mertens, A.G. Porras-Gutierrez, N. Le Poul*, et al.*, Immobilization of Monolayers Incorporating Cu Funnel Complexes onto Gold Electrodes. Application to the Selective Electrochemical Recognition of Primary Alkylamines in Water, J Am Chem Soc, (2016).
[286] T.R. Chan, R. Hilgraf, K.B. Sharpless, V.V. Fokin, Polytriazoles as Copper(I)-Stabilizing Ligands in Catalysis, Organic Letters, 6(2004) 2853-5.
[287] K. Welser, M.D.A. Perera, J.W. Aylott, W.C. Chan, A Facile Method to Clickable Sensing Polymeric Nanoparticles, Chemical Communications, (2009) 6601-3.
[288] R. Berg, B.F. Straub, Advancements in the Mechanistic Understanding of the Copper-Catalyzed Azide-Alkyne Cycloaddition, Beilstein Journal Of Organic Chemistry, 9(2013) 2715-50.
[289] F. Shamsi, H. Coster, K.A. Jolliffe, Characterization of Peptide Immobilization on an Acetylene Terminated Surface Via Click Chemistry, Surface Science, 605(2011) 1763-70.
[290] D.L. Reger, M.F. Huff, Synthesis and Characterization of Copper(I) Trifluoroacetate Alkyne Complexes of the Type $Cu_4(Mu\text{-}O_2ccf_3)_4(Mu\text{-}Alkyne)_2$ and $Cu_2(Mu\text{-}O_2ccf_3)_2(Alkyne)_2$, Organometallics, 9(1990) 2807-10.
[291] A. Poghossian, S. Ingebrandt, M.H. Abouzar, M.J. Schoning, Label-Free Detection of Charged Macromolecules by Using a Field-Effect-Based Sensor Platform: Experiments and Possible Mechanisms of Signal Generation, Applied Physics a-Materials Science & Processing, 87(2007) 517-24.
[292] S. Raghavan, C.S. Chen, Micropatterned Environments in Cell Biology, Advanced Materials, 16(2004) 1303-13.
[293] J.T. Koepsel, W.L. Murphy, Patterned Self-Assembled Monolayers: Efficient, Chemically Defined Tools

for Cell Biology, Chembiochem, 13(2012) 1717-24.
[294] A.P. Quist, S. Oscarsson, Micropatterned Surfaces: Techniques and Applications in Cell Biology, Expert Opinion on Drug Discovery, 5(2010) 569-81.
[295] K.Y. Suh, M.C. Park, P. Kim, Capillary Force Lithography: A Versatile Tool for Structured Biomaterials Interface Towards Cell and Tissue Engineering, Advanced Functional Materials, 19(2009) 2699-712.
[296] V. Hasirci, H. Kenar, Novel Surface Patterning Approaches for Tissue Engineering and Their Effect on Cell Behavior, Nanomedicine, 1(2006) 73-89.
[297] B. Guillotin, F. Guillemot, Cell Patterning Technologies for Organotypic Tissue Fabrication, Trends In Biotechnology, 29(2011) 183-90.
[298] E. Ajami, K.-F. Aguey-Zinsou, Functionalization of Electropolished Titanium Surfaces with Silane-Based Self-Assembled Monolayers and Their Application in Drug Delivery, Journal of Colloid and Interface Science, 385(2012) 258-67.
[299] M. Staples, K. Daniel, M.J. Cima, R. Langer, Application of Micro- and Nano-Electromechanical Devices to Drug Delivery, Pharmaceutical Research, 23(2006) 847-63.
[300] J.J. Pancrazio, J.P. Whelan, D.A. Borkholder, W. Ma, D.A. Stenger, Development and Application of Cell-Based Biosensors, Annals Of Biomedical Engineering, 27(1999) 697-711.
[301] J. Nakanishi, T. Takarada, K. Yamaguchi, M. Maeda, Recent Advances in Cell Micropatterning Techniques for Bioanalytical and Biomedical Sciences, Analytical Sciences, 24(2008) 67-72.
[302] P. Fromherz, A. Offenhausser, T. Vetter, J. Weis, A Neuron-Silicon Junction - a Retzius Cell of the Leech on an Insulated-Gate Field-Effect Transistor, Science, 252(1991) 1290-3.
[303] G. Zeck, P. Fromherz, Noninvasive Neuroelectronic Interfacing with Synaptically Connected Snail Neurons Immobilized on a Semiconductor Chip, Proceedings Of the National Academy Of Sciences Of the United States Of America, 98(2001) 10457-62.
[304] A. Kira, K. Okano, Y. Hosokawa, A. Naito, K. Fuwa, J. Yuyama*, et al.*, Micropatterning of Perfluoroalkyl Self-Assembled Monolayers for Arraying Proteins and Cells on Chips, Applied Surface Science, 255(2009) 7647-51.
[305] K. Itoga, J. Kobayashi, M. Yamato, A. Kikuchi, T. Okano, Maskless Liquid-Crystal-Display Projection Photolithography for Improved Design Flexibility of Cellular Micropatterns, Biomaterials, 27(2006) 3005-9.
[306] G.M. Whitesides, E. Ostuni, S. Takayama, X.Y. Jiang, D.E. Ingber, Soft Lithography in Biology and Biochemistry, Annual Review Of Biomedical Engineering, 3(2001) 335-73.
[307] J.E. Gautrot, B. Trappmann, F. Oceguera-Yanez, J. Connelly, X. He, F.M. Watt*, et al.*, Exploiting the Superior Protein Resistance of Polymer Brushes to Control Single Cell Adhesion and Polarisation at the Micron Scale, Biomaterials, 31(2010) 5030-41.
[308] W.F. Zheng, W. Zhang, X.Y. Jiang, Precise Control of Cell Adhesion by Combination of Surface Chemistry and Soft Lithography, Advanced Healthcare Materials, 2(2013) 95-108.
[309] M. Junkin, S.L. Leung, Y.L. Yang, Y. Lu, J. Volmering, P.K. Wong, Plasma Lithography Surface Patterning for Creation of Cell Networks, Jove-Journal Of Visualized Experiments, (2011).
[310] S.F. Toosi, S. Moradi, S.G. Hatzikiriakos, Fabrication of Micro/Nano Patterns on Polymeric Substrates Using Laser Ablation Methods to Control Wettability Behaviour: A Critical Review, Reviews Of Adhesion And Adhesives, 5(2017) 55-78.
[311] S. Takayama, J.C. McDonald, E. Ostuni, M.N. Liang, P.J.A. Kenis, R.F. Ismagilov*, et al.*, Patterning Cells

and Their Environments Using Multiple Laminar Fluid Flows in Capillary Networks, Proceedings Of the National Academy Of Sciences Of the United States Of America, 96(1999) 5545-8.
[312] R. Maoz, S.R. Cohen, J. Sagiv, Nanoelectrochemical Patterning of Monolayer Surfaces: Toward Spatially Defined Self-Assembly of Nanostructures, Advanced Materials, 11(1999) 55-61.
[313] R.K. Smith, P.A. Lewis, P.S. Weiss, Patterning Self-Assembled Monolayers, Progress In Surface Science, 75(2004) 1-68.
[314] J. Clausmeyer, W. Schuhmann, N. Plumere, Electrochemical Patterning as a Tool for Fabricating Biomolecule Microarrays, Trac-Trends In Analytical Chemistry, 58(2014) 23-30.
[315] N.S. Kehr, J. El-Gindi, H.-J. Galla, L. De Cola, Click Chemistry on Self-Assembled Monolayer of Zeolite L Crystals by Microcontact Printing - Applications in Nanobiotechnology, Microporous And Mesoporous Materials, 144(2011) 9-14.
[316] A. Greco, L. Maggini, L. De Cola, R. De Marco, L. Gentilucci, Diagnostic Implementation of Fast and Selective Integrin-Mediated Adhesion of Cancer Cells on Functionalized Zeolite L Monolayers, Bioconjugate Chemistry, 26(2015) 1873-8.
[317] N.S. Kehr, K. Riehemann, J. El-Gindi, A. Schafer, H. Fuchs, H.J. Galla*, et al.*, Cell Adhesion and Cellular Patterning on a Self-Assembled Mono Layer of Zeolite L Crystals, Advanced Functional Materials, 20(2010) 2248-54.
[318] S.J. Xiao, M. Textor, N.D. Spencer, M. Wieland, B. Keller, H. Sigrist, Immobilization of the Cell-Adhesive Peptide Arg-Gly-Asp-Cys (Rgdc) on Titanium Surfaces by Covalent Chemical Attachment, Journal Of Materials Science-Materials In Medicine, 8(1997) 867-72.
[319] S. Verrier, S. Pallu, R. Bareille, A. Jonczyk, J. Meyer, M. Dard*, et al.*, Function of Linear and Cyclic Rgd-Containing Peptides in Osteoprogenitor Cells Adhesion Process, Biomaterials, 23(2002) 585-96.
[320] D. Boturyn, J.L. Coll, E. Garanger, M.C. Favrot, P. Dumy, Template Assembled Cyclopeptides as Multimeric System for Integrin Targeting and Endocytosis, Journal Of the American Chemical Society, 126(2004) 5730-9.
[321] C. McNichols, J. Wilkins, A. Kubota, Y.T. Shiu, S.M. Aouadi, P. Kohli, Investigating Surface Topology and Cyclic-Rgd Peptide Functionalization on Vascular Endothelialization, Journal Of Biomedical Materials Research Part A, 102(2014) 532-9.
[322] F. He, B.W. Luo, S.J. Yuan, B. Liang, C. Choong, S.O. Pehkonen, Pvdf Film Tethered with Rgd-Click-Poly(Glycidyl Methacrylate) Brushes by Combination of Direct Surface-Initiated Atrp and Click Chemistry for Improved Cytocompatibility, Rsc Advances, 4(2014) 105-17.
[323] E. Ruoslahti, M.D. Pierschbacher, New Perspectives in Cell-Adhesion - Rgd and Integrins, Science, 238(1987) 491-7.
[324] C. Henry, N. Moitessier, Y. Chapleur, Vitronectin Receptor -Alpha(V)Beta(3) Integrin- Antagonists: Chemical and Structural Requirements for Activity and Selectivity, Mini-Reviews In Medicinal Chemistry, 2(2002) 531-42.
[325] V. Dhir, A. Natarajan, M. Stancescu, A. Chunder, N. Bhargava, M. Das*, et al.*, Patterning of Diverse Mammalian Cell Types in Serum Free Medium with Photoablation, Biotechnology Progress, 25(2009) 594-603.
[326] E. Kuru, H.V. Hughes, P.J. Brown, E. Hall, S. Tekkam, F. Cava*, et al.*, In Situ Probing of Newly Synthesized Peptidoglycan in Live Bacteria with Fluorescent D-Amino Acids, Angewandte Chemie-International Edition, 51(2012) 12519-23.

[327] T. Jafari, E. Moharreri, P. Toloueinia, A.S. Amin, S. Sahoo, N. Khakpash*, et al.*, Microwave-Assisted Synthesis of Amine Functionalized Mesoporous Polydivinylbenzene for Co_2 Adsorption, Journal Of CO_2 Utilization, 19(2017) 79-90.
[328] G. Marletta, G. Ciapetti, C. Satriano, S. Pagani, N. Baldini, The Effect of Irradiation Modification and Rgd Sequence Adsorption on the Response of Human Osteoblasts to Polycaprolactone, Biomaterials, 26(2005) 4793-804.
[329] D.J. Stephens, V.J. Allan, Light Microscopy Techniques for Live Cell Imaging, Science, 300(2003) 82-6.
[330] I. Morkvenaite-Vilkonciene, A. Ramanaviciene, A. Ramanavicius, 9,10-Phenanthrenequinone as a Redox Mediator for the Imaging of Yeast Cells by Scanning Electrochemical Microscopy, Sensors And Actuators B-Chemical, 228(2016) 200-6.
[331] Q.J. Liu, C.S. Wu, H. Cai, N. Hu, J. Zhou, P. Wang, Cell-Based Biosensors and Their Application in Biomedicine, Chemical Reviews, 114(2014) 6423-61.
[332] T. Yoshinobu, H. Ecken, A. Poghossian, H. Luth, H. Iwasaki, M.J. Schoning, Alternative Sensor Materials for Light-Addressable Potentiometric Sensors, Sensors And Actuators B-Chemical, 76(2001) 388-92.
[333] J. Suzurikawa, M. Nakao, Y. Jimbo, R. Kanzaki, H. Takahashi, A Light Addressable Electrode with a Tio2 Nanocrystalline Film for Localized Electrical Stimulation of Cultured Neurons, Sensors And Actuators B-Chemical, 192(2014) 393-8.
[334] J. Du, X.L. Chen, C.C. Liu, J. Ni, G.F. Hou, Y. Zhao*, et al.*, Highly Transparent and Conductive Indium Tin Oxide Thin Films for Solar Cells Grown by Reactive Thermal Evaporation at Low Temperature, Applied Physics a-Materials Science & Processing, 117(2014) 815-22.
[335] F. Wu, I. Campos, D.-W. Zhang, S. Krause, Biological Imaging Using Light-Addressable Potentiometric Sensors and Scanning Photo-Induced Impedance Microscopy, Proceedings of the Royal Society A: Mathematical, Physical and Engineering Science, 473(2017).
[336] M. Riedel, S. Holzel, P. Hille, J. Schormann, M. Eickhoff, F. Lisdat, InGaN/GaN Nanowires as a New Platform for Photoelectrochemical Sensors - Detection of Nadh, Biosensors & Bioelectronics, 94(2017) 298-304.